ELECTROHYDRODYNAMIC INVESTIGATION DURING MELTING OF PHASE CHANGE MATERIALS IN A CONDUCTION DOMINATED MELTING REGIME

ELECTROHYDRODYNAMIC INVESTIGATION DURING MELTING OF PHASE CHANGE MATERIALS IN A CONDUCTION DOMINATED MELTING REGIME

By Ahmed Hassan, M.A.Sc., B.A.Sc.

A Thesis Submitted to the School of Graduate Studies in Partial Fulfillment of the Requirements for the Degree

Doctor of Philosophy

in Mechanical Engineering

McMaster University

McMaster University Doctor of Philosophy (2023), Mechanical Engineering, Hamilton, Ontario

TITLE: ELECTROHYDRODYNAMIC INVESTIGATION DURING MELTING OF PHASE CHANGE MATERIALS IN A CONDUCTION DOMINATED MELTING REGIME

AUTHOR: Ahmed Hassan, B.A.Sc., M.A.Sc. (Ain Shams University)

SUPERVISOR: Dr. James S. Cotton, Professor, Dept. of Mechanical Engineering

NUMBER OF PAGES: xiv, 174

Abstract

Latent heat thermal energy storage plays an important role in bridging the gap between the energy supply and consumer demands. The latent heat storage systems use phase change materials (PCMs) which are characterized by their high latent heat and therefore lead to higher energy densities. However, one major disadvantage of PCMs is their low thermal conductivities which affects the rates of charging and discharging. Electrohydrodynamics (EHD) offers an opportunity as an active heat transfer enhancement method which can significantly enhance the melting rates while being able to control the heat transfer as per system' needs with a very low power consumption. The application of EHD in two-phase solid liquid systems results in generating electroconvection flow in the liquid medium which increases the heat transfer coefficient and decreases the melting time.

The main objective of the current work is to study the heat transfer enhancement and the role of EHD forces during melting of phase change materials (PCMs) under constant temperature boundary conditions. There are two main investigations performed in the current study. First is experimentally studying the EHD melting enhancement of PCMs while applying high voltages through two rows of electrodes embedded inside the PCM. Moreover, in the experiments, solid extraction was investigated using high speed imaging conducted at various locations with respect to the electrodes. In the second investigation, PCM melting in a rectangular cavity under the effect of EHD and constant temperature boundary conditions is studied numerically. The flow field, temperature field and phase field are simulated during the melting process until steady state condition is reached. Additionally, the effect of the applied voltage and temperature boundaries on the electroconvection flow are illustrated.

Experimentally, the EHD melting enhancement of paraffin wax is examined under different applied DC voltage magnitudes and polarities, and different temperature gradients. In addition, the role of EHD forces was investigated by applying DC and AC square waves with different frequencies and offset values. The results showed that the melting enhancement increases with a nonlinear relation with voltages, wherein the maximum effective thermal conductivity was found to be 0.95 W/m-K at -10 kV in comparison with the value of 0.2 W/m-K for the pure liquid paraffin wax, with an enhancement ratio of 4.75. The Coulomb force was concluded to be the dominant EHD force in the study while the dielectrophoretic effect was negligible.

Characterization of solid extraction was performed by measuring the intensity of extraction, and the size and velocity of dendrites after extraction at different applied voltages and temperature boundaries for different phase change materials having different mushy zone thickness. For paraffin wax, solid extraction was detected for all the applied DC voltages. Small dendrites were observed to be pulled out from the mushy zone melt front and rise upwards in a rotational manner. The extraction intensity was found to be high at locations of high Coulomb force near the electrodes. In addition, solid extraction measurements showed that the size and velocity of the extracted dendrites increases alongside the applied voltage while the velocity decreases at higher temperature boundaries. Finally, it was found that the existence of a large mushy zone results in higher solid extraction intensities.

A numerical model was conducted using the finite element method to investigate the EHD melting of PCMs. In the model, the non-autonomous charge injection assumption is used with the Coulomb force being the only electrical body force considered. First, phase-change modeling is conducted to simulate melting of paraffin wax without EHD under constant temperature boundary conditions until a steady-state condition is achieved. Next, the whole set of coupled EHD equations is introduced to the model to simulate the EHD melting process. The results revealed that two electroconvection cells were generated between each two successive electrodes in the liquid PCM. The EHD flow leads to redistribution of the temperature field which enhances the heat transfer. EHD melting continues until a steady-state condition is regained after one hour of EHD time, at which point the enhancement ratio was found to be 2.33 at 6 kV. The influence of the applied voltages and temperature boundaries on the electroconvection flow showed that the fluid velocity increases significantly by increasing the voltage while it decreases under higher temperature gradients across the liquid region.

This thesis makes a novel contribution to the state-of-the-art literature on EHD melting enhancement of PCMs showing the effects of electroconvection flow and solid extraction during the melting process. The details of the contribution made by this work have been disseminated in the form of three journal publications, which have been integrated into this sandwich Ph.D. thesis.

Acknowledgements

In the name of Allah, the Entirely Merciful, the Especially Merciful. All praise is due to Allah alone for blessing me with patience, knowledge, and strength to complete this work and granting me everything in my life.

I would like to express my gratitude to my supervisor, Dr. James Cotton. I am really thankful to you by giving me the opportunity to be in such a scholastic position. Your guidance and motivation were very supportive to me during my whole Ph.D. journey. I will always remember the critical thinking and dedicated supervision you gave me during our weekly meeting. Your mentorship made this PH.D. experience very special.

I am also grateful to Dr. Yasser for his suggestions and technical support whenever I needed him. Special thanks to Jeff and Ali who helped me a lot in the lab. You never hesitate to offer help and guidance.

Special thanks to the mechanical engineering technicians, John, Mike, Mark, Justin, and Steve. Special thanks to Mike who helped me a lot designing and manufacturing my test section.

I would like to give thanks to the TMRL team, an amazing team of people who kept me company. Special thanks to James who helped me a lot and was very supportive. Deepest thanks to my friends Safy, Abdelnabi, Saber, and Samy, I couldn't have done it without you.

To my late father, I wish you were here to be proud of me. I owe you everything I have. May Allah bless your soul in paradise. *To my mother*, your love, and prayers to me are what kept me going. Thanks for my *brother, Muhammed, and my sisters Marwa and Israa*, I count on you to be my rock.

Last, and most importantly, thanks to my *amazing wife Aiat*. Thanks for being with me, motivating and supporting me in every step I take. You always had my back.

Table of Contents

Nomenclature

A	Area (m^2)
b_i	Electric mobility (m^2/V.s)
c_p	Specific heat capacity (kJ/kg.K)
D	Diffusion coefficient (m^2/s)
e	Charge constant (C)
E	Electric field (N/m)
f	Force (N)
H	Cell height (m)
I	Total electric current (A)
J	Current density (mol/m^2s)
k	Thermal conductivity (W/m.K)
n_i	Ion concentration (mol/m^3)
Nu_E	Electric Nusselt number
P	Pressure (Pa)
Pr	Prandtl number
q	Space charge density (C/m^3)
Q	Heat flux (W)
Ra	Rayleigh number
S_E	Melt thickness (m)
St	Stefan number
T	Temperature (K)
T_E	Electric Rayleigh number

u	Velocity field (m/s)
V	Voltage (V)

Greek symbols

α	Thermal diffusivity (m^2/s)
γ	Liquid fraction
ε	Dielectric constant
μ	Dynamic viscosity (kg/m.s)
ρ	Mass density (kg/ m^3)
σ	Electrical conductivity (S/m)
τ	Charge relaxation time (s)
φ	Electric potential (V)

Subscripts

c	Cold
eff	Effective
h	Hot
l	Liquid
m	Mushy
mh	High melting point
ml	Low melting point
s	Solid

Acronyms

PCM	Phase Change Material
LHS	Latent Heat Storage

Co-Authorship

This thesis was prepared according to the standard sandwich thesis format and contains multi-authored papers with details of the academic contribution of this thesis. The majority of the contributions to the papers were based on the first author's work. The following describes the contributions of each author and demonstrates the contributions of Ahmed Hassan the author of this thesis:

Paper I: Hassan, Ahmed, and James S. Cotton. "Investigation of the role of electrohydrodynamic forces on the heat transfer enhancement and solid extraction during melting of paraffin wax under constant temperature boundary conditions." International Journal of Heat and Mass Transfer 204 (2023): 123831.

Ahmed Hassan: Conceptualization, Methodology, Software, Validation, Investigation, Data curation, Formal analysis, Writing original draft. **James S. Cotton:** Supervision, Funding acquisition, Writing, review, and editing.

Paper II: Numerical investigation of the role of charge injection and Coulomb force during the melting of phase-change materials under constant temperature boundary conditions. Submitted to Physics of Fluids journal.

Ahmed Hassan: Conceptualization; Analytical formulations; Modeling; Data curation; Formal analysis; Investigation; Methodology; Validation; Visualization; Writing - original draft. James S. Cotton: Conceptualization; Deliberating the results; Funding acquisition; Supervision; Writing - review & editing.

Paper III: An investigation of the electroconvection flow and solid extraction during melting of phase-change materials. Submitted to Journal of Electrostatics.

Ahmed Hassan: Conceptualization; Analytical formulations; Modeling; Data curation; Formal analysis; Investigation; Methodology; Validation; Visualization; Writing - original draft. James S. Cotton: Conceptualization; Deliberating the results; Funding acquisition; Supervision; Writing - review & editing.

Chapter 1: Introduction

1.1 Introduction and literature review

1.1.1 Thermal energy storage

Thermal energy storage technologies have brought the attention of many researchers in the last few decades owing to their crucial role in solving the world's energy crisis. The application of thermal energy storage systems can result in many economic and environmental benefits. Economically, these systems can play a vital role in reducing the gap between energy supply and consumer demands which can yield higher system efficiency and better reliability. Additionally, the development and implementation of thermal energy storage is crucial in enabling the widespread use of renewable energy sources, especially solar energy and wind energy which are characterized by their intermittent energy supply. This can contribute to lower dependence on traditional fossil fuels and consequently can result in reductions in CO2 emissions [1].

Thermal energy storage is classified into three different types: sensible heat storage, latent heat storage, and thermochemical storage. Thermochemical storage systems are based on thermochemical materials undergoing reversible chemical reactions. In sensible heat storage systems, energy is stored by increasing the temperature of a solid or a liquid material, where the amount of stored energy depends on the mass and specific heat of the material as well as the change in temperature. On the other hand, latent heat storage requires phase transformation of a material within a narrow temperature range which increases the energy density of the system leading to a reduction in their size and weight, which makes them the most effective heat storage technique [2], [3].

The kind of materials used in the latent heat storage (LHS) systems are called phase change materials (PCMs). These materials have the advantage of having high latent heat capacity which enables the storage of high amounts of energy. During the charging process, the PCM absorbs sensible heat first until its temperature reaches the phase transition temperature. Then, phase change starts to occur where the melting process of the PCM takes place at nearly constant temperature while latent heat is stored in the material as shown in Fig. 1. In the discharging process, solidification of the material occurs, and the stored heat is released from the material. PCMs can be categorized mainly into two groups: organic and inorganic. Organic PCMs, including paraffins and fatty acids, are distinguished by their chemical and thermal stability, low degree of subcooling and non-corrosiveness. Conversely, inorganic PCMs, such as salt hydrates, are chemically unstable and high corrosive, however they are characterized by having higher latent heat compared to the organic types [3]–[5].

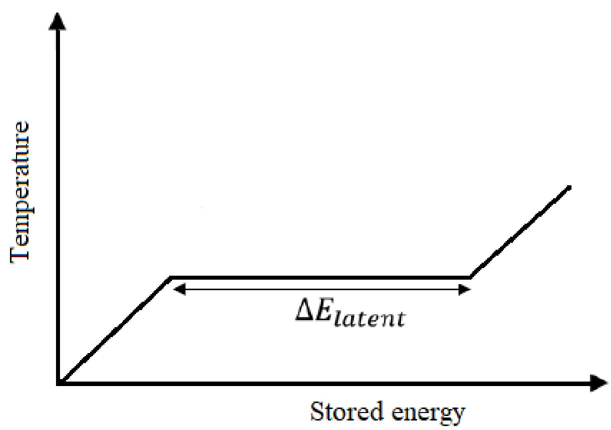

Figure 1: Latent heat thermal storage vs temperature

1.1.2 Heat transfer enhancement techniques

Among the most undesirable features of PCMs is their low thermal conductivity, ranging from 0.1 to 0.6 W/m*k [6], which reduces the rate of heat exchange between the PCM and the heat transfer fluid. This leads to lower rates of melting and solidification during the charging and discharging processes, ultimately leading to a decrease in the overall system performance. To address this problem, several heat transfer enhancement techniques have been developed. These techniques are classified into two categories: passive and active. Passive techniques do not need external power to enhance the heat transfer, and they usually rely on modifying the surface geometry or enhancing the thermal properties of the PCM. These methods have the advantages of their simple design, low cost, and reliability [7], [8]. Active techniques on the other side require external power to take effect, which gives the advantage of controlling the heat augmentation as per need of the system [7].

The common approaches employed for the passive methods involve utilizing extended surfaces, employing mixing promoters, using multiple PCMs, or adding fluid additives of high thermal conductivity. Extended surfaces such as fins and heat pipes are used to increase the heat transfer area of the system allowing more heat to flow. In LHS systems, both longitudinal and radial fins are installed at the side of the lower thermal conductivity fluid which is the PCM to increase the heat transfer [3], [7], [9], [10]. Several studies have found that heat transfer enhancement depends on increasing the number fins and the fin size [3]. PCM microencapsulation is an alternative method to increase the heat transfer surface area, where the LHS system is comprised of a shell polymer containing the PCM in its core [4], [9], [10]. A different technique that can be used to enhance the heat transfer is using mixing promoters or turbulators to increase the system turbulence, thereby reducing the thermal boundary layer thickness and consequently increasing the heat transfer coefficient of the fluid. The mechanisms used include swirl devices and adding artificial roughness to the heat transfer surface [7], [8]. Furthermore, using multiple PCMs is an effective way that can be implemented to enhance the heat transfer by creating uniform heat flow through the system. In this approach, PCMs are arranged in a descending order based on their respective melting points which can maintain a nearly constant temperature difference between the PCM and the heat transfer fluid [3], [11]. The issue of the low thermal conductivity of PCMs can be addressed by incorporating high conductive additives directly into the PCM which increases the overall thermal conductivity of the composite. Extensive studies on different additive materials with various mass fractions were performed to determine the optimum system performance. Materials that can be employed as additives include porous substances, such as expanded graphite, and nanoparticles such as Al nano-powders and carbon nanotubes [3], [4], [8]–[10]. A summary of the different heat transfer enhancement passive techniques is presented in Table 1. The results are presented using the effective thermal conductivity parameter which is defined as the ratio of the thermal conductivity using the enhancement method to the original thermal conductivity of the PCM.

Table 1: Passive heat transfer enhancement methods

Passive method	**Thermal conductivity enhancement**	**Reference**
PCM additives	Up to 12 times enhancement.	[12]–[15]
PCM encapsulation	Up to 8 times enhancement.	[16]–[18]
Fins	Up to 3 times enhancement (30 – 40 % decrease in melting or solidification times).	[19], [20]
Multiple PCMs	Up to 21% decrease in melting time.	[3]

Moreover, the most common active heat transfer enhancement methods studied in literature include Electrohydrodynamic (EHD), Magnetohydrodynamic, ultrasonic vibration, mechanical aid, and pulsating flow. In electrohydrodynamics, heat transfer is augmented due to a secondary flow generated in the medium as a result of an external electric field. Previous studies reported an enhancement ratio that ranged from 1.5 – 5.5 for both single phase and multiple phase systems [21]. Magnetohydrodynamics is a similar method which uses an external magnetic field to manipulate and control a flow generated in a magnetic fluid [22]. Heat transfer enhancement up to 4 times was reported in literature [7]. For ultrasonic vibration method, an oscillating flow is produced which can significantly increase the heat transfer. Oh et al. [23] reported a 2.5 decrease in the melting time when using ultrasonic vibration during melting of different PCMs. Mechanical aid methods involve disrupting the thermal boundary layer of the fluid by means of mechanical agitation or stirring. The maximum enhancement in Nusselt number reached 4.3-fold [24]. Ultimately, in the pulsating flow method, flow mixing as well as increasing turbulence can be achieved through the dynamic behavior of the flow, where the rate of heat transfer can increase up to 3.5 times that of the steady flow [25].

1.1.3 Electrohydrodynamics

Electrohydrodynamics (EHD) is an active heat transfer enhancement method in which a high voltage is applied to a dielectric medium to create an electric field. The generated electric field creates electrical body forces in the bulk of the fluid and interfacial forces at the interface of multi-phase systems. The EHD forces acting on a dielectric fluid per unit volume can be formulated as [26]:

$$\bar{f}_{eB} = q\bar{E} - \frac{1}{2}E^2\nabla\varepsilon + \frac{1}{2}\nabla[\rho E^2 \left(\frac{\partial\varepsilon}{\partial\rho}\right)_T] \quad (1)$$

Where q is the charge density, E is the electric field, ε is the electric permittivity, and ρ is the fluid mass density. The three terms on the right-hand side of Equation (1) represent the electrophoretic (Coulomb force), the dielectrophoretic force and the electrostrictive force, respectively [27]. The Coulomb force is generated by the application of electric field (E) on the free charges in the fluid (q), and it is considered the main contributor to heat-transfer enhancement in single-phase systems. The dielectrophoretic force requires a high non-homogenous electric field in the medium, and it becomes effective at the interface between the different phases that have a measurable difference in their electrical permittivity, or in the bulk of the fluid with a high temperature gradient that creates a gradient in permittivity. The electrostrictive force is significant when there is a change in permittivity with density including liquid vapor interfaces and compressible systems [28], [29].

In two-phase solid-liquid systems, only the Coulomb and the dielectrophoretic forces are significant. The Coulomb force is generated when there are free charges in the medium which can exist via different charge creation mechanisms. One mechanism is called charge injection, where free charges are directly injected from the electrodes. In this mechanism electrochemical processes take place at the electrode surface wherein neutral species undergo reduction or oxidation reactions [30]. The amount of charge injection depends on the local electric field at the electrode as well as the materials of both the electrode and the dielectric medium. The other charge creation mechanism is conduction where free charges are generated from a thermally induced conductivity gradient called field-enhanced dissociation. A non-equilibrium charged layer (hetero-charge layer) is induced around the electrode by the process of dissociation and recombination of the generated ions. The electric field intensity should be low enough to prevent direct injection of ions from the electrodes [31]. Daaboul et al. [32] experimentally investigated the transition from conduction to injection mechanisms in a blade-plane electrode configuration. It was found that conduction is dominant at voltages below 1.2 kV where the EHD flow was observed to be directed towards the blade tip, which is considered a characteristic for conduction phenomenon where the EHD forces are directed towards the electrode with the lower curvature. When the applied voltage exceeds 1.4 kV the flow direction is reversed concluding that injection mechanism prevails.

In case of charge injection, free charges are accumulating over a timescale called the charge relaxation time ($\tau_e = {}^{\varepsilon}/_{\sigma}$), where ε and σ are the dielectric constant and the electrical conductivity of the material. Hence, when an AC voltage is applied with high frequency causing the waveform's period to become smaller than the charge relaxation time, the Coulomb force will be diminished as the charges will not have adequate time to respond to the voltage variation [27], [33]. The other important time scale that can affect the dominance of the Coulomb force is the ionic transit time, which is the time required for the charge carriers to reach the collector electrode. The ionic transit time is formulated as:

$$\tau_K = \frac{d^2}{bV}$$

Where d is the distance between the electrodes, b is the ion mobility, and V is the voltage applied.

Electrohydrodynamic technique has attracted the attention of many researchers recently owing to its advantages, which makes it a favorable heat transfer enhancement method that can be applied in many applications. One of the most important EHD advantages is the ability to control the heat transfer as per system' needs. Besides, EHD offers benefits such as low power consumption, absence of moving parts, the ability to operate at no gravity conditions. Due to its favorable qualities, EHD can find use in various applications including heat exchangers [34], EHD fluid pumping [35], drying processes [36], and thermal energy storage.

In two-phase thermal energy storage systems EHD can be utilized to enhance heat transfer during charging and discharging processes. Experimentally, Dellorusso [37] and Thompson [38] studied solidification of PCMs under the effect of EHD. Their findings showed that in solidification processes, where conduction plays a predominant role, EHD has a minimal impact. It was also hypothesized that the EHD-induced electroconvection might cause a decrease in the nucleation rate which leads to the low enhancement. For EHD melting, Nakhla et al. [39]

experimentally studied the influence of EHD during melting of paraffin wax under constant heat flux boundary condition in a conduction dominated melting regime. The study demonstrated that the application of EHD at -8 kV can reduce the time it takes for the melt thickness to reach 7 mm by about 40% for the lowest heat flux case studied (7.1 W). By increasing the heat flux at the top surface, the EHD melting enhancement is reduced. In another study, the author investigated melting of n-octadecane under constant temperature boundary conditions and different applied voltages [40]. The results showed that the melt thickness increased by 7 mm due to the application of EHD at 4 kV. By the increase of voltage, melting enhancement increased, wherein the maximum increase in melt thickness reported was about 17 mm at 10 kV. In their study, a dimensionless parameter was defined to represent the amount of heat transfer enhancement with EHD, which is the electric Nu number. This factor is defined as the ratio of heat transfer with EHD to the heat transfer solely by conduction, it was represented as [40]:

$$\overline{Nu}_E = \frac{k_s(T_m - T_c)S_E}{k_l(T_h - T_m)(H - S_E)} \qquad (2)$$

Where k_s and k_l are the solid and liquid thermal conductivities, T_m is the melting temperature, T_h and T_c are the top and bottom surface temperature boundaries. The maximum electric Nu number reported at 10 kV was 8.6.

In a later study, Nakhla et al [41] expanded his work to examine the coupling between the gravitational and electrical body forces during melting of Octadecane in an initially convection dominated regime under different Rayleigh numbers. The level of EHD enhancement was quantified as the ratio of the time required to melt 50% of the PCM volume with EHD forces compared to that without EHD forces. It is observed that the enhancement factor increases with the magnitude of the applied voltage where the maximum value achieved for the lowest Rayleigh number (Ra=9E7) case at (-6 kV) was about 1.7. The flow regimes and the electroconvection cells were measured using a novel shadowgraph technique. With the application of EHD, the flow structure changed from being an initially gravitationally dominated (one convection cell bounding the whole liquid) into a mixed electrical and gravitational regime, wherein bifurcation of the original convection cell was observed. In other work, Sun et al. [42] experimentally studied melting n-Octadecane in a 4 cm * 4 cm rectangular cavity. Melting progresses by maintaining the vertical sides at hot and cold temperatures. When the voltage was applied at the hot heat exchanger, the electric field was found to retard the melting process, wherein the liquid fraction decreased by about 30% at 20 kV applied voltage. Conversely, by applying the high voltage to the other electrode (cold heat exchanger), a 43 % increase in the melt fraction was reported. In a later study, Sun et al [43] studied the EHD melting enhancement of n-Octadecane in a rectangular cavity with a cylindrical electrode placed at the center. The cylinder was connected to the high voltage side while the bottom surface was grounded. The application of EHD showed no enhancement at the lowest applied voltage (5 kV). At higher voltages (±15 kV and ±25 kV), melting enhancement starts to be manifested. When comparing the positive and negative polarities, the author found that the negative electric potential always showed better results than the positive cases. The maximum enhancement reported for the -25 kV case was about 68% decrease in melting time. Additionally, EHD was found to have limited effect on melting when applying high frequency AC square wave. In their novel later study, Sun et al. [44] experimentally investigated the heat transfer enhancement of phase change materials with a combined passive and active techniques. High-conductive material (nanographene) was passively added to the PCM while applying EHD as an active heat transfer method. The high voltage was applied at the bottom electrode while grounding the top surface. For pure n-octadecane, no EHD enhancement was observed at voltages below 10 kV. By increasing the applied voltage to higher magnitudes, melting enhancement is observed. The increase in the total absorbed energy after 3 hours compared to the case of melting of pure PCM without EHD was about 113%, 135%, and 153 % at 15 kV, 20 kV, and 25 kV, respectively. For the composite PCM, the results showed that the liquid fraction increases significantly with the increase of weight fraction of nanographene at -10 kV. The increase in the absorbed energy was 35.1%, 35.9%, and 68.3% for 0.5wt%, 1.0wt%, and 2.0wt%, respectively.

A summary of the amount of heat transfer enhancement with EHD for the different experimental studies is presented in Table 2.

Table 2: Summary of experimental studies for EHD melting enhancement.

Reference	**Experimental configuration**	**PCM**	**Boundary conditions**	**Heat transfer enhancement**
Nakhla et al. [39]	Rectangular cavity with 2 rows of electrodes.	Paraffin wax	Constant heat flux	40% decrease in melting time at -8 kV.
Nakhla et al. [40]	Rectangular cavity with 3 rows of electrodes.	n-Octadecane	Constant temperature at top and bottom.	17 mm increase in melt thickness at +10 kV.
Nakhla et al. [41]	Rectangular cavity with 5 rows of electrodes.	n-Octadecane	Constant temperature at one vertical side.	1.7-fold at +6 kV.
Sun et al. [42]	Rectangular small cavity.	n-Octadecane	Constant temperature at both vertical sides.	44% increase in liquid fraction at +20 kV.
Sun et al. [43]	Rectangular cavity with centered cylindrical electrode.	n-Octadecane	Constant temperature at cylinder electrode surface.	68% decrease in melting time at -25 kV.
Sun et al. [44]	Rectangular small cavity.	n-Octadecane with nanographene	Constant temperature at top and	124.8% increase in the absorbed

	additive.	bottom.t temp	energy at –10 kV.

Heat transfer enhancement during melting of phase change materials have also been studied numerically in several studies. Charge injection was considered the dominant mode of generation of free charges in the medium and the Coulomb force is the main electrical body force considered in those works. Modeling charge injection can be either autonomous or non-autonomous. In autonomous injection, a constant space-charge density boundary condition is assumed at the injector electrode [30], [45], while in nonautonomous injection, the charges are formed at the interface of the electrode and the liquid where the injection current is functionally dependent on the local electric field [46], [47].

The governing equations deriving the EHD model of charge injection are given as follows.

Electric field equation and Poisson equation for electric potential:

$$E = -\nabla \varphi \qquad (3)$$

$$\nabla E = q/\varepsilon\varepsilon_0 \qquad (4)$$

Where φ is the electric potential, E is the electric field, q is the space charge density, and ε is the relative permittivity of the medium.

Charge transport equation:

$$\frac{\partial n_i}{\partial t} + \nabla j_i = 0\ , \qquad (5)$$

Where $j_i = n_i b_i E + n_i u - D_i \nabla n_i$ which represent the charge transport due to electric field migration, convection transport, and diffusion transport. In the above equation, n is the ion concentration for the different species, b is the electric mobility, and D is the diffusion coefficient.

Continuity equation:

$$\nabla . u = 0 \qquad (6)$$

Momentum equation:

$$\rho \frac{\partial u}{\partial t} + \rho(u.\nabla)u = -\nabla P + \mu\nabla^2 u + qE - \rho g \qquad (7)$$

Energy equation:

$$\frac{\partial T}{\partial t} + \nabla.(\mathrm{uH}) = \nabla.(\alpha\nabla\mathrm{T}) \qquad (8)$$

The numerical model was used to simulate the electric field, velocity field, temperature field, and space charge of the medium during the melting process in several studies. In some works, EHD modeling was implemented for melting of PCMs in a rectangular cavity where the hot temperature boundary was specified for the bottom surface [48]–[50]. A constant electric potential and space charge boundary conditions are identified for the hot bottom wall. The results were presented for different electric Rayleigh number (T), Stefan number (St), and Prandtl number (Pr). There findings revealed that the melting enhancement was limited at the initial stage of melting as the melting regime was initially conduction-dominated. As time progresses, melting enhancement is observed as the EHD forces overcome the viscous forces. Additionally, it was found that melting enhancement increases with the increase of electric Rayleigh number due to the increase of Coulomb force. Besides, better enchantments were observed for the cases of high Pr numbers and low St numbers due to the higher thermal conductivities and latent heat for these cases. Furthermore, Lu et al. [49] compared between two cases: melting from below and melting from the left wall, and it was concluded that the enhancement for the case of melting on the left wall were always higher compared to the other case. Moreover, Selvakumar et al. [51] studied the case for melting from the vertical sides at different Rayleigh numbers. The results showed that melting was initially dominated by the buoyancy effect until a deflection point at which a transition to EHD force-dominated melting occurs. Also, it was shown that the effect of Ra number on EHD melting is more significant at higher values of electric Rayleigh number (T). Elsewhere, EHD melting of PCMs in concentric annular cylinder configuration was studied by He et al. [52] while changing the aspect ratio of the cylindrical electrodes. It was shown that both the Ra number and electric Rayleigh number can influence the EHD melting due to the combined effect of the buoyancy and the EHD forces. Moreover, it was found that melting is enhanced by increasing the aspect ratio up to AR=1 that corresponds to the circular cylinder. In a later study He et al. [53] investigated the effect of low gravity conditions for a concentric cylinder's configuration on the melting process with findings showing that the effect of gravity is more significant for low electric Rayleigh numbers. In other work, Selvakumar et al. [54] studied the effect of orientation of shell and tube latent heat system. The results indicated that melting performance is a little higher for the case of horizontal orientation because of the reduced buoyancy force. A summary of the EHD melting enhancement reported in the above numerical studies is presented in Table 3.

Table 3: Summary of numerical studies for EHD melting enhancement.

Reference	**Numerical Domain**	**Thermal Boundary conditions**	**Heat transfer enhancement**
Luo et al. [48]	Rectangular cavity	Constant temperature at	Up to 50% decrease in melting time at T = 1000, Pr = 10, St = 0.1

		bottom wall	
He et al. [52]	Circular-elliptical annuli	Constant temperature at inner electrode	About 88% decrease in melting time at T = 1000, AR = ¾
Lu et al. [49]	Rectangular cavity	Constant temperature at bottom wall or Left wall	Reduction in melting time: 62 % for left wall and 46% for bottom wall.
Selvakumar et al. [50]	Rectangular cavity	Constant temperature at bottom wall	Up to 56% decrease in melting time at T = 3000, St = 0.01
Endigeri et al. [55]	Square cavity with electrode at center	Constant temperature at left wall	About 63% reduction in melting time at T = 2000, Ra = 1000
He et al. [53]	Concentric cylinders	Constant temperature at inner electrode	Maximum time saving of 95% at 0.5g, T = 2500.
Selvakumar et al. [54]	Concentric cylinders	Constant temperature at inner electrode	Reduction in melting time: 82.5% for vertical orientation and 89.6% for horizontal orientation.

According to the above literature, EHD melting enhancement in two-phase latent heat systems is mainly due to two main effects: electroconvection flow and solid extraction. Electroconvection flow is generated in the liquid PCM under the action of the electrical body forces. This secondary motion, which is in the form of electroconvection cells, disturbs the thermal boundary layer and leads to increasing the heat transfer coefficient [56], [57]. The flow structure and the number of electroconvection cells depend on the electrode configuration and the boundary conditions applied at the electrodes. In a needle plane electrode configuration, the EHD flow was found to be generated from the needle tip and moves downwards towards the bottom surface [58]. The fluid velocity increases along the vertical distance of the interelectrode gap until reaching a maximum value when it starts to slow down and then recirculates near the plane as shown in Fig. 2.

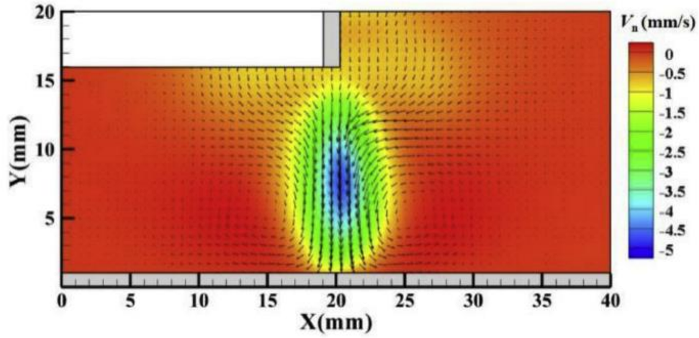

Figure 2: EHD flow for a needle plane electrode configuration at -2 kV applied voltage [58].

Fig. 3 shows the EHD flow for the two main studied configurations, the rectangular cavity and the concentric cylinders. For the rectangular cavity configuration, two electroconvection cells are observed at the initial stages of melting which then bifurcates into four roll structure as melting progresses [48]. This can be hypothesized by the influence of the Ra number on the flow structure which changes with movement of the interface upwards during melting. For the concentric cylinders' configuration, the results revealed that a number of electroconvection cells, which depend on the interelectrode distance, are formed and distributed evenly around the electrode [53]. Also, it has been shown that as the electric Rayleigh number increases, bifurcation of cells is remarked [48].

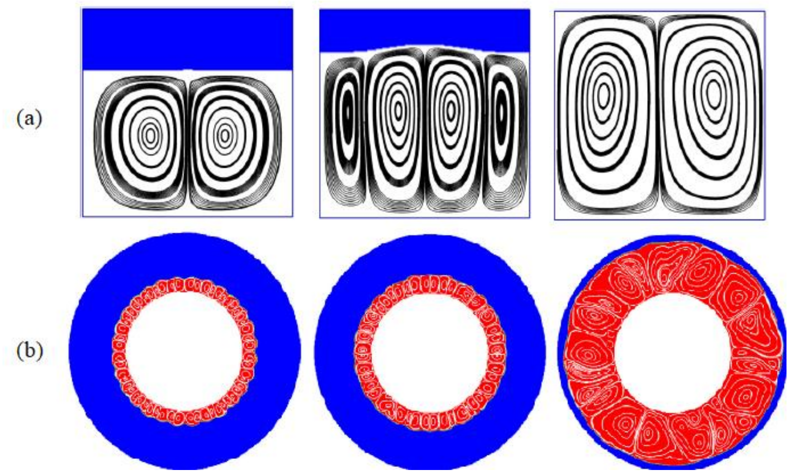

Figure 3: EHD flow during melting of PCMs: (a) rectangular cavity configuration [48], *(b) Concentric cylinders configuration* [53].

The other factor that can contribute to improving the heat transfer in two-phase solid-liquid systems is solid extraction. This phenomenon was first detected in the study of Nakhla et al. [39] where the heat transfer enhancement during melting of paraffin wax under the effect of EHD was examined. The PCM was contained in a rectangular enclosure with a constant heat flux boundary condition applied at the top surface while supplying high voltage through two rows of electrodes embedded inside the PCM. In the experiments, high-speed imaging was conducted to visually observe and analyze the behavior of the solid-liquid interface as melting progresses, allowing for real-time visualization of the melt front. From the high-speed images, the author was able to detect very small particles being pulled out from the mushy region and moving upwards into the liquid bulk. The solid dendrites are then observed to be melting as they migrate into higher temperature regions as shown in Fig. 4.

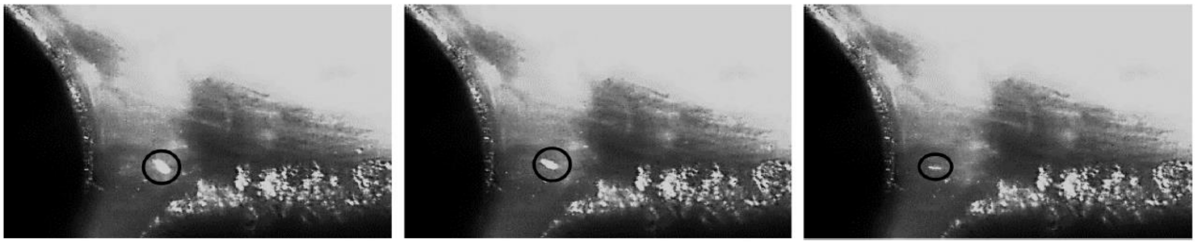

Figure 4: Solid extraction visualization [39].

Elsewhere, Thompson et al. [38] performed high speed imaging during solidification process of paraffin wax in a similar electrode configuration and was not able to detect any solid extraction near the interface. In other work, Nakhla et al. [40] investigated the EHD melting of n-octadecane under constant temperature boundary conditions. Again, solid extraction was not detected in any of the experiments conducted in their study.

1.2 Summary

Electrohydrodynamics (EHD) has been studied experimentally and numerically in various previous works for two-phase latent heat systems. Their findings showed that EHD is an effective heat transfer method that can enhance the melting performance of such systems significantly. Additionally, it was shown that heat transfer enhancement is due to two main mechanisms, first is the electroconvection flow generated in the liquid volume and second is the solid extraction phenomenon detected at the solid-liquid interface. These mechanisms come into effect under the action of the electrical body forces as well as the interfacial EHD forces, wherein the influence of the EHD forces is found to be dependent on the interaction between the thermal, electrical, and gravitational fields. When the EHD forces prevail over the counteracting thermal and gravitational influences, electroconvection becomes dominant and heat transfer is augmented. However, there are some key research gaps that were revealed from the above literature review and will be addressed in the current study. The literature key gaps include:

- The role of the Coulomb and dielectrophoretic forces in the heat transfer enhancement in solid-liquid systems is not clear.
- The effect of the temperature gradient on the EHD melting enhancement was not studied.
- The influence of applying AC voltage with different wave forms on charge injection needs more investigation. Also, the effect of the wave form frequency and determining the critical frequency of charge relaxation needs to be emphasized.
- Numerical modeling of charge injection during melting of phase change materials was conducted only using the autonomous injection assumption, where a constant space charge density boundary condition is applied at the electrodes which is not an accurate representation of the process. Therefore, it is challenging for researchers to develop a numerical model that can accurately simulate the process of charge injection as a function of the local electric field.
- Study of the electroconvection flow in two-phase solid-liquid systems was only performed for two main electrode designs: the rectangular cavity, and the concentric cylinders. Investigation of the EHD flow in different electrode configurations needs to be examined.
- Solid extraction is a new phenomenon that was detected by Nakhla et al. [39] during melting of paraffin wax, however it was not detected in the other studies of Thompson et al. [38] and Nakhla et al. [40]. Further exploration is required to understand the physics responsible for solid extraction in solid-liquid systems.
- The effect of the electric field gradient and the PCM mushy zone thickness on solid extraction needs to be studied.

- Solid extraction characterization and understanding the role of the Coulomb and the dielectrophoretic forces on extraction of dendrites need to be examined.

1.3 Objectives and contributions

The main objectives of the current research can be summarized as follows:

- Study of the EHD melting enhancement of paraffin wax in a conduction dominated melting regime under constant temperature boundary conditions. The effect of different applied DC voltage magnitudes and polarities and different temperature boundaries to be considered.
- Study the effect of AC voltage wave form at different frequencies and offset values to examine the role of the different EHD forces on melting enhancement.
- Investigate the solid extraction phenomenon at different locations with respect to the electrodes during EHD melting of paraffin wax.
- Solid extraction characterization during melting of different phase change materials having different mushy zone thicknesses.
- Develop a numerical model that can simulate the process of charge injection and Coulomb force in two-phase solid-liquid systems.
- Study numerically the EHD heat transfer enhancement during melting of paraffin wax under constant temperature boundary conditions.
- Study numerically the effect of voltage magnitudes and temperature gradients on the electroconvection flow and Coulomb force in two-phase solid-liquid systems.

The contributions of this thesis, which are fully documented in the three journal publications presented in chapters 2, 3, and 4, can be summarized into the following:

- Heat transfer enhancement under EHD effect, at different DC voltages magnitudes and polarity and different temperature gradients.
- The impact of applying AC square waves at different frequencies and offset values on EHD melting and solid extraction while identifying the critical frequency for charge relaxation.
- Investigation of solid extraction for different phase change materials using two different electrode configurations.
- Solid extraction characterization with the measurement of the size and velocities of the extracted dendrites at different applied voltages and temperature gradients.
- Development of a numerical model of charge injection assuming non-autonomous injection at the electrodes.
- Numerical modeling of EHD melting of PCMs under constant temperature boundary conditions and studying the influence of voltage and temperature gradients on the electroconvection flow and Coulomb force.

Below is a brief description of the main contributions of each publication.

Paper I: "Investigation of the role of electrohydrodynamic forces on the heat transfer enhancement and solid extraction during melting of paraffin wax under constant temperature boundary conditions," published in *Int. J. Heat Mass Transfer*. This paper focuses on investigating the EHD effect during melting of paraffin wax in an initial conduction dominated melting experiments under constant temperature boundary conditions.

The novelty of this paper is determining the role of the Coulomb and dielectrophoretic forces on the EHD melting enhancement through applying DC and AC voltages with different frequencies through two rows of electrodes embedded inside the PCM. The effects of the temperature boundaries as well as the polarity of the applied voltage were determined. Moreover, solid extraction behavior at the melt front interface during EHD melting was investigated using high speed imaging.

Paper II: "Investigation of the role of charge injection and Coulomb force during the melting of phase-change materials under constant temperature boundary conditions," submitted to *Physics of fluids* journal. This paper focuses on numerically modeling an EHD melting problem, wherein a phase change material is melted under constant temperature boundary conditions under the effect of EHD until steady state condition is achieved.

The novelty of this paper is in the development of a numerical model that can simulate the charge injection process using the full EHD coupled equations while applying a non-autonomous boundary condition at the high-voltage electrodes. The time-dependent solutions for the electric field, space charge density, flow field, temperature field, and phase field were determined during the melting process.

Paper III: "Investigation of the electroconvection flow and solid extraction during melting of phase change materials," submitted to *Journal of electrostatics.* This paper demonstrates the influence of the applied voltages and temperature boundary conditions on the electroconvection flow and solid extraction in two-phase solid liquid systems.

The novelty of this paper is in applying the numerical model developed in the prior study to illustrate the impact of changing the applied voltage on the Coulomb force and consequently the electroconvection flow during EHD melting of PCMs. The influence of the buoyancy force on EHD melting is also demonstrated via applying different temperature gradients across the liquid phase. Furthermore, solid extraction characterization was performed by means of measuring the velocity and size of the extracted dendrites at different applied voltages and temperature boundaries. The effect of mushy zone thickness on solid extraction intensities was also determined.

1.4 Thesis Organization

This thesis is organized in 5 chapters:

Chapter 1 introduces the thesis with a background and a critical literature review emphasizing the primary area of investigation in this study and identifying the key research gaps in the field. Furthermore, a highlight on the objectives and contributions of this research work to the state-of-the-art literature in the field is presented.

Chapter 2 presents the first paper titled: "Investigation of the role of electrohydrodynamic forces on the heat transfer enhancement and solid extraction during melting of paraffin wax under constant temperature boundary conditions."

Chapter 3 presents the second paper titled: "Numerical investigation of the role of charge injection and Coulomb force during the melting of phase-change materials under constant temperature boundary conditions."

Chapter 4 presents the third paper titled: "Investigation of the electroconvection flow and solid extraction during melting of phase change materials."

Chapter 5 concludes the thesis and recommends future work on the subject matter.

1.5 References

[1] A. G. Olabi, C. Onumaegbu, T. Wilberforce, M. Ramadan, M. A. Abdelkareem, and A. H. Al – Alami, "Critical review of energy storage systems," *Energy*, vol. 214, p. 118987, 2021, doi: 10.1016/j.energy.2020.118987.

[2] G. Alva, Y. Lin, and G. Fang, "An overview of thermal energy storage systems," *Energy*, vol. 144, pp. 341–378, 2018, doi: 10.1016/j.energy.2017.12.037.

[3] N. I. Ibrahim, F. A. Al-Sulaiman, S. Rahman, B. S. Yilbas, and A. Z. Sahin, "Heat transfer enhancement of phase change materials for thermal energy storage applications: A critical review," *Renew. Sustain. Energy Rev.*, vol. 74, no. October 2015, pp. 26–50, 2017, doi: 10.1016/j.rser.2017.01.169.

[4] Y. Lin, Y. Jia, G. Alva, and G. Fang, "Review on thermal conductivity enhancement, thermal properties and applications of phase change materials in thermal energy storage," *Renew. Sustain. Energy Rev.*, vol. 82, no. May 2017, pp. 2730–2742, 2018, doi: 10.1016/j.rser.2017.10.002.

[5] M. Saffari, A. de Gracia, C. Fernández, and L. F. Cabeza, "Simulation-based optimization of PCM melting temperature to improve the energy performance in buildings," *Appl. Energy*, vol. 202, pp. 420–434, 2017, doi: 10.1016/j.apenergy.2017.05.107.

[6] Zalba, Belen, et al. "Review on thermal energy storage with phase change: materials, heat transfer analysis and applications." Applied thermal engineering 23.3 (2003): 251-283.

[7] T. Alam and M. H. Kim, "A comprehensive review on single phase heat transfer enhancement techniques in heat exchanger applications," *Renew. Sustain. Energy Rev.*, vol. 81, no. June 2017, pp. 813–839, 2018, doi: 10.1016/j.rser.2017.08.060.

[8] L. Léal *et al.*, "An overview of heat transfer enhancement methods and new perspectives: Focus on active methods using electroactive materials," *Int. J. Heat Mass Transf.*, vol. 61, no. 1, pp. 505–524, 2013, doi: 10.1016/j.ijheatmasstransfer.2013.01.083.

[9] M. Al-Maghalseh and K. Mahkamov, "Methods of heat transfer intensification in PCM

thermal storage systems: Review paper," *Renew. Sustain. Energy Rev.*, vol. 92, no. September 2016, pp. 62–94, 2018, doi: 10.1016/j.rser.2018.04.064.

[10] Y. B. Tao and Y. L. He, "A review of phase change material and performance enhancement method for latent heat storage system," *Renew. Sustain. Energy Rev.*, vol. 93, no. December 2016, pp. 245–259, 2018, doi: 10.1016/j.rser.2018.05.028.

[11] P. Sivasamy, A. Devaraju, and S. Harikrishnan, "Review on Heat Transfer Enhancement of Phase Change Materials (PCMs)," *Mater. Today Proc.*, vol. 5, no. 6, pp. 14423–14431, 2018, doi: 10.1016/j.matpr.2018.03.028.

[12] M. Amin, N. Putra, E. A. Kosasih, E. Prawiro, R. A. Luanto, and T. M. I. Mahlia, "Thermal properties of beeswax/graphene phase change material as energy storage for building applications," *Appl. Therm. Eng.*, vol. 112, pp. 273–280, 2017, doi: 10.1016/j.applthermaleng.2016.10.085.

[13] J. Yang *et al.*, "Hybrid graphene aerogels/phase change material composites: Thermal conductivity, shape-stabilization and light-to-thermal energy storage," *Carbon N. Y.*, vol. 100, pp. 693–702, 2016, doi: 10.1016/j.carbon.2016.01.063.

[14] T. Xu, Q. Chen, G. Huang, Z. Zhang, X. Gao, and S. Lu, "Preparation and thermal energy storage properties of d-Mannitol/expanded graphite composite phase change material," *Sol. Energy Mater. Sol. Cells*, vol. 155, pp. 141–146, 2016, doi: 10.1016/j.solmat.2016.06.003.

[15] M. Li and Z. Wu, "Thermal properties of the graphite/n-docosane composite PCM," *J. Therm. Anal. Calorim.*, vol. 111, no. 1, pp. 77–83, 2013, doi: 10.1007/s10973-012-2218-5.

[16] S. Yu, X. Wang, and D. Wu, "Microencapsulation of n-octadecane phase change material with calcium carbonate shell for enhancement of thermal conductivity and serving durability: Synthesis, microstructure, and performance evaluation," *Appl. Energy*, vol. 114, pp. 632–643, 2014, doi: 10.1016/j.apenergy.2013.10.029.

[17] T. Wang, S. Wang, R. Luo, C. Zhu, T. Akiyama, and Z. Zhang, "Microencapsulation of phase change materials with binary cores and calcium carbonate shell for thermal energy storage," *Appl. Energy*, vol. 171, pp. 113–119, 2016, doi: 10.1016/j.apenergy.2016.03.037.

[18] J. Zhang, T. Zhao, Y. Chai, and L. Wang, "Preparation and Characterization of High Content Paraffin Wax Microcapsules and Micro/Nanocapsules with Poly Methyl Methacrylate Shell by Suspension-Like Polymerization," *Chinese J. Chem.*, vol. 35, no. 4, pp. 497–506, 2017, doi: 10.1002/cjoc.201600631.

[19] Z. Liu, X. Sun, and C. Ma, "Experimental investigations on the characteristics of melting processes of stearic acid in an annulus and its thermal conductivity enhancement by fins," *Energy Convers. Manag.*, vol. 46, no. 6, pp. 959–969, 2005, doi: 10.1016/j.enconman.2004.05.012.

[20] A. Gil, G. Peiró, E. Oró, and L. F. Cabeza, "Experimental analysis of the effective thermal conductivity enhancement of PCM using finned tubes in high temperature bulk tanks," *Appl. Therm. Eng.*, vol. 142, no. July, pp. 736–744, 2018, doi: 10.1016/j.applthermaleng.2018.07.029.

[21] G. J. McGranaghan and A. J. Robinson, "The mechanisms of heat transfer during convective boiling under the influence of AC electric fields," *Int. J. Heat Mass Transf.*,

vol. 73, pp. 376–388, 2014, doi: 10.1016/j.ijheatmasstransfer.2014.01.050.

[22] Q. Li and Y. Xuan, "Experimental investigation on heat transfer characteristics of magnetic fluid flow around a fine wire under the influence of an external magnetic field," *Exp. Therm. Fluid Sci.*, vol. 33, no. 4, pp. 591–596, 2009, doi: 10.1016/j.expthermflusci.2008.12.003.

[23] Y. K. Oh, S. H. Park, and Y. I. Cho, "A study of the effect of ultrasonic vibrations on phase-change heat transfer," *Int. J. Heat Mass Transf.*, vol. 45, no. 23, pp. 4631–4641, 2002, doi: 10.1016/S0017-9310(02)00162-X.

[24] H. Li, R. You, H. Deng, Z. Tao, and J. Zhu, "Heat transfer investigation in a rotating U-turn smooth channel with irregular cross-section," *Int. J. Heat Mass Transf.*, vol. 96, pp. 267–277, 2016, doi: 10.1016/j.ijheatmasstransfer.2015.12.071.

[25] T. Nishimura and S. Matsune, "Vortices and wall shear stresses in asymmetric and symmetric channels with sinusoidal wavy walls for pulsatile flow at low Reynolds numbers," *Int. J. Heat Fluid Flow*, vol. 19, no. 6, pp. 583–593, 1998, doi: 10.1016/S0142-727X(98)10005-X.

[26] B. Chu, "No Title," *Phys. Fluids*, vol. 2.5, pp. 473–484, 1959.

[27] H. N. Yoshikawa, O. Crumeyrolle, and I. Mutabazi, "Dielectrophoretic force-driven thermal convection in annular geometry," *Phys. Fluids*, vol. 25, no. 2, 2013, doi: 10.1063/1.4792833.

[28] H. Sadek, C. Y. Ching, and J. Cotton, "The effect of pulsed electric fields on horizontal tube side convective condensation," *Int. J. Heat Mass Transf.*, vol. 53, no. 19–20, pp. 3721–3732, 2010, doi: 10.1016/j.ijheatmasstransfer.2010.04.023.

[29] H. Omidvarborna, M. Dasht-e-Bayz, A. Mehrabani-Zeinabad, and M. Nasr Esfahany, “Effect of applied EHD on in-tube condensation of R-134a within an assembled experimental rig including a laboratory heat exchanger,” *Exp. Therm. Fluid Sci.*, vol. 58, pp. 112–120, 2014, doi: 10.1016/j.expthermflusci.2014.06.007.

[30] D. V. Fernandes, H. D. Lee, S. Alapati, and Y. K. Suh, “Numerical simulation of the electro-convective onset and complex flows of dielectric liquid in an annulus,” *J. Mech. Sci. Technol.*, vol. 26, no. 12, pp. 3785–3793, 2012, doi: 10.1007/s12206-012-1005-3.

[31] M. Yazdani and J. S. Yagoobi, “The effect of uni/bipolar charge injection on EHD conduction pumping,” *J. Electrostat.*, vol. 75, pp. 43–48, 2015, doi: 10.1016/j.elstat.2015.03.008.

[32] M. Daaboul, P. Traoré, P. Vázquez, and C. Louste, “Study of the transition from conduction to injection in an electrohydrodynamic flow in blade-plane geometry,” *J. Electrostat.*, vol. 88, pp. 71–75, 2017, doi: 10.1016/j.elstat.2017.01.014.

[33] “1984, Takashima - The Stability of Natural Convection in a Vertical Layer of Dielectric Fluid in the Presence of a horizontal ac.pdf.”

[34] P. H. G. Allen and T. G. Karayiannis, “Electrohydrodynamic enhancement of heat transfer and fluid flow,” *Heat Recover. Syst. CHP*, vol. 15, no. 5, pp. 389–423, 1995, doi: 10.1016/0890-4332(95)90050-0.

[35] Y. Peng, D. Li, X. Yang, Z. Ma, and Z. Mao, “A Review on Electrohydrodynamic (EHD) Pump,” *Micromachines*, vol. 14, no. 2, pp. 1–23, 2023, doi: 10.3390/mi14020321.

[36] S. Ould Ahmedou and M. Havet, “Effect of process parameters on the EHD airflow,” *J. Electrostat.*, vol. 67, no. 2–3, pp. 222–227, 2009, doi: 10.1016/j.elstat.2009.01.055.

[37] Dellorusso, Paul Robert. Electrohydrodynamic heat transfer enhancement for a latent heat storage heat exchanger. DalTech-Dalhousie University, 1999.

[38] E. Thompson, "Electrohydrodynamic solidification of phase change materials," 2017,

[39] D. Nakhla, H. Sadek, and J. S. Cotton, "Melting performance enhancement in latent heat storage module using solid extraction electrohydrodynamics (EHD)," *Int. J. Heat Mass Transf.*, vol. 81, pp. 695–704, 2015, doi: 10.1016/j.ijheatmasstransfer.2014.10.016.

[40] D. Nakhla, E. Thompson, B. Lacroix, and J. S. Cotton, "Measurement of heat transfer enhancement in melting of n-Octadecane under gravitational and electrohydrodynamics (EHD) forces," *J. Electrostat.*, vol. 92, no. January, pp. 31–37, 2018, doi: 10.1016/j.elstat.2018.01.004.

[41] D. Nakhla and J. S. Cotton, "Effect of electrohydrodynamic (EHD) forces on charging of a vertical latent heat thermal storage module filled with octadecane," *Int. J. Heat Mass Transf.*, vol. 167, p. 120828, 2021, doi: 10.1016/j.ijheatmasstransfer.2020.120828.

[42] Z. Sun, P. Yang, K. Luo, and J. Wu, "Experimental investigation on the melting characteristics of n-octadecane with electric field inside macrocapsule," *Int. J. Heat Mass Transf.*, vol. 173, p. 121238, 2021, doi: 10.1016/j.ijheatmasstransfer.2021.121238.

[43] Z. Sun, Y. Zhang, K. Luo, A. T. Pérez, H. Yi, and J. Wu, "Experimental investigation on melting heat transfer of an organic material under electric field," *Exp. Therm. Fluid Sci.*, vol. 131, no. October 2021, 2022, doi: 10.1016/j.expthermflusci.2021.110530.

[44] Z. Sun, K. Luo, H. Yi, and J. Wu, "Experimental study on the melting heat transfer of octadecane with passively adding graphene and actively applying an electric field," *Int. J. Heat Mass Transf.*, vol. 204, 2023, doi: 10.1016/j.ijheatmasstransfer.2023.123845.

[45] J. Wu, P. A. Vázquez, P. Traoré, and A. T. Pérez, "Finite amplitude electroconvection induced by strong unipolar injection between two coaxial cylinders," *Phys. Fluids*, vol. 26, no. 12, 2014, doi: 10.1063/1.4903284.

[46] Y. Stishkov and V. Chirkov, "Dependence of the electrohydrodynamic flows structure in very non-uniform electric field on the charge formation mechanism," *Proc. - IEEE Int. Conf. Dielectr. Liq.*, pp. 1–4, 2011, doi: 10.1109/ICDL.2011.6015482.

[47] V. A. Chirkov and Y. K. Stishkov, "Current-time characteristic of the transient regime of electrohydrodynamic flow formation," *J. Electrostat.*, vol. 71, no. 3, pp. 484–488, 2013, doi: 10.1016/j.elstat.2012.12.005.

[48] K. Luo, A. T. Pérez, J. Wu, H. L. Yi, and H. P. Tan, "Efficient lattice Boltzmann method for electrohydrodynamic solid-liquid phase change," *Phys. Rev. E*, vol. 100, no. 1, pp. 1–15, 2019, doi: 10.1103/PhysRevE.100.013306.

[49] C. L. Lu, X. L. Gao, J. Wu, K. Luo, and H. L. Yi, "Heat transfer enhancement analysis of electrohydrodynamic solid-liquid phase change via lattice Boltzmann method," *Appl. Therm. Eng.*, vol. 194, no. November 2020, p. 117112, 2021, doi: 10.1016/j.applthermaleng.2021.117112.

[50] R. D. Selvakumar, L. Qiang, L. Kang, P. Traoré, and J. Wu, "Numerical modeling of solid-liquid phase change under the influence an external electric field," *Int. J. Multiph. Flow*, vol. 136, p. 103550, 2021, doi: 10.1016/j.ijmultiphaseflow.2020.103550.

[51] R. D. Selvakumar and S. Vengadesan, "Combined effects of buoyancy and electric forces on non-isothermal melting of a dielectric phase change material," *Int. J. Multiph. Flow*, vol. 151, no. December 2021, 2022, doi: 10.1016/j.ijmultiphaseflow.2022.104029.

[52] K. He, L. Wang, and J. Huang, “Electrohydrodynamic enhancement of phase change material melting in circular-elliptical annuli,” *Energies*, vol. 14, no. 23, pp. 1–20, 2021, doi: 10.3390/en14238090.

[53] K. He, B. Ma, and L. Wang, “Electrohydrodynamic enhancement of phase change material melting in cylindrical annuli under microgravity,” *Appl. Therm. Eng.*, vol. 215, no. June, p. 119005, 2022, doi: 10.1016/j.applthermaleng.2022.119005.

[54] R. D. Selvakumar, J. Wu, I. Afgan, Y. Ding, and A. K. Alkaabi, “Melting performance enhancement in a thermal energy storage unit using active vortex generation by electric field,” *J. Energy Storage*, vol. 67, no. February, p. 107593, 2023, doi: 10.1016/j.est.2023.107593.

[55] H. E. Endigeri, R. Deepak Selvakumar, and S. Vengadesan, “Solid-liquid phase change subjected to unipolar charge injection from a circular wire electrode,” *Int. J. Heat Mass Transf.*, vol. 194, p. 123120, 2022, doi: 10.1016/j.ijheatmasstransfer.2022.123120.

[56] H. Sadek, A. J. Robinson, J. S. Cotton, C. Y. Ching, and M. Shoukri, “Electrohydrodynamic enhancement of in-tube convective condensation heat transfer,” *Int. J. Heat Mass Transf.*, vol. 49, no. 9–10, pp. 1647–1657, 2006, doi: 10.1016/j.ijheatmasstransfer.2005.10.030.

[57] S. Nangle-Smith, H. Sadek, and J. S. Cotton, “The influence of the electrophoretic and polarization forces on two phase flow redistribution in a horizontal annular tube,” *Int. J. Plasma Environ. Sci. Technol.*, vol. 7, no. 1, pp. 64–70, 2013.

[58] Z. Sun, D. Sun, J. Hu, P. Traoré, H. L. Yi, and J. Wu, “Experimental study on electrohydrodynamic flows of a dielectric liquid in a needle-plate configuration under

direct/alternating current electric field," *J. Electrostat.*, vol. 106, no. October 2019, 2020, doi: 10.1016/j.elstat.2020.103454.

Chapter 2: Investigation of the role of electrohydrodynamic forces on the heat transfer enhancement and solid extraction during melting of paraffin wax under constant temperature boundary conditions

Investigation of the role of electrohydrodynamic forces on the heat transfer enhancement and solid extraction during melting of paraffin wax under constant temperature boundary conditions

Ahmed Hassan, James S. Cotton*,

McMaster University, Department of Mechanical Engineering, Hamilton, Ontario, Canada

*Corresponding Author: cottonjs@mcmaster.ca

ABSTRACT

The melting enhancement of paraffin wax is studied experimentally under the effect of electrohydrodynamic (EHD). Paraffin wax was melted under constant temperature boundary conditions with different applied DC voltage magnitudes and polarities, and different temperature gradients. The role of EHD forces was investigated by applying DC and AC square waves with different frequencies and offset values.

It was found that the melting enhancement rises nonlinearly with increasing the voltage magnitudes. The maximum effective thermal conductivity under -10 kV was found to be 0.95 W/m-K in comparison with the value of 0.2 W/m-K for the pure liquid paraffin wax, with an enhancement ratio of 4.75.

The EHD solid extraction phenomenon investigation showed that the extraction was detected for all the applied DC voltages. Small dendrites were observed to be pulled out from the mushy zone melt front and rise upwards in a rotational manner. It is concluded that the Coulomb force is the primary force for extraction while the formation of electroconvection cells is the main driving

mechanism for the motion of the suspended dendrites in the liquid bulk. In addition, the AC studies revealed that the dielectrophoretic force is negligible in this study.

Nomenclature

A	Area
E	Electric field strength
f	Force
H	Cell height
k	Thermal conductivity
q	Space charge density
Q	Heat flux
S	Thickness
T	Temperature
V	Voltage
Greek symbols	
ε	Dielectric constant
ρ	Density
τ	Charge relaxation time
Subscripts	
c	Cold
eff	Effective
h	Hot
l	Liquid
m	Mushy
mh	High melting point
ml	Low melting point
s	Solid

2.1 Introduction

Thermal energy storage is considered one of the most effective techniques in bridging the gap between the energy supply and consumer demand. The thermal storage systems are either sensible, latent, or thermochemical type. The latent thermal storage is more favorable in certain applications as the energy is stored at nearly constant temperature which gives better control over the system and has the advantage of its high energy density which leads to smaller system size and weight [1].

Latent energy storage requires the use of phase change materials (PCMs) in thermal systems. PCMs have the advantage of their high latent heat capacity which enables the storage of higher energy in smaller volumes. However, the very low thermal conductivity of PCMs, [0.1 – 0.6 W/m-k], is a major problem as it results in low heat transfer rates of energy charging and discharging, which reduces the performance of such systems [2,3]. Different techniques have been implemented to enhance the thermal performance of PCMs. The heat transfer enhancement techniques are either passive or active type. The passive methods require no external power where the system usually needs special surface geometries or adding fluid additives of high thermal conductivity such as carbon fiber and graphene [4,5].

For the active methods, an external power source is applied such as magnetic field, electric field, and surface vibration. One advantage of these methods is their capability of controlling the heat transfer based on the system requirements [6]. One of the most promising methods for this type is the electrohydrodynamic (EHD) technique. EHD requires the application of high voltage into a dielectric medium to create an electric field. The generated electric field creates electrical body forces in the fluid and interfacial forces at the solid-liquid interface. The EHD force acting on a dielectric fluid per unit volume can be formulated as [7]:

$$\bar{f}_{EHD} = q\bar{E} - \frac{1}{2}E^2\nabla\varepsilon + \frac{1}{2}\nabla[\rho E^2\left(\frac{\partial\varepsilon}{\partial\rho}\right)_T] \qquad (1)$$

The first term of equation (1) represents the electrophoretic (Coulomb force). This force is generated by the application of electric field [E] on the free charges [q] in the fluid. The charges can be created through injection where free charges are directly injected from the electrodes, or conduction where the charges are generated by dissociation of molecules in the liquid volume [8]. Charge injection mechanism will be dominant over the conduction mechanism in case of the application of very high electric field in liquids of low electrical conductivity [9]. In case of charge injection, the free charges are accumulating over a timescale called the charge relaxation time ($\tau_e = {}^{\varepsilon}/_{\sigma}$), where ε and σ are the dielectric constant and electrical conductivity of the medium. This time scale affects the motion of charges within the medium. Another time scale that influences the accumulation of charges in the fluid is the ionic transit time which is the time taken by the charges to reach the collector electrode. The Coulomb force can be suppressed under high frequency AC voltages with a wave period that is smaller than the shortest electrical time scales, as the charges will not have enough time to respond to the voltage variation [10,11]. The second and third terms of equation (1) are the dielectrophoretic and electrostrictive forces, respectively. These forces become significant in two-phase systems where there is a gradient in fluid permittivity. For the dielectrophoretic force, a spatial change in permittivity is needed which can be created by nonuniform electric field. Also, this force is effective at the interface between the different phases that have a measurable difference in dielectric constant, or in the bulk of the fluid with a high temperature gradient that creates a gradient in permittivity. The electrostrictive force is significant when there is a change in permittivity with density including liquid vapor interfaces and compressible systems [12,13], however this force becomes zero in confined solid-liquid systems.

In two phase solid-liquid systems, there are two main mechanisms for the heat transfer enhancement. The first is the generation of a secondary motion inside the liquid as a result of the electrical body (EHD) forces. This secondary motion, which is in the form of electroconvection cells disturbs the thermal boundary layer and thus increases the heat transfer coefficient [14-16]. The other enhancement mechanism is the solid extraction where solid dendrites are pulled out by the interfacial forces from the solid-liquid interface into the liquid volume causing higher melting rates. This phenomenon was recently detected and identified by Nakhla et al. [17].

The effect of EHD on the heat transfer enhancement in latent heat solid-liquid systems has been investigated for both melting and solidification processes. In conduction dominated melting, Nakhla et al. [17] studied the EHD melting of paraffin wax under constant heat flux boundary condition. It was shown that the application of EHD under -8 kV can decrease the melting time taken for the melt thickness to reach 7 mm by 40% for the lowest heat flux case (7.1 W). Also, it was shown that the EHD enhancement becomes lower by increasing the heat flux. In this study, the solid extraction phenomenon was detected using high speed imaging and it was observed that the extracted dendrites are attracted to the electrode and melted as they migrate into higher temperature regions which aided the melting enhancement. In a later study, Nakhla et al. [18] studied the EHD melting of Octadecane under constant temperature boundary conditions. The results showed that the steady state melt thickness increases by 17 mm when EHD is applied at 10 kV. The main mechanism for the enhancement in this study was found to be the electrophoretic force, while the role of the dielectrophoretic effect is negligible. Also, it was found that there is no solid extraction detected under EHD melting. This was attributed to the absence of the mushy zone in the Octadecane.

Mixing electrical and gravitational flow is studied experimentally during melting of Octadecane in a vertically oriented test section under 3 and 6 kV [19]. The EHD effect on the local heat transfer coefficient was quantified by measuring the local temperature gradient at the heat transfer wall using shadowgraph method. The results showed that the melting is electrically dominated in the early stages of melting where the presence of two opposing electroconvection cells is observed between each two rows of electrodes. As melting progresses, the gravitational effect is intensified, and a mixed electrical and gravitational flow exists. Also, it was found that the local heat transfer coefficient rises to 3-fold by the application of EHD under 6 kV. In a numerical study, Selvakumar and Vengadesan [20] also investigated the combined effect of the EHD forces and the buoyancy force during non-isothermal melting of PCM in a 2D rectangular cavity. It was found that the melting shifted from a buoyancy dominated melting to EHD force dominated melting after a deflection point at which an increase in the melting rate is observed. The shift to strong EHD flow was detected in the velocity field where several smaller convective cells and oscillating charge void regions are created.

Sun et al. [21] experimentally studied melting n-Octadecane in a microcapsule (4 cm * 4 cm). Melting occurs by maintaining the vertical sides at hot and cold temperatures. The author examined the effect of electrohydrodynamic on the melting performance and the velocity field generated in the liquid phase by applying positive and negative high voltages on one of the heat exchangers while grounding the other. When the voltage is applied to the hot heat exchanger, the electric field was found to hinder the melting where the liquid fraction decreased by about 30% at 20 kV applied voltage. By reversing the electrodes and applying the electric potential at the cold heat exchanger, the melting was enhanced, and liquid fraction increased by 43%. In the later study, Sun et al. [22] studied the melting of n-Octadecane with a different configuration. The PCM is melted in a rectangular cavity with a cylindrical heat exchanger placed at the center of the cavity. The cylinder is connected to the high voltage side while the bottom surface is grounded. The EHD application showed no enhancement with the lowest voltage applied (5 kV). By increasing the voltage to 15 and 25 kV, the melting performance was better when compared to the non-EHD case. When comparing the positive and the negative polarity, the author found that the negative electric potential always showed better results than the positive cases.

For solidification heat transfer under the effect of EHD, Thompson [23] investigated the solidification of Octadecane under EHD effects. The experimental results showed very little enhancement with the application of EHD under -8 kV.

Previous studies showed that the effect of EHD on heat transfer enhancement depends on the interaction of the thermal, electrical, and gravitational fields. Heat transfer can be enhanced when electroconvection is created as a result of an electrically dominated or a mixed electrical and gravitational melting regime. Also, it can be concluded from the previous studies that the role of each of Coulomb force and dielectrophoretic force on the enhancement is not clear in literature.

In the current study, the melting of paraffin wax, having a large mushy zone, under EHD effect is investigated. The PCM is melted under constant temperature boundary conditions in a forced conduction dominated heat transfer regime until steady state condition is reached. After that, the high voltage is applied and the increase in melt fraction is determined. The effect of different DC applied voltages with different polarities, and different temperature boundaries are examined. AC square wave forms are also investigated with different frequencies and offset values to study the role of the different EHD forces on the melting enhancement. Finally, high speed imaging is conducted for visualizing the solid extraction phenomenon and investigating its behavior.

2.2 Experimental facility and data reduction

The experimental test facility was designed for melting phase change materials in a conduction dominating heat transfer under constant temperature boundary conditions. The phase change material used in the experiments is paraffin wax. Paraffin wax was chosen because of its large mushy zone due to its high melting range (53 - 63 °C). This large mushy zone can create a large volume where extracted dendrites may exist and get charged, and a high nonuniform electric field can be generated due to the gradient in the dielectric constant in this region. The breakdown voltage for paraffin wax was calculated theoretically for the current electrode design and was found to be approximately equal to 40 kV. The experimental breakdown voltage was found to be lower (~12.5 kV) for the test section as breakdown tended to occur either outside of the facility or at the electrode test facility interface. Therefore, the maximum voltage applied in the experiments is set to be 10 kV. The thermophysical properties of paraffin wax are listed in Table 4.

Table 4: Thermophysical properties of paraffin wax.

Property	Value
Melting temperatures [DSC test]	53-63 °C
Density [24]	825 (solid) – 755 (liquid) [kg/m^3]
Thermal conductivity [24]	0.23 (solid) – 0.2 (liquid) [W/m k]
Specific heat capacity [DSC test]	2.1 [kJ/kg K]
Electrical permittivity (liquid)	2.1
Latent heat of fusion [1]	190 [kJ/kg]

The schematic of the experimental facility is presented in Fig. 5. The PCM is contained in a rectangular enclosure made of acrylic which allows for visualization due to its transparency. Two heat exchangers are installed at the top and the bottom of the test section. The constant temperature boundary condition is maintained by supplying the heat exchangers with near constant temperature water from two thermal baths NESLAB RTE-10 and PolyScience AP15R-30. The top heat exchanger is maintained at hot temperature (T_h) while the bottom heat exchanger is maintained at cold temperature (T_c). Hence, the melting will be progressing downwards in a conduction melting regime. A riser is installed on the top heat exchanger to allow for thermal expansion during melting. A glass wool thermal insulation of 20 mm thickness is installed on all sides of the test section to minimize the heat losses to the surroundings. The heat losses were assessed and minimized using a CFD transient melting model of the test section.

For the application of EHD, two rows of cylindrical copper electrodes are arranged horizontally inside the enclosure as shown in Fig. 5. The high voltage is supplied by TREK 20/20C high voltage amplifier with an amplification factor of 2000:1. The electrodes are connected to the high voltage side while the heat exchangers are grounded. The voltage magnitudes and wave forms are controlled using Tektronix AFG 3021B function generator. Electric current is measured at the ground side using Keithley DMM 6500 digital reader with a reading sensitivity of 10 pA.

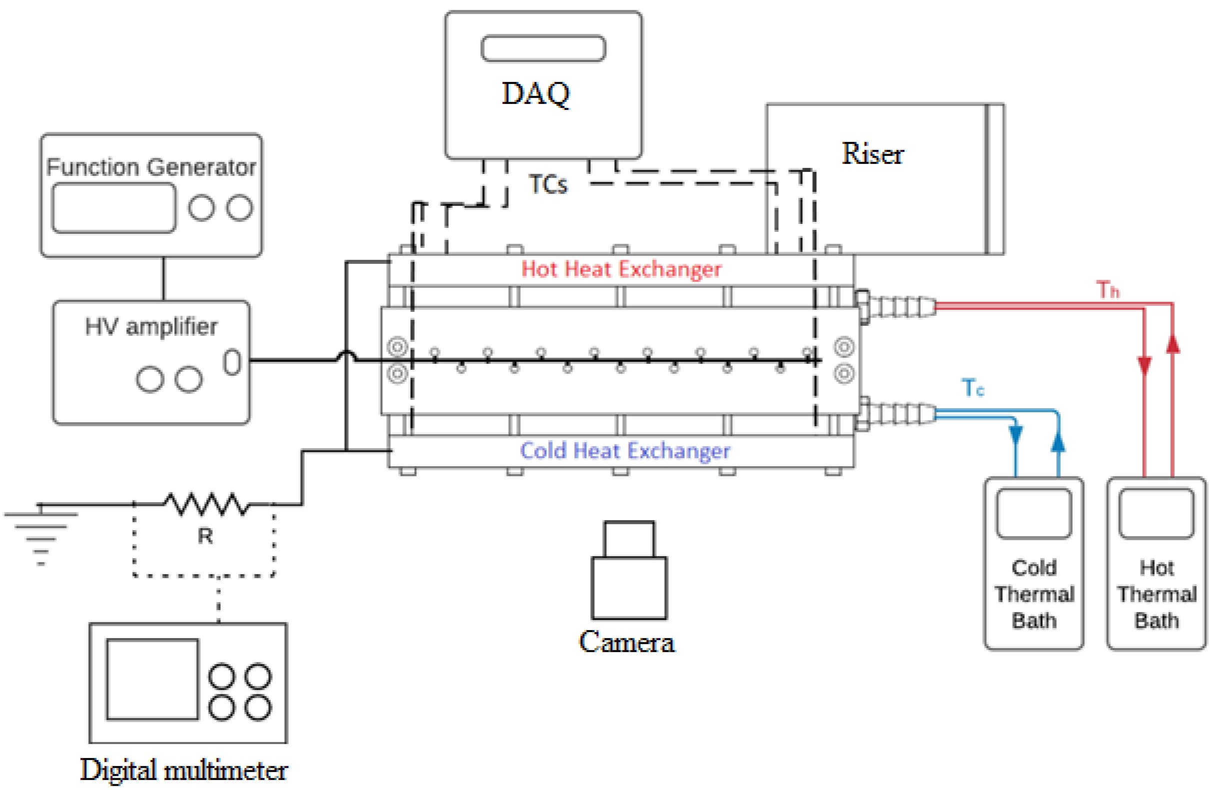

Fig. 5. Experimental Constant Temperature Boundary EHD Test Facility

Type T thermocouples are used to measure the temperatures of the heat exchangers at four different positions on the top and bottom surfaces to ensure being at nearly constant temperatures. The maximum allowable temperature deviation along the heat transfer surfaces was set to be 0.3 °C. Another type T thermocouple is used to record the ambient temperature during the experiments. All the experiments are conducted within an ambient temperature range of 23 – 25 °C. The thermocouples are connected to a data acquisition card (NI-DAQ 9211) which is connected to a computer for monitoring and control. The uncertainty of the temperature readings is ±0.2 °C.

Images for the PCM melt front locations with time were captured by a time lapse camera Nikon D5200. The images are then analyzed by ImageJ software to determine the melting fraction. Images were taken every 1 hour until steady state condition is reached when the change in the melt fraction does not exceed 1% within a one-hour period. After that, the EHD is turned on and the melting started again due to the EHD enhancement effect. Melt front locations are recorded until the EHD steady state condition was achieved. The uncertainty of the calculated melt fraction was ±1 %. For the detection and visualization of the solid extraction phenomenon, high-speed imaging is taken using a FASTCAM SA4 high-speed camera with a frame rate of 125 f/s.

Thermal and electrical degradation of PCMs could occur when subjected to successive thermal cycles of melting and solidification. It was found that the latent heat of Paraffin wax decreases over 100 thermal cycles while the melting temperature increases [26-28]. To avoid PCM deterioration with successive thermal cycling, the paraffin wax used in the experiments was replaced twice with a new sample where the test section was completely emptied, cleaned, and then refilled with the new PCM to test repeatability. The results for the conducted melting experiments showed a very good repeatability within the uncertainty of the measurements.

2.2.1 Data reduction

Effective thermal conductivity (k_{eff}) will be used to represent the amount of heat transfer enhancement due to the application of EHD. This can facilitate the comparison between different cases with different enhancement techniques. The heat flux through the liquid region with the application of EHD can be represented by the conduction relation for heat transfer with the utilization of k_{eff}. It can be expressed as:

$$Q_{EHD,l} = k_{Eff} * \frac{A(T_h - T_{mh})}{S_{l,EHD}} \quad (2)$$

Where $S_{l,EHD}$ is the steady state EHD liquid melt thickness determined from the experimental melt front images and A is the heat transfer area. T_h and T_{mh} are the upper hot temperature of the top heating surface and the PCM higher melting temperature, which is the lower temperature limit of the liquid region, respectively. The temperature limits for the different melting phases are illustrated in Fig. 6.

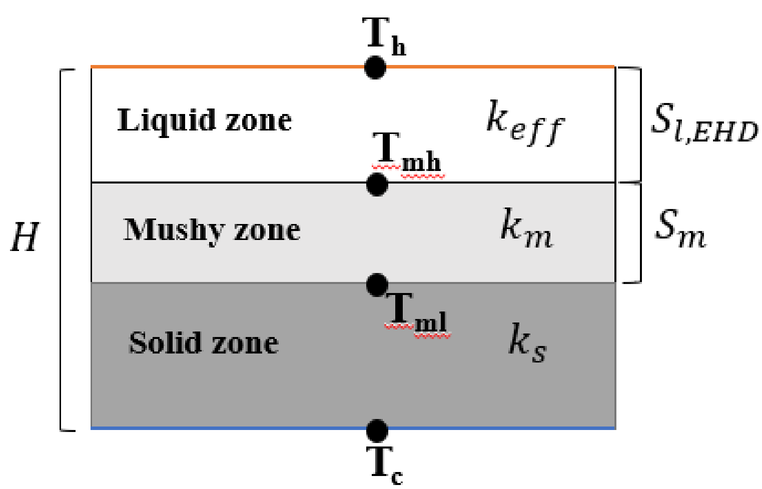

Fig. 6. Illustration for the different phases and temperature limits during EHD melting of Paraffin wax

To determine the heat transfer through the liquid phase ($Q_{EHD,l}$), heat balance is applied on the three existing phases at steady state melting, where the heat flux through the liquid, mushy and solid phases can be assumed to be the same.

$$Q_{EHD,l} = Q_{EHD,mushy} = Q_{EHD,solid} \qquad (3)$$

Since the heat transfer in the solid and mushy phases are by conduction only, the heat balance can be written as:

$$Q_{EHD,l} = \frac{A*k_m*(T_{mh}-T_{ml})}{S_m} = \frac{A*k_s*(T_{ml}-T_c)}{(H-S_{l,EHD}-S_m)} \qquad (4)$$

Where T_{ml} and T_c are the PCM lower melting temperature and the lower cold temperature of the bottom heating surface respectively. k_m and k_s are the thermal conductivities for the mushy and solid phases, S_m is the mushy thickness, and H is the cell height. The thermal conductivity for the mushy zone (k_m) is assumed to be the average of the conductivities of the liquid and the solid phases assuming 50% porosity for the mushy region. From equation (4), S_m can be eliminated and the EHD heat flux can be represented as:

$$Q_{EHD,l} = \frac{k_m(T_{mh}-T_{ml})+k_s(T_{ml}-T_c)}{H-S_{l,EHD}} \qquad (5)$$

By integrating equation (5) into equation (1), the effective thermal conductivity is derived to be:

$$k_{Eff} = \frac{S_{l,EHD}[k_m(T_{mh}-T_{ml})+k_s(T_{ml}-T_c)]}{(H-S_{l,EHD})(T_h-T_{mh})} \qquad (6)$$

The effective thermal conductivity can be determined by measuring the EHD melt thickness from the experimental melt front images. The propagation of error analysis showed that the uncertainty of the effective thermal conductivity is ±0.02 W/m-K.

2.3 Results and Discussion

2.3.1 Electric field simulation

The role of the EHD forces on the heat transfer enhancement depends on the electric field distribution. Therefore, the electrostatic field for the solid-liquid PCM medium is simulated for better understanding of the experimental results. Comsol software is used for solving Gauss law and Poisson's equation which are relating the electric potential and electric field as:

$$E = -\nabla V \quad (7)$$

$$\nabla^2 V = -q/\varepsilon \quad (8)$$

Where E is the electric field, V is the electric potential, q is the space charge, and ε is the electric permittivity. A 2D domain that is identical to the experimental test section was constructed. The electrical properties of paraffin wax were defined for the domain material where the dielectric constants for the solid and liquid phases are 2.5 and 2.25 respectively. The space charge density is assumed to be zero. The boundary conditions at the electrode surfaces are set to constant electric potential (V = 6000 V), while the top and bottom surfaces are set to have ground boundary conditions (V=0).

The distribution of the electric field strength at different melt front positions is presented in Fig. 7. The gradient of the electric field is high at regions of top of upper rows of electrodes and at the bottom of the lower rows. The maximum electric field strength at the vicinity of the electrodes is about $2*10^6$ V/m. It can be observed that the change in the distribution between the different cases is small as the difference in the electric permittivity of the solid and the liquid paraffin wax is very small.

When the solid-liquid interface is between the two rows of electrodes (Fig. 7a and 7b), the electric field directed upwards is stronger than that directed downwards. Thus, the resultant Coulomb force will be directed upwards in this case as long as a positive gradient in the space charge is generated at the vicinity of the electrodes. Therefore, electroconvection cells will be generated in the liquid region as a result of the Coulomb force. When the interface becomes below the lower electrodes (Fig. 7c), a very high gradient electric field appears that is directed downwards, which leads to lower EHD body forces in the liquid when compared to the former cases.

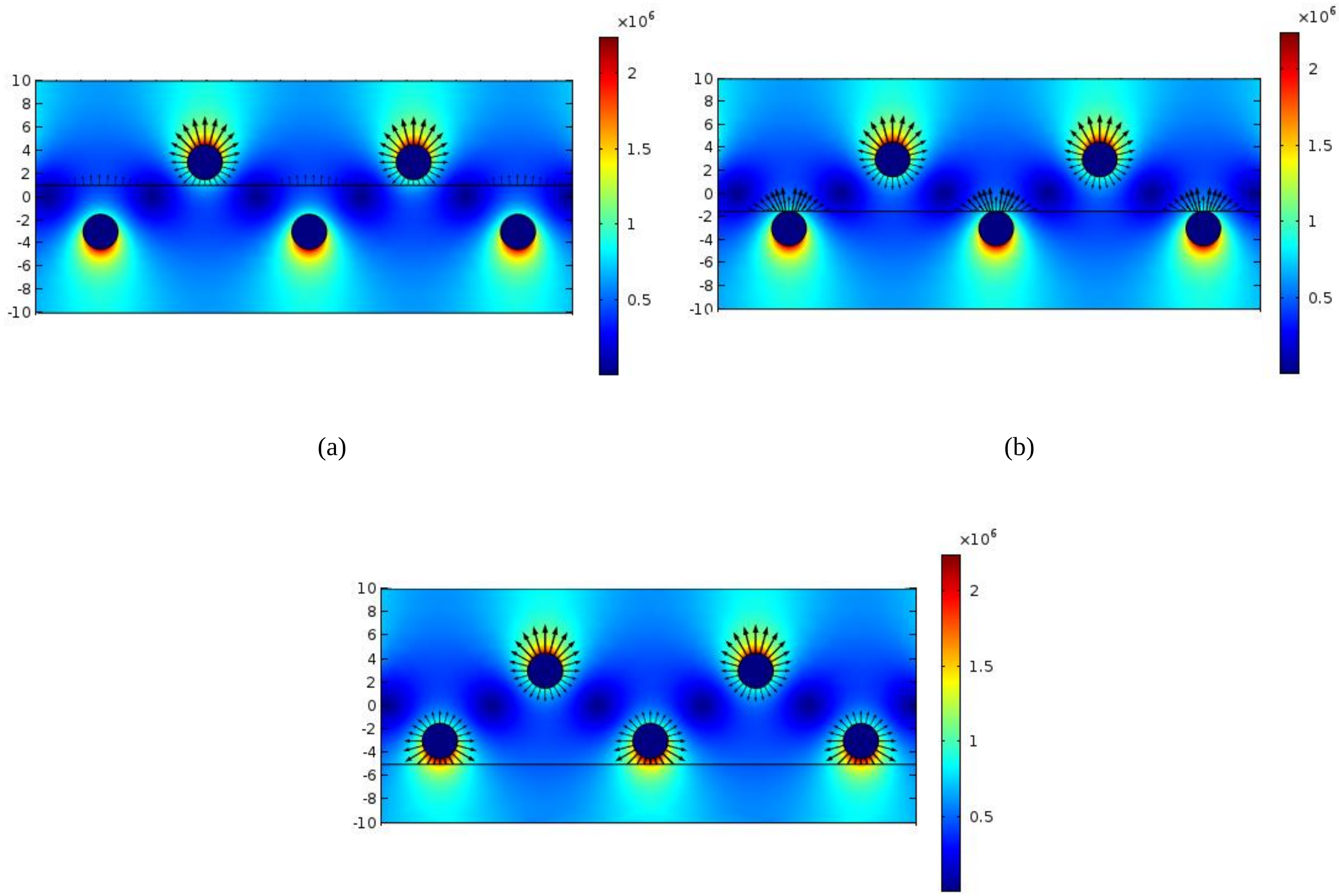

Fig. 7. *Electric field distribution at different melt front positions at 6 kV applied voltage*

2.3.2 Electric Current-Voltage Characteristics

Electric current measurements were conducted at different applied voltages for a completely melted PCM. The current was measured at the ground side of the test section using a digital reader. Fig. 8 shows the current-voltage characteristics for DC applied voltage up to 10 kV. The relation can be considered linear at low applied voltages up to 4 kV. After that, the current increases nonlinearly with the rise of voltages which indicates the domination of the charge injection from the electrodes. The maximum current obtained at the maximum applied voltage is 262 nA. Due to the very low current associated with EHD, the joule heating effect on the melting enhancement can be neglected.

The power consumption is calculated based on the measured current and the results are plotted in Fig. 9. The consumption increases nonlinearly with the increase of voltage due to the non-linear current-voltage relation. The maximum power consumption at 10 kV was found to be about 2.6 mW.

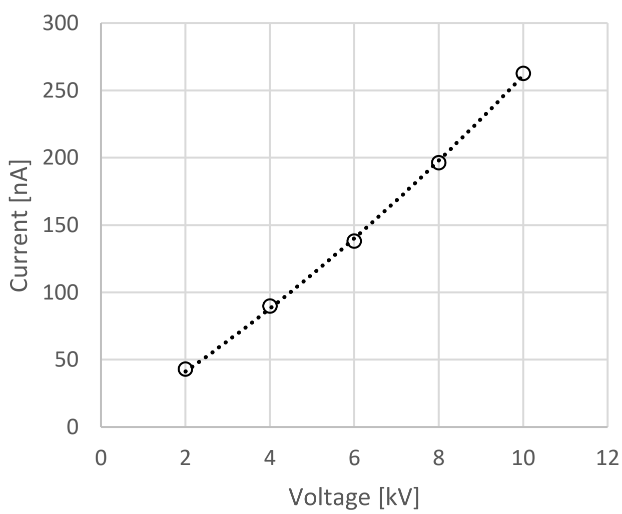

Fig. 8. Current-voltage characteristics for DC applied voltage

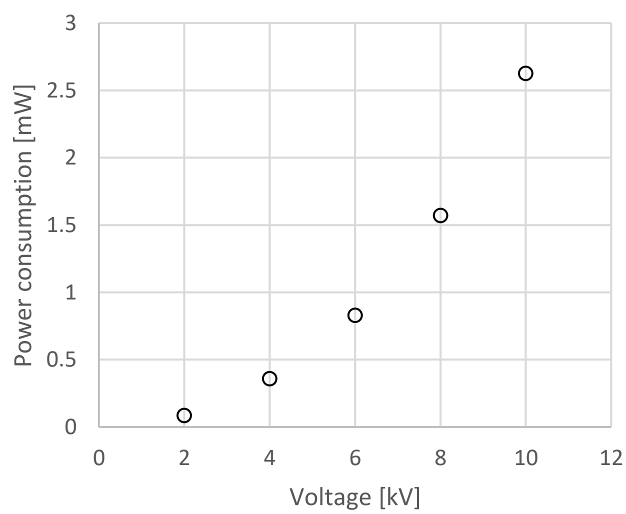

Fig. 9. Electric power consumption with voltage

2.3.3 Heat transfer Enhancement

In this section, the heat transfer enhancement under different applied DC and AC voltages will be presented. The effective thermal conductivity (Keff) is used to represent the amount of enhancement using the quasi-steady state assumption calculated at different melt front locations.

The heat transfer enhancement with EHD has been experimentally studied at different applied DC voltages for both positive and negative polarities. First, the threshold voltage at which the EHD comes into effect is determined. It was found that the lowest voltage at which EHD influenced the melt front took place at 400 V. At this case, the amount of enhancement was very small, and by increasing the voltage the enhancement rises until it becomes significant at an applied voltage of 2 kV. The EHD enhancement was investigated for voltages from 2 kV until a maximum applied voltage 10 kV, after which electric breakdown may occur. The variation of the effective thermal conductivities at EHD steady state with these voltage magnitudes is shown in Fig. 10. It is observed that the heat transfer enhancement is increasing approximately linearly with voltages until 6 kV. This is due to the increase in electric field as voltages increases which results in higher charge injection and thus larger Coulomb force. At higher voltages, greater than 6 kV, the enhancement continues to rise with a lower rate as the melt front becomes below the bottom row of electrodes. At this position (Fig. 7c), the gradient of the electric field is directed downwards which changes the flow and reduces the intensity of the Coulomb force. Also, when the second row of electrodes becomes located in the liquid region, the electroconvection cells will be subjected to higher damping effect due to their presence which results in lower velocity field and thus lower heat transfer. The maximum effective thermal conductivity determined at the highest applied voltages +10 kV is 0.93 W/m-K with an increase in thermal conductivity of 4.6-fold.

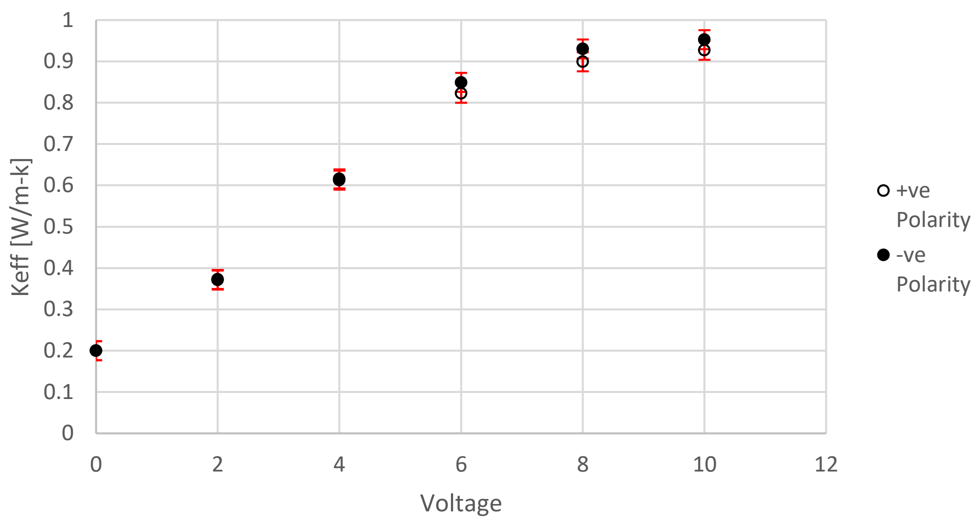

Fig. 10. EHD enhancement at different DC voltages for both positive and negative polarities

The effect of polarity is studied by applying negative DC voltages with the same amplitude values as for the positive polarities. It was found that the heat transfer enhancement is almost the same for both polarities at low voltages up to 4 kV. At higher voltages, the negative polarity showed a slightly higher enhancement than the positive voltage cases. This may be attributed to the higher electric mobility of the negative ions which results in higher electric current. The small variations for the enhancement between the different polarities is due to the very low electric current associated with the EHD application in this study. The maximum effective thermal conductivity reached for all cases is 0.95 W/m-K at -10 kV, which corresponds to a maximum enhancement ratio of 4.75.

The effect of the temperature boundaries on the EHD melting is presented in Fig. 11. Three different temperature boundary conditions were tested at 6 kV applied voltage, and it was found that the temperature has a very limited effect on the EHD heat transfer enhancement. The effective thermal conductivity is found to be increasing with time due to the rise in the melting thickness with the application of EHD until steady state is reached after about 90 minutes. The

EHD steady state melting enhancement reached for the 70 – 40 °C and 70 – 45 °C cases are the same with an effective thermal conductivity of 0.8 W/m-k. This is because of their similar temperature variations across the liquid region ($\Delta T_{liq} = 7$ ℃), which leads to a similar suppressive buoyancy effect caused by the temperature gradient across the liquid. Also, it is shown that the melting progress is slower for the 70 – 40 °C case as the melt front at non-EHD steady state is above the upper row of electrodes which acts as a heat sink and reduces the melting time. However, the enhancement observed for the 75 – 45 °C case was slightly lower than the other two cases with an effective thermal conductivity (k_{eff}) of 0.7 W/m-k. This is because of the higher temperature gradient across the liquid region for this case ($\Delta T_{liq} = 12$ ℃). This results in higher opposing buoyancy which leads to damping the electroconvection cells, which is considered the main reason for the enhancement.

The effect of AC square wave at different frequencies on the EHD enhancement is studied for both symmetric and unsymmetric wave forms. The symmetric wave form is a square wave with zero offset and with amplitude equals 12 kV as shown in Fig. 12a. The melting progress with time under EHD at different wave frequencies is shown in Fig. 12b. At 60 Hz frequency, the charges will not have enough time to relax as the frequency is higher than the critical frequency for charge relaxation ($f > 1/\tau_e$), where τ_e is the charge relaxation time, and hence the Coulomb force is suppressed. At this high frequency, there is no enhancement observed indicating that the dielectrophoretic force is minimal in this study. This is because the dielectrophoretic force depends on the square of the electric field (E^2) (refer to equation (1)) and hence it is not affected by the direction of the electric field. By reducing the frequency to 3 Hz, the enhancement still does not exist. At 2 Hz, melting under EHD starts to take place which reveals that the critical frequency is reached, and the Coulomb force becomes effective. The EHD enhancement becomes very significant when the frequency is reduced to 1 Hz. At this case, the effective thermal conductivity reached a maximum value of 1.2 with an enhancement of 6-fold.

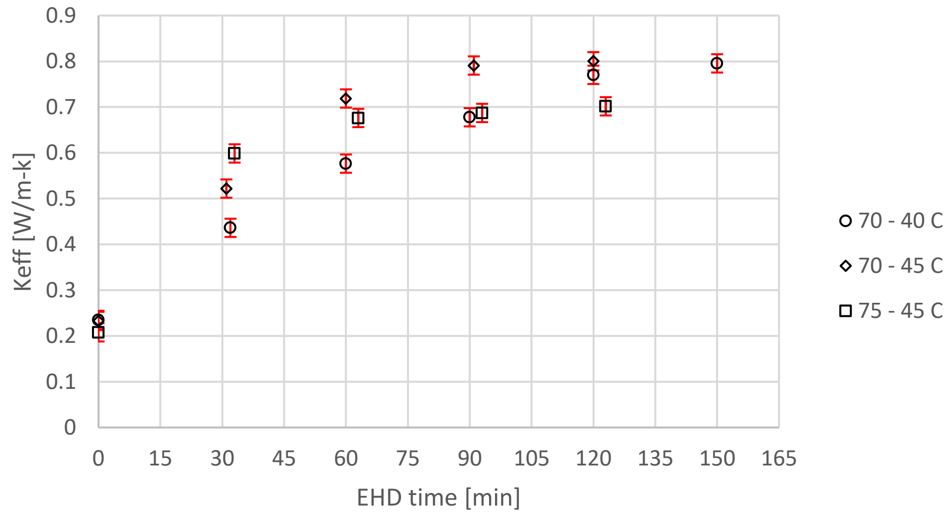

Fig. 11. EHD enhancement at different temperature boundaries at 6 kV applied voltage

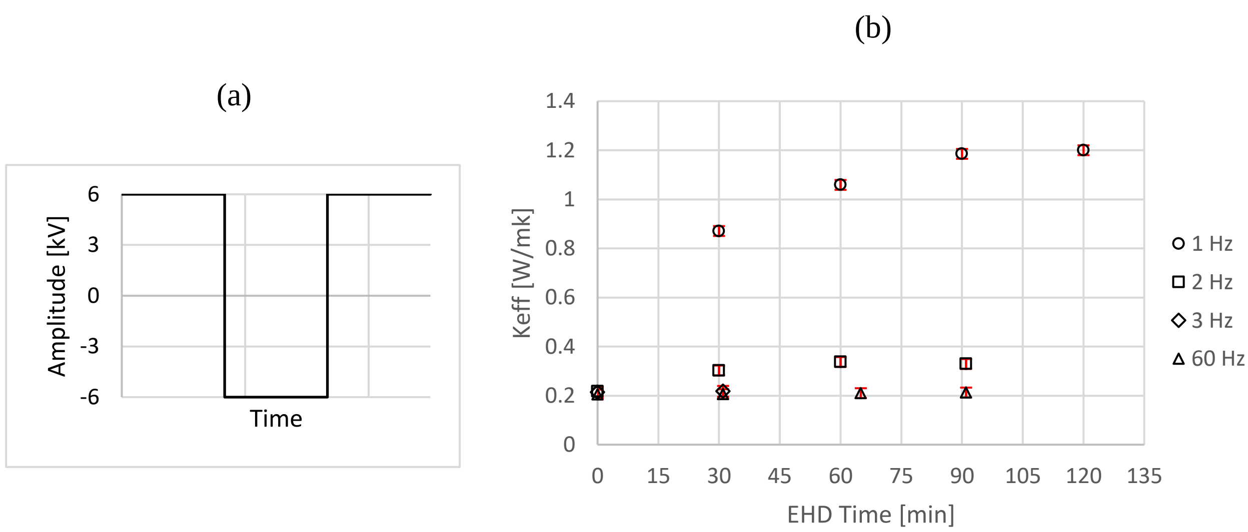

Fig. 12. (a) Symmetric square wave form, (b) EHD enhancement with time for AC square symmetric wave forms with different frequencies at 6 kV applied voltage

For the unsymmetric 6 kV amplitude square wave shown in Fig. 13, EHD enhancement is observed for all cases. For frequencies higher than the critical value (2 Hz), the enhancement indicates the existence of Coulomb force despite the effect of charge relaxation. This is because the charges are accumulating during the half cycles of non-zero amplitude as the Coulomb force is not reversing its action each half cycle; it has a positive effect in one cycle and zero on the other. This results in a buildup of charges over time giving rise to the Coulomb force. Variation of the AC wave frequency within values that are higher than the critical frequency does not have any effect on the melting enhancement. However, by reducing the frequency to 1 Hz, there is a small increase in the enhancement observed. The effective thermal conductivity for this case reaches 0.52 W/m-K at EHD steady state. This can be attributed to the frequency becoming lower than the critical frequency for charge relaxation; hence the charges will have enough time to accumulate, and the Coulomb force is intensified.

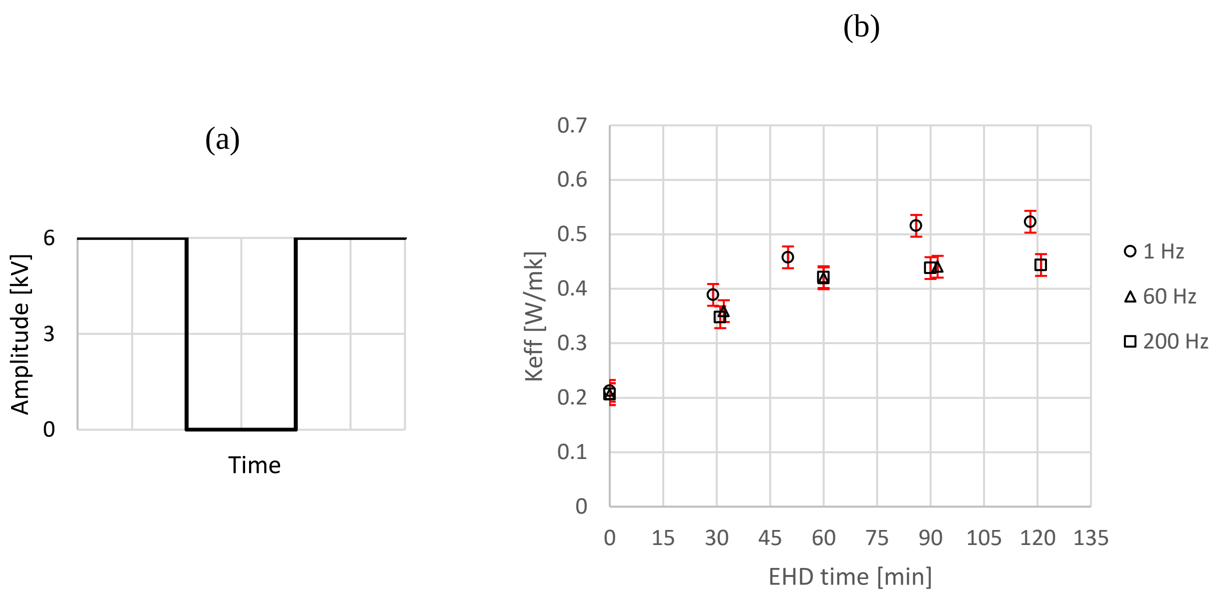

Fig. 13. (a) Unsymmetric square wave form, (b) EHD enhancement with time for AC square unsymmetric wave forms with different frequencies

Fig. 14 compares the EHD enhancement for the cases of DC and AC symmetric and unsymmetric wave forms. For the low frequency cases (1 Hz), the symmetric wave form shows higher enhancement than the unsymmetric one as the effect of the Coulomb force is existing only on one half cycle for the unsymmetric case while it is prevailing over the whole cycle period for the symmetric case. For the high frequency cases (60 Hz), the effect of the Coulomb force exists only in the unsymmetric waves due to the charge relaxation effect which suppresses this force for the symmetric waves at frequency higher than the reciprocal of charge relaxation time.

Also, the enhancement for the AC 1 Hz symmetric square wave was found to be higher than that for the DC case. The melt fraction for the AC case reached 78% with an effective thermal conductivity of 1.2, while the melt fraction for the DC case is 67% and k_{eff} = 0.7. Therefore, the melting enhancement for the AC 1 Hz symmetric wave can be considered the maximum enhancement reached for the 6 kV applied voltage in all cases. This is hypothesized to be due to that the electroconvection cells is reversing direction each half cycle of the AC symmetric wave, due to change in polarities, leading to an unstable flow regime which increases turbulence inside the liquid region and thus results in more melting.

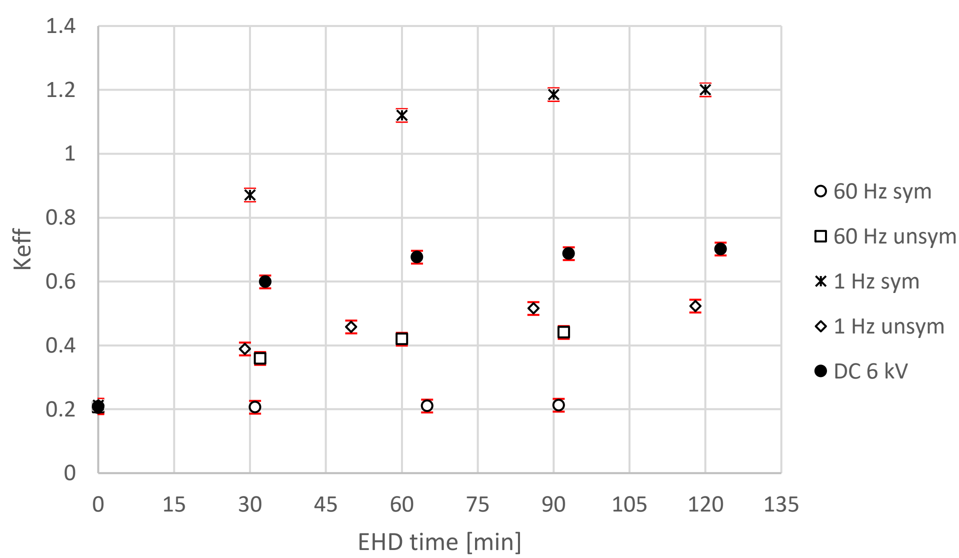

Fig. 14. EHD enhancement for DC and AC square symmetric and unsymmetric waves at 6 kV applied voltage and different frequencies.

2.3.4 Solid Extraction

Solid extraction is detected in all EHD experiments with DC applied voltage. Dendrites are observed to be pulled out from the mushy zone at the melt front under the action of the interfacial forces into the liquid bulk. In this study, the Coulomb force is the dominant force that acts on the dendrites at the interface.

After extraction, the suspended dendrites in the liquid medium will be influenced by two main factors. The first factor is the secondary motion created in the liquid in the form of convection cells which drives the dendrites' motion in the direction of rotation of the cells. The second factor is the dielectrophoretic force on a particle in an inhomogeneous electric field. This force tends to move the particles in the direction of the high electric field [29]. Under the action of these effects, the dendrites move upwards as shown in Fig. 15. The size of the dendrites decreases as they move into higher temperature regions until they are completely melted and disappear.

Fig. 16 shows the melt front locations with time starting from the non-EHD position to 25 minutes after EHD is applied at which time the melt front nearly reaches a steady state position. It can be observed that the melt front is not moving horizontally as it would for conduction dominated melting, and it takes the wavy shape form due to the generated EHD convection cells. The direction of motion of the dendrites after extraction is represented by the arrows. It is shown that the dendrites are moving towards the center in a rotational manner. This indicates that the main driving force acting on the suspended dendrites in the liquid region is the electroconvection cells.

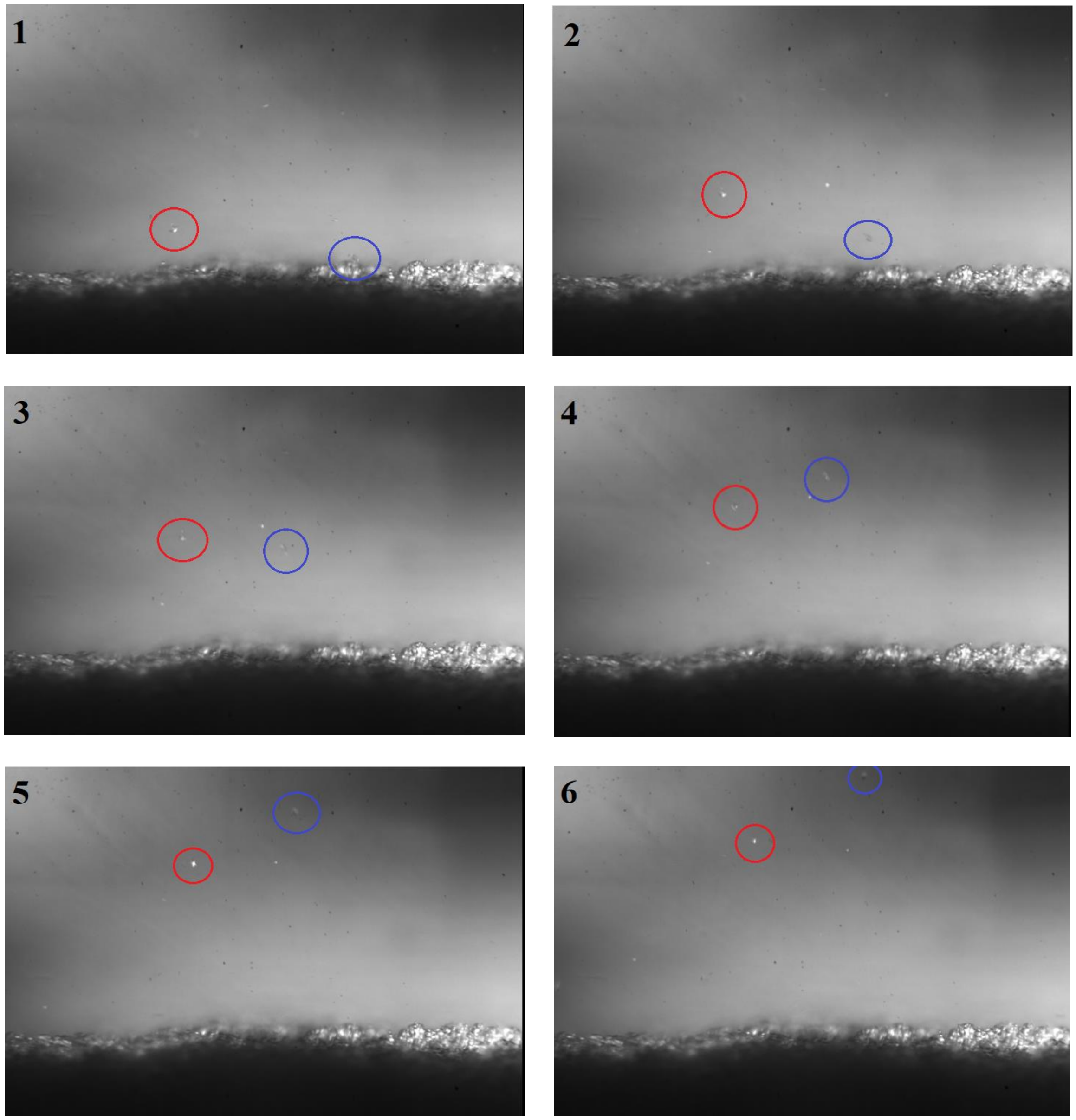

Fig. 15. Solid extraction behavior at 6 kV applied voltage – time between frames = 0.2 s.

The locations where dendrites are extracted are illustrated in Figs. 17 and 18. The high-speed camera is focused on the melt front at different periods. At the beginning of EHD, solid extraction is detected very intensively at location (a), and the extraction continues until EHD time equals 7 min. The extraction then becomes very low except for some regions close to the electrode where the dendrites tend to move away from it. Melting continues with low extraction intensity until steady state condition is reached after about 25 min from EHD. For location (b), the solid extraction is only observed at starting EHD and remains for about 2 min. As the melt front progresses downwards, the extraction almost disappears. Solid extraction is not observed when steady state is reached.

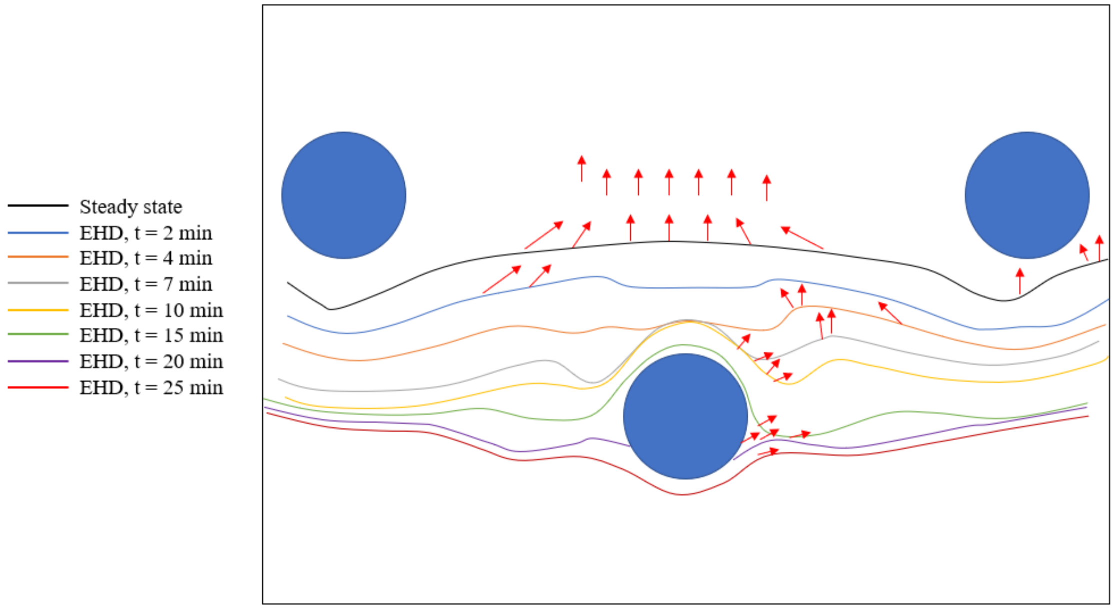

Fig. 16. Melt front positions with time showing the direction of solid extraction.

The main driving mechanism for solid extraction in this study is mainly the Coulomb force as the dielectrophoretic force was shown to be negligible in the AC square wave form experiments. The Coulomb force acts on the charged dendrites at the interface and forces them to move into the liquid bulk. When EHD is applied, the injection of free charges takes place from the high voltage electrodes due to the high generated electric field. The charge injection leads to the formation of charged layers in the vicinity of the electrodes that have similar polarity as that of the electrodes, and the charge density is declining away from the electrode area [30]. It is hypothesized that the accumulated charges at the interface of the mushy zone will move by the action of the attraction forces towards the opposite polarity electrodes or the ground sides (the top and bottom heat exchangers). This results in higher extraction intensity at start of EHD when the interface is below the upper row of electrodes. As the melt front progresses downwards, solid extraction is observed with lower intensity as the mushy zone is moving away from the upper ground surface and coming closer to the lower surface. This reverses the direction of the attraction forces acting on the dendrites at the interface, which will be directed downwards, and hence resulting in lower solid extraction. The absence of the solid extraction at position b is due to the electric field lines are directed downwards at this position as shown in Fig. 7.

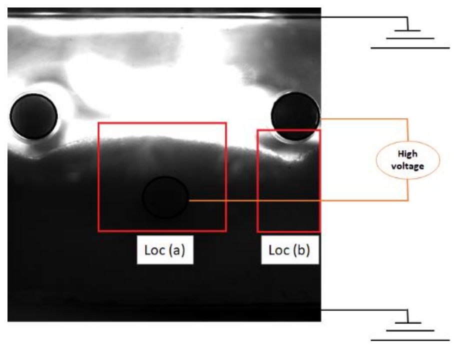

Fig. 17. Locations for solid extraction visualization

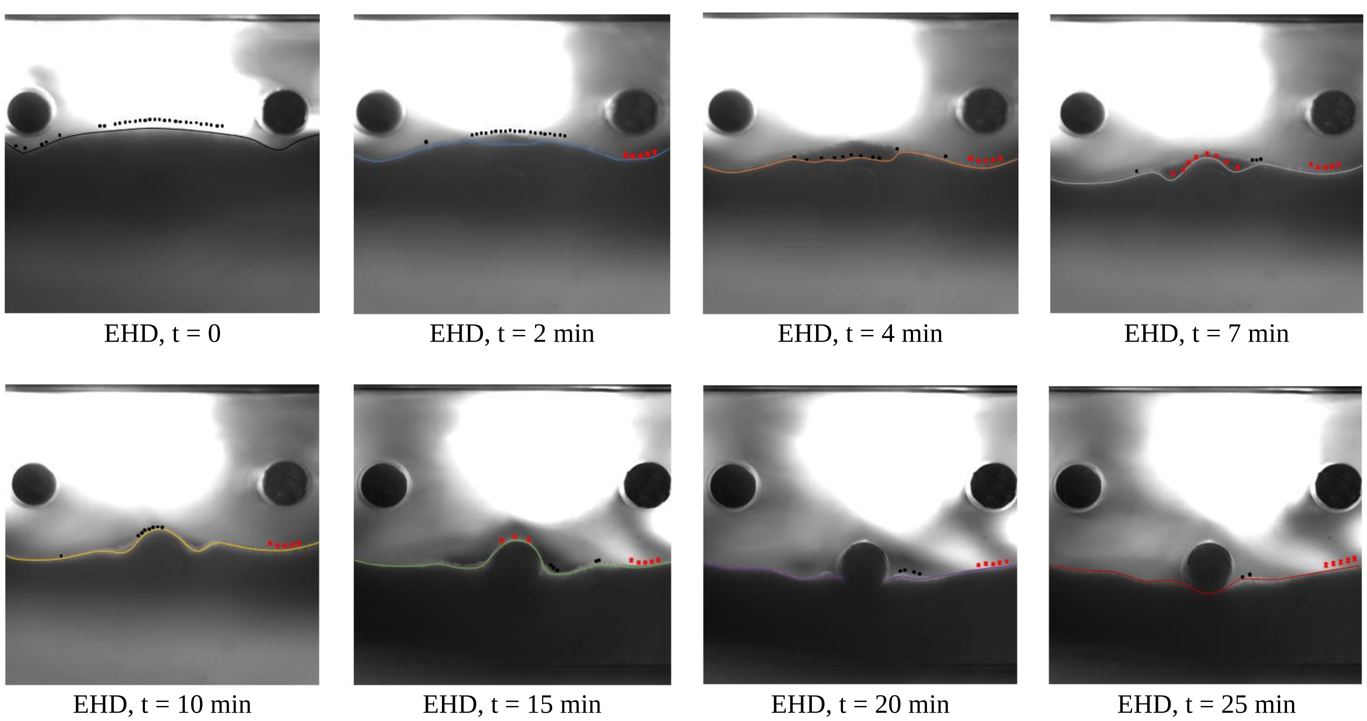

Fig. 18. Solid extraction locations with time under an applied voltage 6 kV – Black dots: extraction exists, red x: no extraction.

Solid extraction is examined for AC square symmetric wave form with frequency equals 1 Hz. The images for the dendrites are shown in Fig. 19. It is observed that the dendrites are moving up and down in an oscillatory motion. This is because the AC wave is reversing direction every half cycle which results in reversing the force acting on the dendrites due to the change in electric field direction. During the positive half cycle the charge injection is from the high voltage electrodes and are attracted to the upper ground surface, while during the other negative half cycle, the charge injection becomes from the ground side and attracted to the counter electrodes. Therefore, the motion of the charges is reversed each half cycle which leads to the conclusion that the main driving force for solid extraction is the Coulomb force.

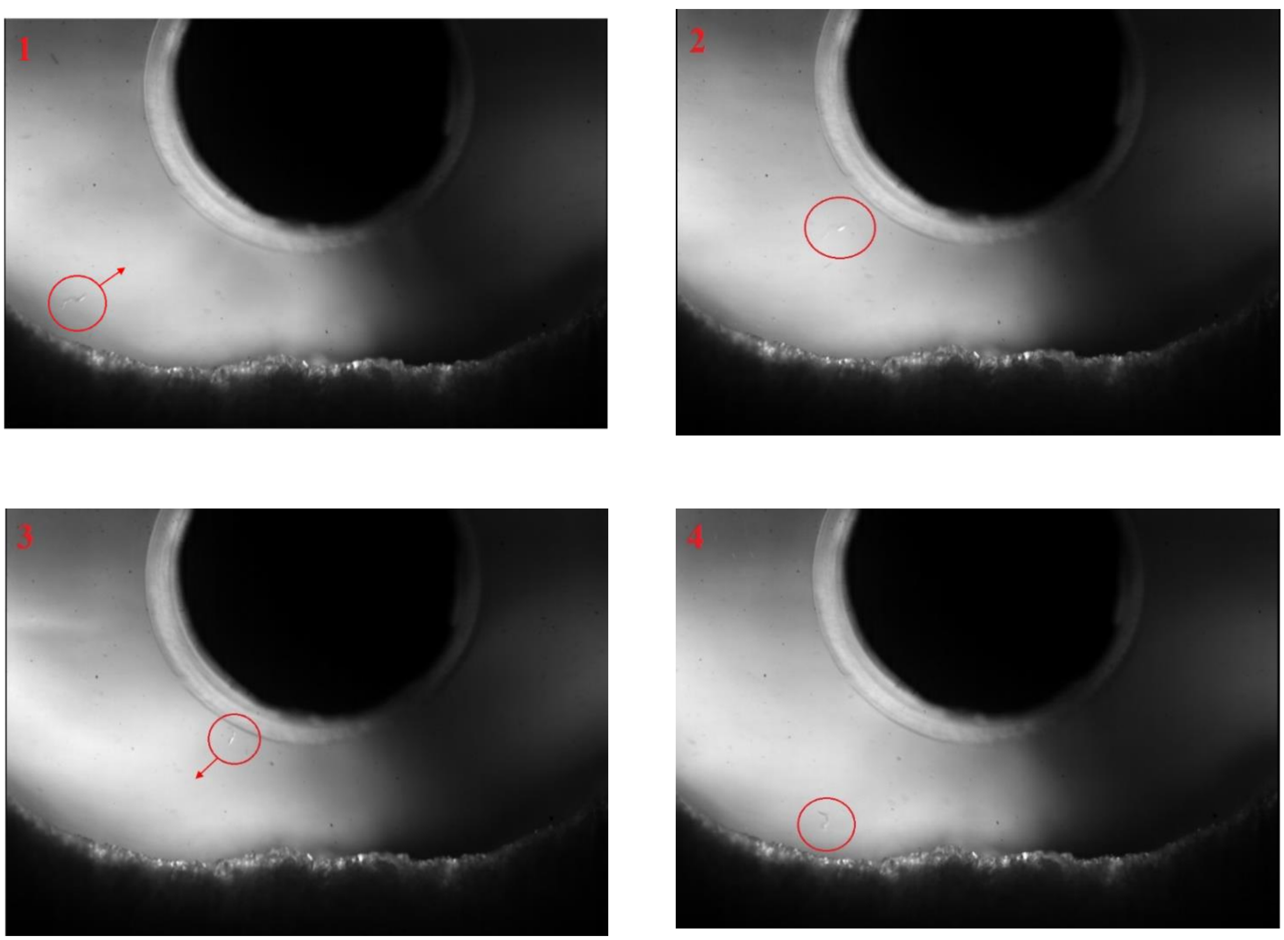

Fig. 19. Solid extraction for AC symmetric square wave – time between frames = 0.15 s.

2.4 Conclusions

In this study, the heat transfer enhancement using electrohydrodynamic (EHD) method was investigated during melting of paraffin wax under constant temperature boundary condition. Experiments under DC and AC applied voltages were conducted. The melt fraction of the PCM was determined for both the non-EHD and the EHD conditions. The EHD effective thermal conductivity was determined to represent the amount of heat transfer enhancement for each of the cases.

For the DC experiments, the effects of different applied voltages, polarities, and temperature boundaries were studied. It was found that the melting enhancement is increasing with voltages, and the maximum effective thermal conductivity was 0.95 at -10 kV applied voltage with an increase in thermal conductivity of 4.8-fold. The study of the effect of polarities showed that the negative polarity showed a little higher enhancement than the positive polarity at voltages higher than 6 kV. The effect of temperature boundary on the EHD melting enhancement was observed to be small. The case of higher temperature gradient has a lower enhancement due to the influence of the buoyancy force acting on the bulk liquid to reduce electroconvection.

The AC experimental results showed that the effect of the dielectrophoretic force is negligible in this study. The critical frequency for charge relaxation was found to be 2 Hz, and by reducing the frequency below this value the Coulomb force becomes effective. The effect at 1 Hz frequency case led to higher enhancement compared to the DC case hypothesized to be due to the flow instabilities. Also, it was found that the Coulomb force is still effective when applying high frequency AC unsymmetric wave forms, and that the enhancement results is not depending on the wave frequency for these conditions. The two later findings require additional investigating to fully understand the effect of duty cycle and the potential of controllable flow instabilities.

The solid extraction visualization using high-speed imaging showed that the extraction was detected for all the applied voltages. The dendrites were pulled out from the mushy zone at the melt front into the liquid bulk under the action of Coulomb force. After extraction, the dendrites are moving in the liquid volume under the effect of the electroconvection cells.

Declaration of Competing Interest

The authors declare that they have no known competing financial interests or personal relationships that could have appeared to influence the work reported in this paper.

CRediT authorship contribution statement

Ahmed Hassan: Conceptualization, Methodology, Software, Validation, Investigation, Data curation, Formal analysis, Writing - original draft. **James S. Cotton:** Supervision, Funding acquisition, Writing - review & editing.

Acknowledgements

This project was partly supported by the Natural Sciences and Engineering Research Council of Canada (RGPIN/355844). We would like to acknowledge CMC Microsystems for the provision of COMSOL that facilitated this research.

2.5 Appendix A: Differential Scanning Calorimetry (DSC) results

A DSC test was conducted inside McMaster University using TA instruments DSC 2910 machine to accurately obtain the melting temperatures for the paraffin wax used in experiments. The DSC system applies a constant heat flow into a sample and reference pan while measuring the temperatures and the associated heat flow, with an accuracy ±1 %, during the transition in materials as a function of time. A DSC test with a reference sample (Indium) is conducted first to determine the calibration cell coefficient for the experiments, then a sample of 9.8 mg Paraffin wax is tested. During the test, a heat flow of 10 °C/min is applied to the DSC cell while purging the cell with Nitrogen gas at a flow rate of 20 mL/min. The result of the heat flow as a function of temperature is shown in Fig. A.1. The results show that the higher and lower melting temperatures are 53 °C and 62.7 °C respectively.

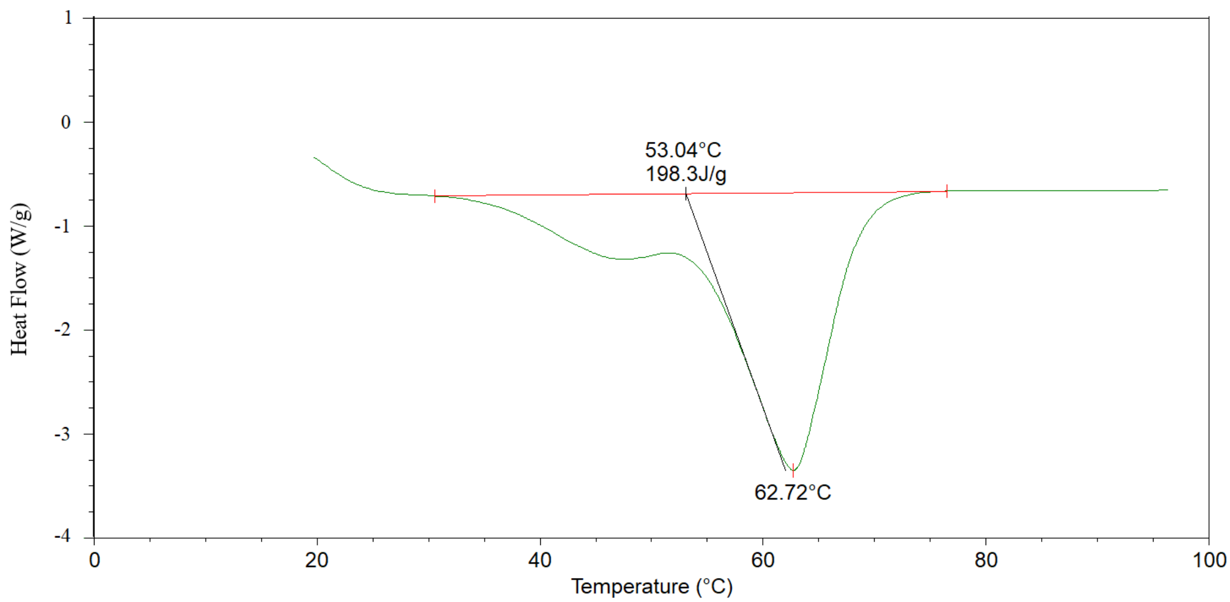

Fig. A.1. DSC test result

2.6 References

[1] Iten, Muriel, Shuli Liu, and Ashish Shukla. "A review on the air-PCM-TES application for free cooling and heating in the buildings." Renewable and Sustainable Energy Reviews 61 (2016): 175-186.

[2] Zalba, Belen, et al. "Review on thermal energy storage with phase change: materials, heat transfer analysis and applications." Applied thermal engineering 23.3 (2003): 251-283.

[3] Ibrahim, Nasiru I., et al. "Heat transfer enhancement of phase change materials for thermal energy storage applications: A critical review." Renewable and Sustainable Energy Reviews 74 (2017): 26-50.

[4] Lin, Yaxue, et al. "Review on thermal conductivity enhancement, thermal properties and applications of phase change materials in thermal energy storage." Renewable and sustainable energy reviews 82 (2018): 2730-2742.

[5] Al-Maghalseh, Maher, and Khamid Mahkamov. "Methods of heat transfer intensification in PCM thermal storage systems." Renewable and Sustainable Energy Reviews 92 (2018): 62-94.

[6] Alam, Tabish, and Man-Hoe Kim. "A comprehensive review on single phase heat transfer enhancement techniques in heat exchanger applications." Renewable and Sustainable Energy Reviews 81 (2018): 813-839.

[7] Chu, Boa-Teh. "Thermodynamics of electrically conducting fluids." The Physics of Fluids 2.5 (1959): 473-484.

[8] Nishikawara, Masahito, Hideki Yanada, and Kota Shomura. "Synergy between injection and dissociation mechanisms in electrohydrodynamic pumps modeled numerically." Journal of Electrostatics 93 (2018): 137-145.

[9] Fernandes, Dolfred Vijay, et al. "Numerical simulation of the electro-convective onset and complex flows of dielectric liquid in an annulus." Journal of mechanical science and technology 26.12 (2012): 3785-3793.

[10] Yoshikawa, Harunori N., Olivier Crumeyrolle, and Innocent Mutabazi. "Dielectrophoretic force-driven thermal convection in annular geometry." Physics of Fluids 25.2 (2013): 024106.

[11] Takashima, Masaki, and Hiromitsu Hamabata. "The stability of natural convection in a vertical layer of dielectric fluid in the presence of a horizontal ac electric field." Journal of the Physical Society of Japan 53.5 (1984): 1728-1736.

[12] Sadek, H., C. Y. Ching, and J. Cotton. "The effect of pulsed electric fields on horizontal tube side convective condensation." International journal of heat and mass transfer 53.19-20 (2010): 3721-3732.

[13] Omidvarborna, H., et al. "Effect of applied EHD on in-tube condensation of R-134a within an assembled experimental rig including a laboratory heat exchanger." Experimental Thermal and Fluid Science 58 (2014): 112-120.

[14] Sadek, H., et al. "Electrohydrodynamic enhancement of in-tube convective condensation heat transfer." International Journal of Heat and Mass Transfer 49.9-10 (2006): 1647-1657.

[15] Laohalertdecha, Suriyan, and Somchai Wongwises. "Effects of EHD on heat transfer enhancement and pressure drop during two-phase condensation of pure R-134a at high mass flux in a horizontal micro-fin tube." Experimental thermal and fluid science 30.7 (2006): 675-686.

[16] Nangle-Smith, S., H. Sadek, and J. S. Cotton. "The influence of the electrophoretic and polarization forces on two phase flow redistribution in a horizontal annular tube." Int. J. Plasma Environ. Sci. Technol. 7.1 (2013): 64-70.

[17] Nakhla, David, Hossam Sadek, and James S. Cotton. "Melting performance enhancement in latent heat storage module using solid extraction electrohydrodynamics (EHD)." International Journal of Heat and Mass Transfer 81 (2015): 695-704.

[18] Nakhla, D., et al. "Measurement of heat transfer enhancement in melting of n-Octadecane under gravitational and electrohydrodynamics (EHD) forces." Journal of Electrostatics92 (2018): 31-37.

[19] Nakhla, David, and James S. Cotton. "Effect of electrohydrodynamic (EHD) forces on charging of a vertical latent heat thermal storage module filled with octadecane." International Journal of Heat and Mass Transfer 167 (2021): 120828.

[20] Selvakumar, R. Deepak, and S. Vengadesan. "Combined effects of buoyancy and electric forces on non-isothermal melting of a dielectric phase change material." International Journal of Multiphase Flow 151 (2022): 104029.

[21] Sun, Zhihao, et al. "Experimental investigation on the melting characteristics of n-octadecane with electric field inside macrocapsule." International Journal of Heat and Mass Transfer 173 (2021): 121238.

[22] Sun, Zhihao, et al. "Experimental investigation on melting heat transfer of an organic material under electric field." Experimental Thermal and Fluid Science 131 (2022): 110530.

[23] Thompson, Eric. Electrohydrodynamic Solidification of Phase Change Materials. Diss. 2017.

[24] Tabassum, Tonny, Mainul Hasan, and Latifa Begum. "Transient melting of an impure paraffin wax in a double-pipe heat exchanger: Effect of forced convective flow of the heat transfer fluid." Solar Energy 159 (2018): 197-211.

[25] Dellorusso, Paul Robert. Electrohydrodynamic heat transfer enhancement for a latent heat storage heat exchanger. DalTech-Dalhousie University, 1999.

[26] Sharma, R. K., P. Ganesan, and V. V. Tyagi. "Long-term thermal and chemical reliability study of different organic phase change materials for thermal energy storage applications." *Journal of Thermal Analysis and Calorimetry* 124.3 (2016): 1357-1366.

[27] Shukla, Anant, D. Buddhi, and R. L. Sawhney. "Thermal cycling test of few selected inorganic and organic phase change materials." *Renewable energy* 33.12 (2008): 2606-2614.

[28] McPherson, Joe W., et al. "Trends in the ultimate breakdown strength of high dielectric-constant materials." *IEEE transactions on electron devices* 50.8 (2003): 1771-1778.

[29] Pethig, Ronald, et al. "Dielectrophoresis: a review of applications for stem cell research." Journal of Biomedicine and Biotechnology 2010 (2010).

[30] Stishkov, Yury, and Vladimir Chirkov. "Dependence of the electrohydrodynamic flows structure in very non-uniform electric field on the charge formation mechanism." 2011 IEEE International Conference on Dielectric Liquids. IEEE, 2011.

Chapter 3: Investigation of the role of charge injection and Coulomb force during the melting of phase-change materials under constant temperature boundary conditions

Investigation of the role of charge injection and Coulomb force during the melting of phase-change materials under constant temperature boundary conditions

Ahmed Hassan, James S. Cotton*,

McMaster University, Department of Mechanical Engineering, Hamilton, Ontario, Canada

*Corresponding Author: cottonjs@mcmaster.ca

ABSTRACT

This paper presents an investigation of the melting of dielectric material in a rectangular cavity under the effect of electrohydrodynamics (EHD). First, phase-change modeling is implemented to simulate the melting performance of paraffin wax without EHD under constant temperature boundary conditions until a steady-state condition is achieved. Next, the whole set of coupled EHD equations is introduced to the model, with the Coulomb force using a Heaviside function for charge injection being the only electrical body force considered. Finally, the numerical model is implemented using the finite element method to solve for the electric field, flow field, temperature field, and charge transport.

The numerical results show that, under the effect of EHD, melting continues due to the generation of electroconvection cells in the liquid phase change material (PCM) and the flow field manifests as two symmetric rotational cells generated between every two successive electrodes. The flow field causes the redistribution of the temperature field in the liquid bulk, which enhances the heat transfer. Melting continues until a steady-state condition is reestablished after about one hour. The enhancement factor, defined as the ratio of the EHD melt thickness to the steady-state melt thickness without EHD, is 2.33 at 6 kV applied voltage.

3.1 Introduction

The augmentation of heat transfer is a major problem that has recently attracted the attention of many researchers. In an attempt to solve this problem, researchers have employed various techniques to increase heat transfer in different thermal systems, including heat exchangers, thermal energy storage systems, power electronics, and the space industry. In thermal energy storage systems, heat transfer is affected by the poor thermal conductivities of the phase-change materials (PCMs) used in such systems. The enhancement techniques used in these systems can be classified into two categories: passive and active. Passive techniques do not use external power and usually require an increase to the thermal conductivity of the material, the modification of the heat-transfer surface, or the use of multiple PCMs with different melting temperatures to maintain a nearly constant temperature difference between the fluid and the PCM [1], [2]. The thermal conductivity of the PCM can be increased by using highly-conductive additives or porous materials, such as carbon nanoparticles and graphene, while the modification of the heat-transfer surface requires the use of extended surfaces or modifying surface geometry [2]–[4]. In contrast, active techniques involve the input of external power to the system to increase heat transfer, which enables more active control of heat transfer compared to passive methods. Active methods are classified based on the type of power supply that is used, for example, mechanical aids, surface vibration, electrohydrodynamics, and magnetohydrodynamics.

In electrohydrodynamics (EHD), a high voltage at very low current levels is applied to the system which creates an electric field within the dielectric medium, this generates secondary motion in the fluid. The secondary flows are produced by electrical body forces and interfacial forces, which can be expressed by Equation (1) [5],

$$\bar{f}_{EHD} = q\bar{E} - \frac{1}{2}E^2\nabla\varepsilon + \frac{1}{2}\nabla[\rho E^2 \left(\frac{\partial\varepsilon}{\partial\rho}\right)_T] \quad (1)$$

where, f_{EHD} represents the EHD forces acting per unit volume on the fluid. The terms on the right-hand side of Equation (1) represent three EHD forces. The first term is the electrophoretic or Coulomb force, which is produced by the space-charge density acting on the electric field lines. This force is considered the main contributor to heat-transfer enhancement in single-phase systems. The second term represents the dielectrophoretic force. This force requires a gradient in the dielectric constant of the medium, which can occur at the interface of two-phase systems. The third term represents the electrostrictive force and is a function of changes in the fluid's permittivity in relation to density. The second and third forces are known as polarization forces, and they become significant in two-phase systems or when using extremely high temperature gradients. For the Coulomb force to be effective, free charges must exist in the fluid volume. There are two main charge-creation methods: injection, wherein charges are formed via chemical reactions created on the surface of the electrodes; and conduction, wherein charges are created via the dissociation of molecules in the bulk of the fluid due to strong electric field gradient. Prior findings have shown that injection becomes dominant when a very high electric field is applied to liquids with very low conductivity [6].

The EHD flow generated in the liquid bulk due to the electrical body forces impacts heat-transfer and melting performance in solid-liquid dielectric systems. Specifically, the electroconvection flow disturbs the thermal boundary layer, thereby increasing the heat-transfer coefficient, and thus, the melting performance of solid-liquid dielectric systems and transports the hot fluid in the thermal boundary in proximity of the solid liquid melt front. The enhancement of electrohydrodynamic heat transfer in two-phase solid-liquid systems has been experimentally investigated in several studies, with findings indicating that, while EHD can enhance heat transfer in melting processes, it has a limited effect for solidification [7]. Nakhla et al. [8] studied the thermal behavior of paraffin wax in conduction-dominated melting experiments under constant heat flux boundary conditions. To this end, they applied high voltage via two horizontal rows of electrodes with the top heated surface being grounded. Their findings revealed that the melting time decreased by about 40% under the influence of EHD at -8 kV. In a subsequent study, Nakhla et al. [9] investigated how EHD impacts the melting performance of n-octadecane under constant temperature boundary conditions. Here, they observed that the application of +10 kV enabled an up to 8.6-fold increase in heat transfer. Elsewhere, Sun et al. [10] investigated the EHD heat-transfer enhancement of a phase-change material contained in a small cavity. In this work, the authors maintained the left and right sides of the cavity at high and low temperatures, respectively. When high voltage was applied at the hot electrode, the melt fraction decreased as the voltage increased. For instance, the application of 20 kV resulted in a 30% decrease in the melt fraction compared to the non-EHD case. The application of PIV measurements to detect the velocity distribution of the EHD flow revealed that the liquid is attracted to the hot plate, thus resisting the natural convection. Conversely, the application of high voltage at the cold plate enhanced melting when the voltage exceeded 15 kV: at +20 kV, the liquid fraction increased by about 43%, with a maximum detected velocity of about 7.5 mm/s. In other work, Nakhla et al. [11] examined the interaction between electrical and gravitational effects during the melting of octadecane in a vertically oriented enclosure. Shadowgraph images were employed to determine the local heat-transfer coefficient at the hot wall. The results suggested the existence of two unsymmetric bifurcation cells between the electrodes at low voltages, which became more symmetric with increasing voltage, thus indicating the transition to an electrically dominated melting regime. Sun et al. [12] further studied the melting of n-octadecane inside a cylindrical cavity under EHD conditions. At 5 kV applied voltage, the detected velocity field was very small resulting in a slight heat transfer enhancement, however, increasing the voltage to 15 kV enhanced melting with the application of EHD. Furthermore, it was found that negative polarity voltage resulted in higher melting enhancement compared to positive polarity voltage. In a different study, Hassan et al. [13] explored how the application of EHD and different DC voltages impacted melting, finding that heat transfer increased alongside the voltage. The authors found that the maximum average effective thermal conductivity reached at the maximum applied voltage of 10 kV was 0.95 W/m-K, with a 4.8-fold enhancement ratio.

Since the Coulomb force is considered the main driving mechanism for EHD flow in both single-phase and two-phase systems, many numerical studies have been conducted to examine the charge injection process in different EHD systems. There are two main models of charge injection: autonomous injection and nonautonomous injection. In autonomous injection, the space-charge density is assumed to be constant at the injector electrode [6], [14], while in nonautonomous injection, the charges are formed at the interface of the electrode and the liquid where the injected charge is functionally dependent on the local electric field [15], [16].

In single-phase autonomous injection modeling, the electroconvection flow characteristics are studied using various electric Rayleigh numbers, T, which represents the intensity of the Coulomb force for different electrode configurations [17]–[20]. Lu et al. [21] examined the flow structure and heat transfer with the application of EHD to a dielectric material contained between two parallel plates. The lower plate was maintained at a higher temperature while assuming a unipolar injection originating at its boundaries. At higher Ra numbers, the heat transfer was found to be independent on T parameter due to the dominance of the buoyancy force.

Additionally, the flow patterns and consequently the heat transfer were significantly influenced by variations in the mobility parameter. Li et al. [18] studied the electroconvection of dielectric liquid in a square cavity using the Lattice Boltzmann method and assuming unipolar autonomous injection. Li et al. [14] were able to characterize the behavior of the EHD flow transition from a steady state to highly transient by increasing the electric Rayleigh number, T, at different Rayleigh numbers. In another study, Huang et al. [22] employed the finite volume method to investigate the different EHD flow-characteristic states of a dielectric liquid between concentric cylinders at different mobility parameters. The authors applied different electric potentials to the inner and outer cylinders, while a randomly selected constant space-charge density was applied at the injection electrode. The transition of the electroconvection flow from a steady state to a highly mixed flow was observed by increasing the electric Rayleigh number, with findings indicating that the electroconvection cells bifurcated directly a fully mixed flow at higher mobility parameters. Moreover, Su et al. [23] showed that the fluid elasticity is greatly affecting the flow patterns and the bifurcation conditions while numerically studying unipolar injection for a viscoelastic fluid.

Furthermore, the effect of electric field on the electroconvection within a horizontal oriented layer of a liquid with low conductivity heated from above was investigated for both DC [24] and AC [25] fields. In these studies, space charges are generated due to injection of negative charges at the cathode, it was found that the fluid exhibits oscillatory instability due to the influence of the Coulomb force concurrent with the presence of a convective restoring force that is acting on the opposite direction due to the effect of density variation. Two convective vortices exist within each cell, undergoing periodic changes in rotation direction. Simultaneously, the stream function at a specific point within the cell undergoes periodic reversals in its sign. In addition, the author investigated the linear stability of electroconvection, where the change in the electric parameter T, can result in a regime of standing or traveling waves as a result of direct Hopf bifurcation. Taraut et al. [26] investigated the case of injection from the anode with dissociation of impurities in the medium. Fluid flow with oscillatory perturbation is created due to the generated Coulomb force, from injection and dissociation processes, and the resisting buoyancy force. During the flow evolution, standing waves are formed at the initial stages with two convection rolls created. With time, the waves become unstable, and the flow transitioned to the traveling wave regime.

The effect of the electric driving parameter, T, in two-phase autonomous injection systems has also been investigated at different melting conditions and under different flow configurations. For instance, Luo et al. [27] developed a Lattice Boltzmann method (LBM) to investigate the EHD-enhanced melting of a phase-change material in a 2D square cavity at different applied voltages. Constant temperature and electric potential were applied to the top and bottom surfaces, while the other walls were insulated. A uniform charge injection was assumed at the higher voltage electrode. Initially, melting was observed to be conduction dominated; however, two pairs of vortices were subsequently created in the liquid, which eventually became one pair as EHD melting progressed. Finally, the flow pattern became unstable once the system had completely melted, as the electric Rayleigh number exceeded the critical value for the single-phase case. In addition, Luo et al. [27] found that the melting time could be reduced by increasing the electric potential, as increasing the electric Rayleigh number to 1800 reduced melting-time by up to 33%. Elsewhere, Lu et al. [28] numerically investigated the melting behavior of a dielectric material in a 2D cavity under the combined effect of buoyancy and EHD forces. To this end, the LBM method was used to simulate the velocity field, electric field, and temperature field during EHD melting at different Rayleigh numbers and electric Rayleigh numbers for two cases: melting from the bottom surface and melting from the left wall. Constant space-charge density boundary conditions were applied for the injecting electrodes. The findings revealed that the melting performance was nearly the same for the different applied parameters during the initial melting stages. At high electric Rayleigh numbers, the bifurcation of convection cells enhanced the melting rate, and melting occurred more rapidly in the case of melting from below compared to melting from the left wall. However, the time savings accrued from melting on the left wall were always higher compared to melting from below, with maximum time savings of 63% at the highest electric Rayleigh number (T = 2000). In a later study, Lu et al. [29] investigated the EHD melting of a pure dielectric between two concentric annuli using the LBM method. The number and symmetricity of the generated convection cells was found to be influenced by the melting boundary. Selvakumar et al. [30] employed the finite volume method to numerically study the combined effects of gravitational and EHD forces on solid-liquid phase-change behavior inside a rectangular cavity under the influence of an electric field and assuming homogenous and autonomous injection. When melting was conducted from the bottom surface, the melting regime was initially conduction-dominated, but gradually converted to a convection-dominated regime. When the Coulomb force overcomes the viscous force, electroconvection flow cells are generated in the liquid region, where four charge void regions can be observed. Ultimately, a maximum melting enhancement of 56% was obtained at the highest electric Rayleigh number. In other work, Endigeri et al. [31] assessed the melting performance of a vertically heated square cavity under the effect of EHD flow. Here, a circular electrode at the center of the cavity was maintained at a constant electric potential boundary condition while simultaneously grounding all the cavity walls. Endigeri's et al. [31] findings revealed that melting enhancement increases alongside the electric potential at different Rayleigh numbers for the low electrode radius. Furthermore, the damping resistance of the flow increases alongside the electrode size, which reduces the melting rates. Interestingly, He et al. [32] studied melting under microgravity conditions in a shell and tube system. The LBM method was numerically implemented to model the phase-change of organic PCM due to EHD, with results indicating that the melting rate at no gravity without EHD was lower than that the melting rate under EHD or in the presence of gravitational force. Furthermore, increasing the electric Rayleigh number, T, from 0 to 1500 resulted in a 67% reduction in melting time in the no-gravity condition, while altering the gravity was found to influence EHD melting at small electric Rayleigh numbers, T, while having a negligible effect at higher values of T. The maximum melting enhancement obtained was 96% at 0.5 g gravity condition.

The nonautonomous injection model has been used in several recent numerical studies on single-phase liquid systems [15], [16], [33]–[35]. In these works, the charge injection at the electrode surface was defined as a function of the local electric field, depending on the actual current voltage characteristics of the studied EHD system. The space-charge density and the EHD flow structure of a dielectric liquid were numerically studied using the finite element method in a needle-plane electrode configuration [15], [33]. Specifically, high voltage was applied to the needle electrode surface while grounding the horizontal plane, with the injection current at the electrode being determined using the exponential function dependence equation or the Fowler-Nordheim equation. Additionally, the evolution of the charged jet in the axial and radial directions was resolved, and the characteristics of the space-charge distribution and the velocity field were compared for different methods of charge formation. Chirkov et al. [16] investigated the current-time characteristics during the application of EHD in a needle-plane electrode design for both the injection and dissociation models. For the injection model, an exponential function dependence was used for the current density boundary condition at the needle electrode. The authors discovered that the current-time characteristics were dependent on the charge-creation mechanism, and that the typical time required for the charge jet to reach the ground electrode was 0.1 s and the time interval for charge accumulation was 10 s. After this time, the total current becomes constant. Furthermore, the findings also revealed that the current increases in response to increasing the applied voltage. In other work, Gazaryan et al. [35] developed a method for determining the functional dependence of the charge injection function on the local electric field. They applied a charge injection model in a blade plane electrode design, with the introduction of different injection Heaviside functions as a boundary condition at the electrode surface. The authors determined the total electric current based on the integral solution of the current density, and the current-voltage relations obtained from the simulation were then compared to the experimental current voltage characteristics to obtain a good match between the results.

Previous studies have shown that the electrohydrodynamic technique can enhance the melting rates of phase-change materials in different solid-liquid systems. Both experimental and numerical studies have shown that heat-transfer enhancement depends on interactions between the thermal, electrical, and flow fields. In addition, several numerical studies have shown that the characteristics of EHD flow generated in the liquid bulk are affected by different control parameters such as the electric Rayleigh number, mobility, and the thermal Rayleigh number. Furthermore, previous numerical studies for two-phase EHD problems have employed charge-injection modeling using only the autonomous injection assumption, namely, that there is constant charge injection at the electrode, but this assumption does not represent the actual injection current density for non-uniform electric field like those present in studies with cylindrical electrodes or non-uniform melt fractions. Rather, the amount of charge injection depends on the local electric field at the electrode surface. Therefore, the assumption of an autonomous injection boundary condition is not accurate and does not reflect the actual charged ions injected from the electrodes, as the electric field is distributed around the injection electrode in a non-uniform manner. Therefore, electrohydrodynamic charge injection will be numerically modelled in this work using the nonautonomous injection.

The objective of the current study is to model the EHD problem for a two-phase solid-liquid system. The resultant numerical model will then be applied to simulate the phase change of paraffin wax under the effect of electroconvection generated due to the EHD Coulomb force using the finite element method. The observed interactions between the electric field, velocity field, and temperature field will be presented following this analysis. In the present work, charge injection is considered the only source for charge creation in the dielectric medium. The remainder of this paper is organized as follows. The physical problem, governing equations, and boundary conditions are detailed in Section II, and the numerical methods are briefly described in Section III. Next, the results are presented and discussed in Section IV, while Section V provides some concluding remarks.

3.2 Problem Formulation

3.2.1 Physical problem and governing equations

The physical problem considered in this study is similar to that addressed by the experimental two-phase latent heat system presented in our previous work [13]. As shown in Fig. 20, the system under consideration consists of a 2D rectangular cavity containing two rows of cylindrical electrodes evenly distributed in a staggered configuration. The horizontal distance between the electrodes is 9 mm, and the vertical spacing between the two rows is 6 mm. The electrode material is defined for copper (k = 400 W/m-K and Cp = 385 J/kg-K), and the rest of the domain is assigned the fluid properties of paraffin wax (Table 5). The electric permittivity of the paraffin wax is assumed to be homogenous for the whole domain, while the change in permittivity between the solid and liquid phases is neglected due to its low gradient at the interface which did not change the results of the simulations. An overestimated value for the diffusion coefficient is chosen ($D = 10^{-7}$ m^2/s) to accelerate the convergence of the model and increase the numerical stability. However, this exaggerated value has a limited effect on the results, as the diffusion current contributes relatively little compared to the migration and convection current components.

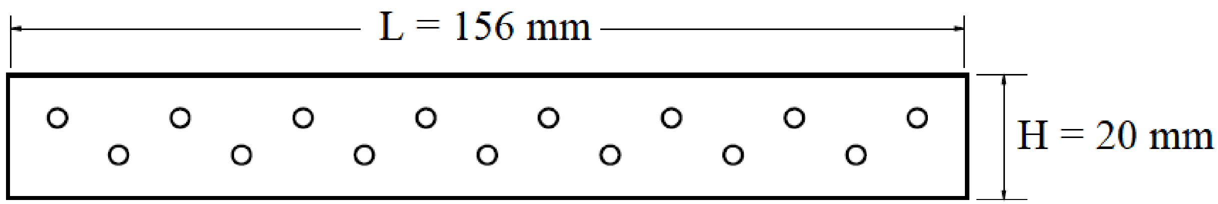

Figure 20: Numerical domain geometry.

The set of equations governing the EHD system include: the Poisson equation for the electric field; the Nernst Plank equation for charge transport; the Navier-Stokes equations; and the energy equation. In the mathematical model, the dissociation in the bulk of the fluid is neglected where the only source of charges in the medium is by charge injection from the electrodes. Also, the body forces considered in the momentum equation that govern the flow are the EHD Coulomb force and the gravitational force. Additionally, in the energy equation, the joule heating effect is neglected due to the very low current associated with the EHD problem. The electric power at the maximum studied voltage (6 kV) is about 0.6 mW which is less than 0.1 % of the applied heat flux. The complete formulation of the governing equations can be expressed as follows:

$$\vec{E} = -\nabla\varphi \tag{2}$$

$$\nabla.(\varepsilon_o \varepsilon_r \vec{E}) = q \tag{3}$$

$$\frac{\partial n_i}{\partial t} + \nabla.[n_i b_i \vec{E} + n_i \vec{U} - D_i \nabla n_i] = 0 \tag{4}$$

$$\mathrm{q} = e(n_1 - n_2) \tag{5}$$

$$\nabla.\vec{U} = 0 \tag{6}$$

$$\rho \frac{\partial \vec{U}}{\partial t} + \rho\left(\vec{U}.\nabla\vec{U}\right) = -\nabla P + \mu\nabla^2\vec{U} + \mathrm{q}\vec{E} - \rho g \tag{7}$$

$$\frac{\partial T}{\partial t} + \nabla.(\vec{U}\frac{\mathrm{H}}{C_p}) = \nabla.(\alpha\nabla\mathrm{T}) \tag{8}$$

In the above equations, φ is the electric potential, *E* is the electric field, *q* is the space-charge density, n_i is the ion concentration for the positive and negative species, *U* is the fluid velocity, *P* is the dynamic pressure, *H* is the total enthalpy, and *T* is the temperature. The symbols, ε, b, *D*, μ, ρ, and α, represent the properties of electrical permittivity, ionic mobility, the diffusion coefficient, dynamic viscosity, mass density, and thermal diffusivity, respectively. Equation (4) contains three different types of charge transport: charge migration due to the electric field, convection due to the flow field, and diffusion transport. The space-charge density can be determined by solving the ion concentrations for the different species and inserting them into Equation (5), where *e* is the charge constant. In the momentum equation, two body forces are introduced: the EHD coulomb force (qE) and the gravitational force (ρg). The gravitational force comes into effect during EHD melting due to the variation of density with temperature in the liquid region. The total enthalpy of the PCM can be expressed as,

$$\mathrm{H} = C_{\mathrm{p}}T + \gamma L \tag{9}$$

where L is the latent heat content of the PCM and γ is the liquid fraction, which is defined as:

$$\gamma = \begin{cases} 0 & \text{If } T < T_{solidus} \\ \dfrac{T - T_{solidus}}{T_{liquidus} - T_{solidus}} & T_{solidus} < T < T_{liquidus} \\ 1 & T > T_{liquidus} \end{cases} \tag{10}$$

The thermophysical properties of the PCM in the phase-change physics are defined as,

$$\rho = \gamma\rho_{\mathrm{liquid}} + (1-\gamma)\rho_{solid} \tag{11}$$

$$\mathrm{k} = \gamma k_{\mathrm{liquid}} + (1-\gamma)k_{solid} \tag{12}$$

where ρ and k are the density and thermal conductivity of the PCM, respectively. For the material viscosity, an exaggerated value is defined for the solid domain to eliminate the flow while applying a linear gradient in the mushy region to enhance the stability of the solution.

Table 5: Thermophysical properties of paraffin wax.

Physical property	Value
Higher melting temperature (T_{mh}), °C	63
Lower melting temperature (T_{ml}), °C	53
Latent heat (L), kJ/kg	190
Solid density (ρ_s), kg/m3	800

Liquid density (ρ_l), kg/m3 [36]	750/(0.001*(T-319) +1)
Specific heat capacity (C_p), kJ/kg K	1800 (liquid), 2000 (solid)
Thermal conductivity (K)	0.2 (liquid), 0.23 (solid)
Dielectric constant (ε)	2.1
Positive ion mobility (b), m^2/V-s [37]	$2*10^{-8}$
Viscosity (μ), kg/m s	0.01 (liquid)

3.2.2 Boundary and initial conditions

The boundary conditions applied to the numerical domain are shown in Fig. 21. For the fifteen cylindrical electrodes, a constant positive DC electric potential and charge injection current density boundary conditions were applied at the electrode surfaces. The charge injection for the positive ions is given a current density that is function of the electric field – $f_1(E)$, while zero current flux is applied for the negative ions. The top and bottom surfaces were grounded and assigned a charge loss boundary condition ($J_{i,bulk}$), while all cavity walls and electrode surfaces were given nonslip velocity boundary conditions. For the temperature field, the top and bottom surfaces were given hot and cold temperature boundary conditions, respectively, to ensure that melting progressed downwards.

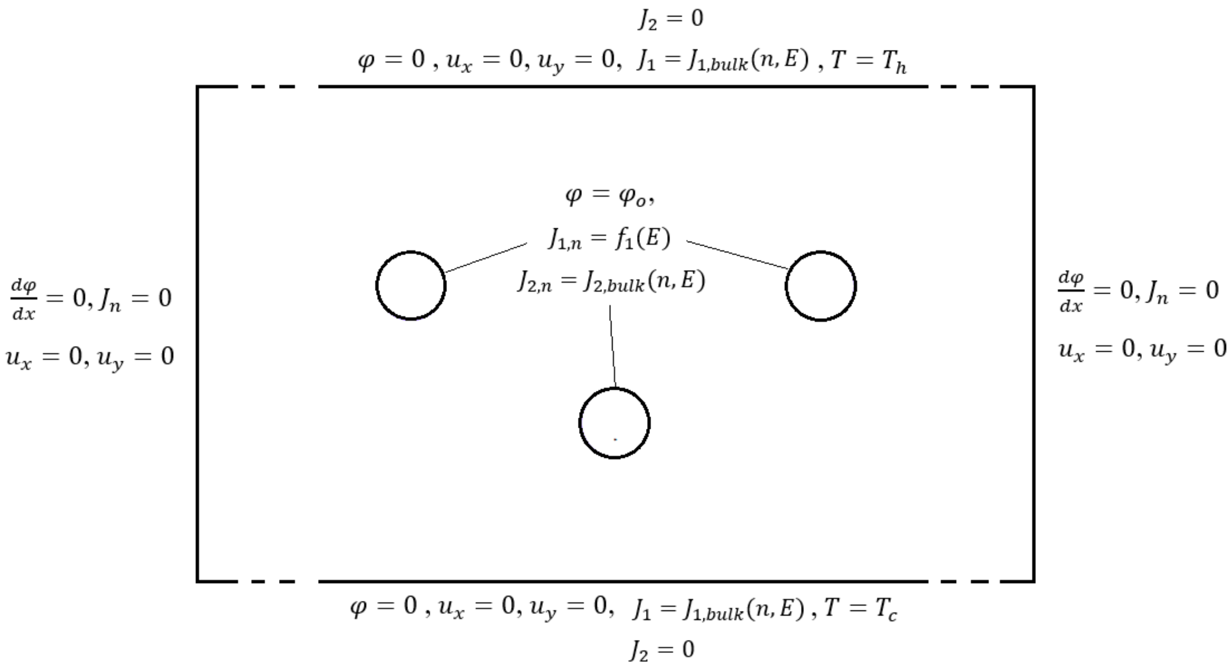

Figure 21: Boundary conditions.

The injection function used in the simulation was chosen based on the actual current voltage characteristics determined in the experiments. A linear function is applicable up to a certain voltage where the current-voltage characteristics are within the ohmic region. Beyond this region, the injection becomes very intense, and the current-voltage relation becomes nonlinear. To better represent the injection function of the positive ions current density (J1) for the whole voltage range, the following expression will be used:

$$\mathrm{f}_1(\mathrm{E}) = \mathrm{AE} + \mathrm{B}(\mathrm{E} - \mathrm{E}_\mathrm{t})^2\theta(E - E_t) \tag{13}$$

Where A and B are constants that can be varied to yield different current results that will provide a good match with the actual current-voltage relation. θ is a Heaviside step function and E_t is the threshold electric field at which the nonlinear relation will be valid. For the charge-loss boundary condition applied at the counter electrodes (top and bottom surfaces), the dissociation function is assumed to be equal to the current density coming from the bulk of the material. It can be expressed as:

$$J_{i,bulk} = \mathrm{n_i b_i E_N} - \mathrm{D_i}\nabla_N n_i \quad (14)$$

The initial temperature of the PCM was specified as the solidus temperature for the non EHD melting study. The initial conditions for the EHD study were taken from the previous state of the non-EHD study. For all other parameters, zero initial conditions were specified.

3.2.3 Computational technique

The set of governing equations was solved based on the finite element method using COMSOL Multiphysics 5.5 software. The simulation technique was performed using the time-dependent backward differentiation formula BDF solver with variable order and variable time step. The solution accuracy was controlled by setting the absolute tolerance to a maximum value of 0.5%. The time step was varied such that the solution error fell within the specified tolerance for the different parameters; if the error exceeded the limits of the defined tolerance, the solver used the nonlinear iterations method.

A structured computational mesh consisting of quadrilateral mesh elements was employed in the simulations. The selected mesh was extremely refined in the near electrode area where the charge injection takes place with very high gradients. The maximum element size in the vicinity of the electrodes was 50 µm, with a maximum element growth rate of 5%. A grid independency study was conducted to estimate the uncertainties of the simulation, with findings showing that reducing the mesh size did not change the solution by more than 0.5%. An additional accuracy investigation was performed following the numerical computations. Energy conservation and total current were compared between the different cross sections and between the inlet and outlet charge boundaries. The findings of this analysis revealed that the maximum deviation of the total current between the injection electrodes and the counter electrodes did not exceed 0.7%, while the maximum discrepancy of the total heat transfer was approximately 0.2%.

3.2.4 Model validation

Key characteristics of the current numerical study was validated via a two-step process. In the first step, the numerical modelling of charge injection in a needle-plane electrode configuration was validated against Sun et al.'s [38] experimental results. In Sun et al.'s work, the EHD flow of a single-phase dielectric liquid was investigated under constant DC voltage applied to a vertical needle plane contained in a cubical cavity. The electric current-voltage characteristics were determined by measuring the current at the ground side of the test section using a pico-ammeter, while the velocity field was obtained using PIV measurement technique. A 2D axisymmetric model was constructed for a needle-plane design resembling the experimental configuration, and the full EHD equations were then solved. The boundary conditions applied at the electrode are shown in Fig. Figure 4122. A constant electric potential and charge-creation boundary conditions were applied at the needle electrode while grounding the horizontal bottom plane. The injection function used in the simulation was the same as in Equation (13). The values of coefficients A and B were $5*10^{-16}$ mol/m-V-s and $5*10^{-24}$ mol/V^2-s, respectively, while the threshold value of the electric field was found to be $7*10^{6}$ V/m. These values are obtained based on the numerical electric current results which are fitted to give a good agreement with the experimental current-voltage characteristics.

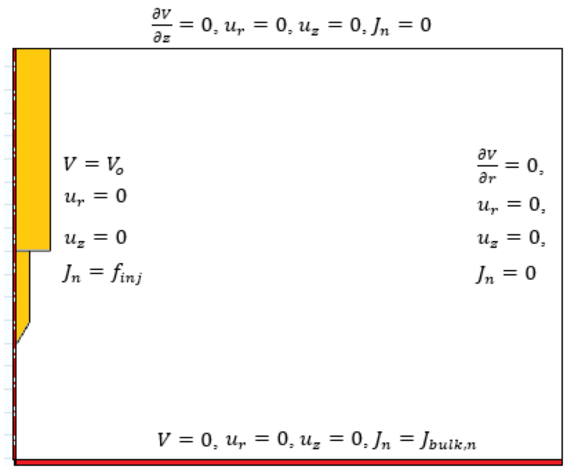

Figure 22: Numerical domain for the validation case.

The electric current can then be evaluated by applying Sato's equation to the simulation results for the current density, where the total current is determined by the volumetric integration of the current density [35], [39].

$$I = \int (J, f_E) dV \tag{15}$$

where, $f_E = E/Vo$ is the weighting electric field.

A comparison of the numerical results for the current-voltage characteristics and the experimental results is presented in Fig. 23a. As can be seen, the current-voltage relation remained linear in the ohmic region until 2 kV, after which point it became nonlinear. The results revealed that there is good agreement between the numerical simulation data and the experimental data, with a maximum discrepancy of about 5% between the results.

The numerical results for the velocity field were validated using the experimental values at +2 kV. The distribution of the vertical velocity component along the centerline at the interelectrode distance was plotted and compared with the experimental values, as shown in Fig. 23Figure 42b. As can be seen, the velocity increased from the electrode tip downwards along the vertical axis until reaching a maximum value of about 2.3 mm/s at 10 mm from the tip before starting to decrease again. Once again, good agreement was observed between the numerical results and the experimental results.

(a) (b)

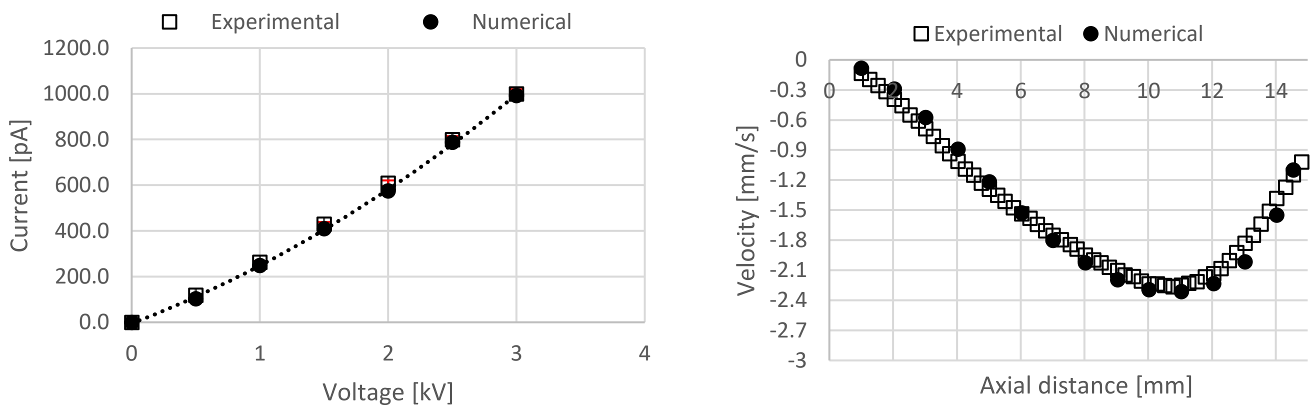

Figure 23: Validation of the numerical model at 2 kV applied voltage against Sun et al.'s experimental results [38].

In the second validation step, a numerical simulation of the 2D domain of the current study was conducted at different injection functions while varying coefficients A and B. The total current was then calculated using the same equation used in the first step (Equation (15)) and compared to the experimental results obtained by Hassan et al. [13]. As shown in Fig. 24, good agreement was achieved for a linear current-voltage relation up to 6 kV, where the value of the coefficient A is $1.2*10^{-16}$ mol/m-V-s. The maximum discrepancy between the numerical and experimental current results was within 9%.

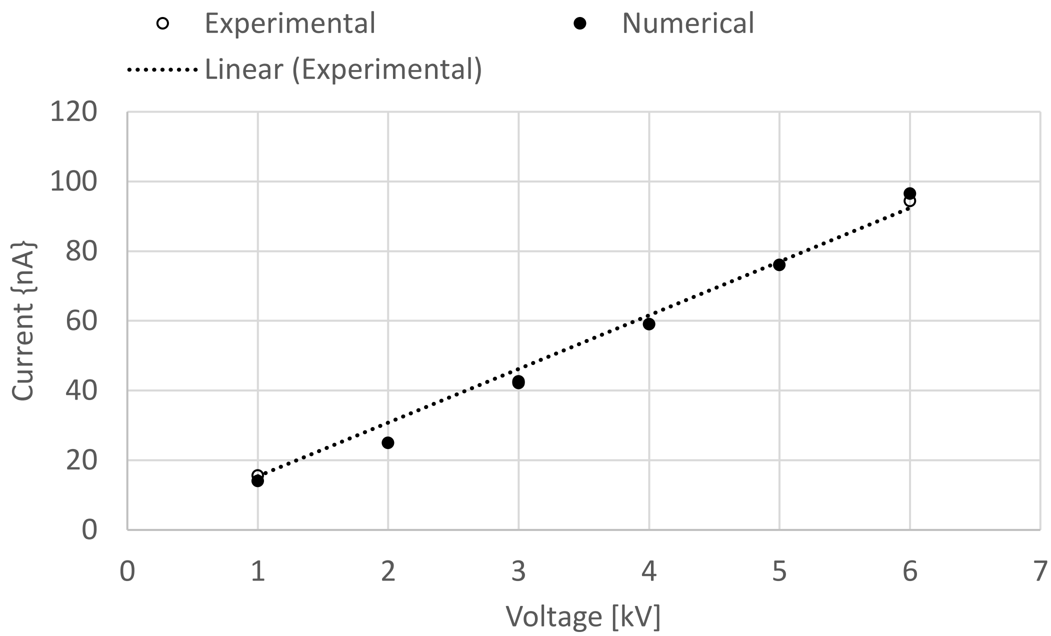

Figure 24: Validation of current-voltage characteristics.

3.3 Results and Discussion

The application of EHD under constant temperature boundaries to enhance the melting of paraffin wax in a rectangular cavity was assessed by conducting time-dependent simulations for the non-EHD and EHD melting cases. First, the melting without EHD case was numerically modelled for hot (70°C) and cold (45°C) temperatures, with simulations being performed until a steady-state condition was achieved (i.e., when the amount of the liquid fraction no longer changed with time). Next, the charge injection and phase change were numerically modelled for a two-phase system where the initial temperature field of the model was based on the final conditions of the non-EHD melting study. The EHD melting problem investigated the melting of paraffin wax under 6 kV applied voltage. The results for the non-EHD melting case are presented in the following section, followed by an analysis of the electric field and space-charge density results. Subsequently, the time evolution of the EHD flow and the thermal field are illustrated, and the enhancement of melting via the application of EHD is analyzed. Due to the symmetry of the results along the horizontal axis, only the data for a portion of the numerical domain showing five electrodes will be presented.

3.3.1 Non-EHD results

This section presents the time evolution of the non-EHD melting case up to the point where a steady state is achieved. The melt-front positions with time are shown in Fig. 25a. As can be seen, the melting face is initially flat, indicating that the melting is conduction dominated. When the melt-front approaches the first row of electrodes, the melting becomes faster in the middle region between the electrodes than in the locations opposite the electrodes due to the axial heat resistance of the electrodes, which are insulated from both ends. Fig. 25**Error! Reference source not found.**b shows the development of the liquid fraction with respect to time. Here, the melting progresses very fast in the beginning due to the high temperature difference between the top surface and the PCM. However, as thermal stratification develops, the melting slows until a steady state is achieved after about four hours wherein the liquid fraction reaches 0.45. At this point, the liquid fraction does not change with time and melting stops. In a previous work [9], an experimental value of 0.3 was reported for the steady state melt fraction for the non-EHD case. The large discrepancy between the numerical and experimental values is due to two main factors: heat loss and the large mushy zone. The steady state liquid fraction in the numerical results was higher compared to the experimental value because the former simulation results did not consider heat loss. In addition, in the experiments, heat loss resulted in an uneven melt interface, causing the melt thickness to be higher in the center of the test section than at the walls. Thus, the images of the melt-front locations do not capture the actual melt thickness in whole. Furthermore, the huge mushy zone of the paraffin wax also contributes to the higher numerical value, as this value is calculated based on the total amount of liquid, including the liquid in the mushy region.

The steady state liquid fraction and temperature contours are shown in Fig. 26. The isotherms of the PCM are shown as horizontal parallel lines due to the thermal stratification of the PCM, wherein the higher temperature boundary is the temperature of the top surface. The liquid fraction distribution of the PCM is illustrated in Fig. 26b. As can be seen, the PCM has a very thick mushy region in which the liquid fraction varies from 0 to 1, and the gradient of the liquid fraction starts from the first row of electrodes and continues to about 1 mm above the second row, largely due to the very high melting temperature range of the paraffin wax ($\Delta T_m = 10$ ℃).

(a) (b)

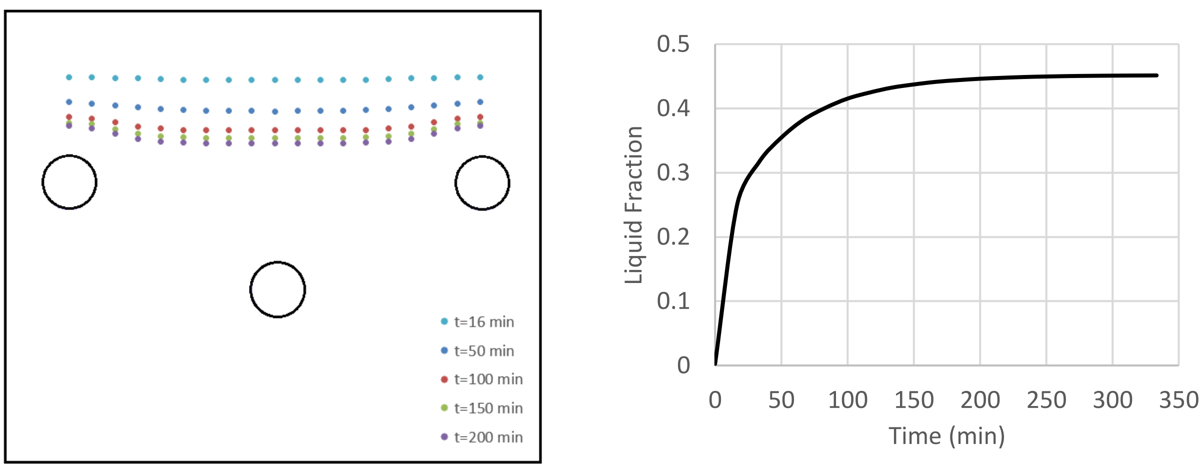

Figure 25: (a) Melt interface locations with time for non-EHD case. (b) Liquid fraction variation with time for non-EHD case.

(a) (b)

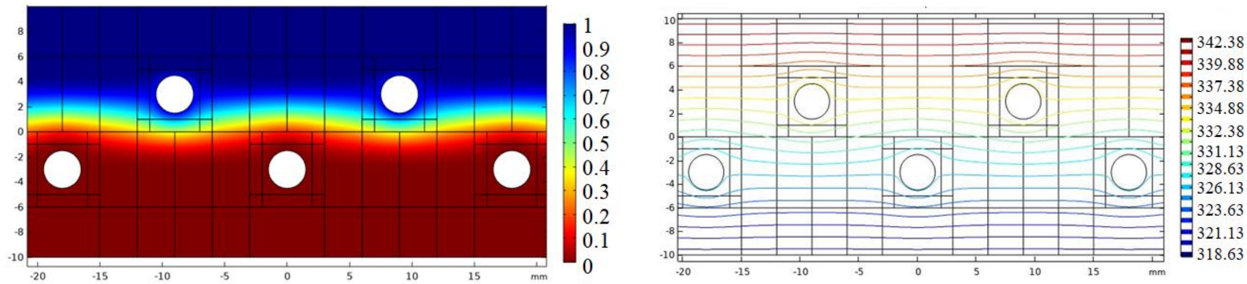

Figure 26: (a) Liquid fraction distribution at steady state in non-EHD case. (b) Temperature contours at steady state in non-EHD case [K].

3.3.2 Electrostatic analysis and EHD forces

In this section, the electrostatic results and EHD forces will be presented. The EHD is applied starting from the non-EHD steady state condition where the system consisted of a two-phase solid-liquid domain with a liquid fraction of 45%. The initial conditions for the EHD melting problem for the liquid fraction and temperature field are presented in Fig. 26.

The electric field distribution is shown in Fig. 27**Error! Reference source not found.**. The electric field is generated in the PCM following the application of EHD due to the electric potential gradient between the high voltage electrodes and the grounded surfaces. Variations in the electric field during EHD melting were found to be insignificant due to the small difference between the solid and liquid dielectric constants. The regions with the highest electric field strength were located above the top row and below the bottom row of electrodes, with a maximum value of 2 MV/m. Furthermore, a high electric field gradient between the top and bottom electrodes was observable, with an average electric field value of 560 kV/m and $E_{max} \cong 3.7\ E_{avg}$.

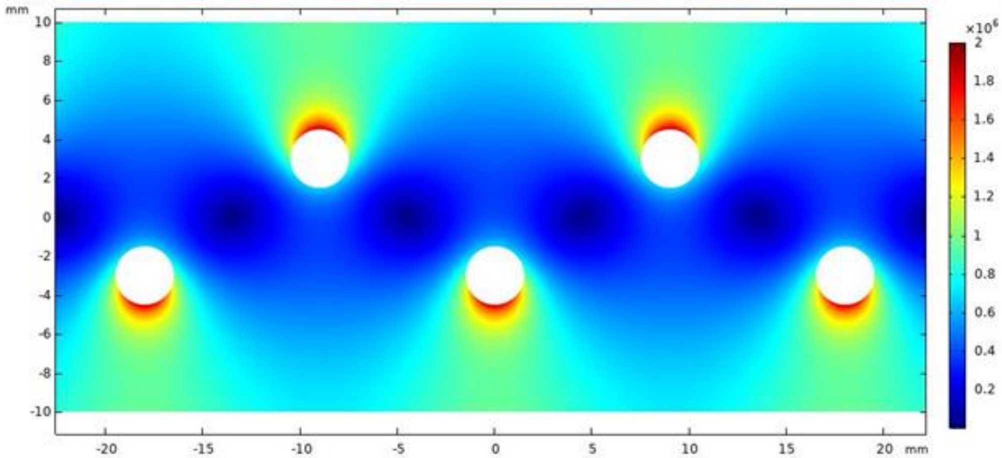

Figure 27: Electric field distribution [V/m].

Fig. 28 shows the time evolution of the space-charge density from the start of EHD until reaching a steady state. Initially, positive ions injected from the surface of the electrodes migrate in the medium along the electric field lines, forming a layer of charged jet around the electrodes. Progressively, the charged layers around each electrode grow radially towards the counter electrodes (top and bottom surfaces) until they reach the top and bottom surfaces at about t = 0.2 s, after which they begin to discharge into the ground. At t = 0.5 s, the charged layers begin to interfere with each other, forming one big, charged jet with a maximum value of about $5.8*10^{-4}$ C/m^3 in the vicinity of the electrodes. The space charge decreases away from the electrodes, where the minimum value near the ground surfaces is about 3.2 $*10^{-4}$ C/m^3. However, the space charge around the electrodes varied slightly where the minimum value observed was about $5.6*10^{-4}$ C/m^3. The conservation of the ion concentration is established in the steady state, wherein the amount of space charge in the medium stabilizes at around t = 1.8 s. The variation of the space-charge density with time was minimal during EHD melting, as the change in the electric field was very small. Fig. 28b shows the distribution of the space charge for the whole domain to illustrate the effect of the side walls. It is observed that the space charge density declines away from the electrodes towards the sides, where it is almost zero in the vicinity of the walls due to the insulation boundary conditions applied at these surfaces. This results in the charges being discharged only from the top and bottom grounded walls.

(a)

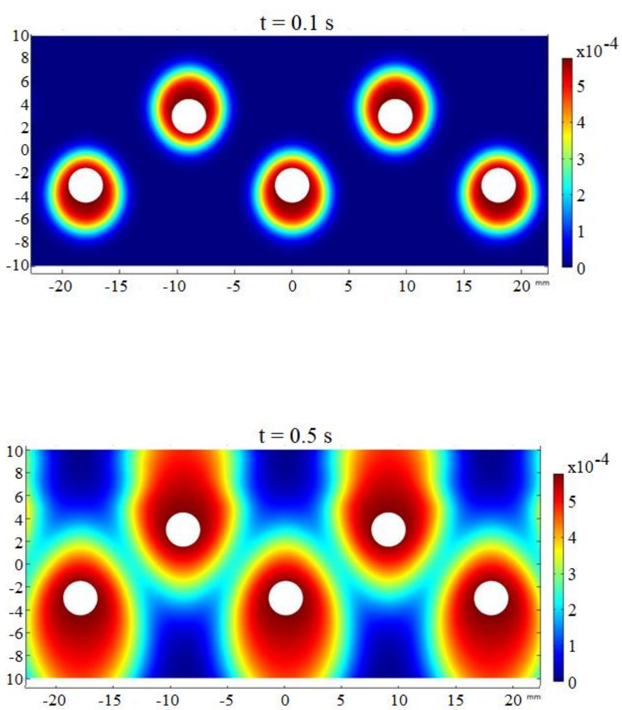

(b)

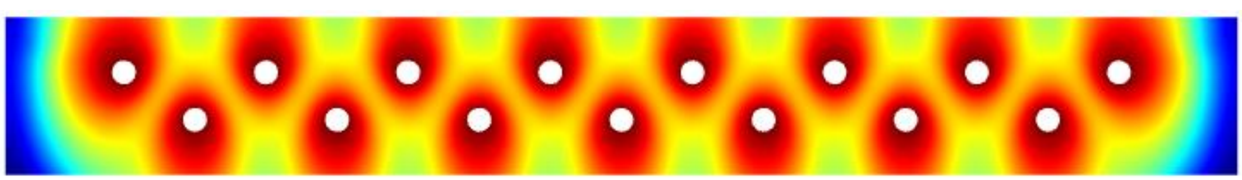

Figure 28: (a) Time evolution of space-charge density [C/m^3], (b) Space charge density results for whole domain @ t = 1.8 s [C/m^3].

The numerical results of the current-time characteristics are presented in Fig. 29**Error! Reference source not found.**. The total current is calculated using Equation (15). At the start of EHD (t = 0), the electric current is almost zero, as there are no ions in the PCM medium. The injection of charges from the surface of the electrodes results in the formation of a charged layer in the vicinity of the electrodes and the increase of the total electric current. Initially, the current density is mainly due to the migration effect, as the velocity field is very low at the beginning. Eventually, the electroconvection current becomes more prominent as the charge density around the electrodes increases. The electric current continues to increase until a steady-state condition is reached after about 1.5 s, whereupon the current flux reaches the counter electrodes and the charged jet fills the gap between the injecting electrodes and the ground electrodes. At this point, discharging commences and the total electric current begins to stabilize at about 96 nA. The very low electric current associated with EHD explains the assumption of neglecting the joule heating effect in this study.

The main mechanism of the EHD flow that drives melting enhancement is the Coulomb force, which is defined as the space-charge density mulitplied by the electric field. Since the quantity of the Coulomb force depends on both parameters, the force distribution will be similar to that of the electric field, as it is the parameter of the higher gradient. At start of EHD, the Coulomb force appears in the bulk of the medium once ion injection is initated at the electrodes. As time progressess, the Coulomb force develops along with the rise of the charged jet until it is maintained at constant level after the stabilization of the space charge at about $t = 1.8$ s from the start of EHD. The distribution of the Coulomb force and its direction at this time are shown in Fig. 30. As can be seen, the Coulomb force peaks above the top row of electrodes and below the bottom row of electrodes, with a maximum value of 1.16 kN/m^3; it then decreases gradually away from the electrodes, with very low magnitudes in the regions in between them. In addition, it is apparent that the force direction follows the electric field lines towards the regions of low electric field. The presence of the Coulomb force generates moment in the fluid which gives rise to the EHD flow, which will be discussed in the following subsection. Variations in the Coulomb force with melting were not siginifcant due to the small changes in both the electric field and the charge density during the EHD melting process.

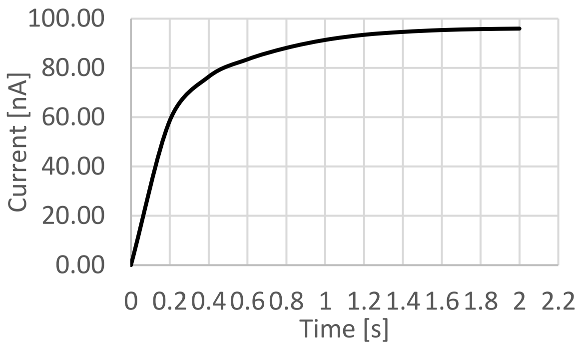

Figure 29: Total electric current evolution with time.

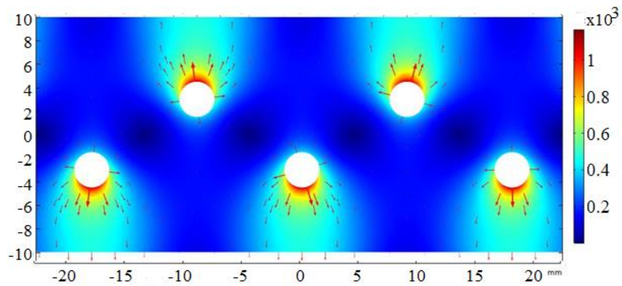

Figure 30: Coulomb force distribution [N/m^3].

3.3.3 EHD flow

The existence of the electrical body Coulomb force in the liquid bulk facilitates the generation of the velocity field or electroconvection cells, which results in the redistribution of the temperature field in the liquid PCM. Fig. 31 shows the evolution of the EHD flow field and the temperature field from the start of EHD until the stabilization of the velocity field after about 2 s. In the early stage of EHD (t = 0.1 s), two peak velocity regions can be observed opposite the electrodes, with a very thin layer of zero velocity near the interface between the liquid and the mushy zone. After this stage, the velocity field continues to develop, with the emergence of the space-charge density in the liquid bulk creating two rotational cells on both sides of each electrode. These rotational cells form due to the high Coulomb force values in the regions above the upper electrodes and the relatively lower values in the middle regions, as illustrated in Figure 11. These body forces, which are directed upwards above the electrodes, tend to move the liquid particles upwards towards the top surface; the flow then recirculates and is directed towards the low-velocity regions in the middle, creating two rotational convection cells between each electrode, as demonstrated in the streamline plot shown in Fig. 31c. After about 2 seconds, the EHD flow attains a stable flow structure due to the steadiness of the Coulomb force. The maximum velocity is found at regions closer to the electrodes and near the top surface, with a value of about 1.7 mm/s. The velocity magnitude decreases gradually in the radial direction of the rotational cell towards the center, where the velocity is almost zero. The variation of the maximum velocity with time is shown in Fig. 32. As can be seen, the velocity increases with the application of EHD due to the increase in the space-charge density until reaching a maximum value of approximately 6 mm/s at about 0.4 seconds. At this time, the first charge jet created at the electrodes reaches the ground electrodes and begins to discharge, causing the velocity to drop to a value of 1.7 mm/s after about 2 seconds as the space-charge density stabilizes. The subsequent increase in velocity is driven by the EHD melting, which results in the expansion of the liquid region and, consequently, an increase in the Coulomb force in the liquid PCM. The development of the temperature contours in response to EHD is presented in Fig. 31b. At the beginning, the contours are still horizontal parallel lines, as the electroconvection cells are still developing. As the EHD flow progressively expands in the liquid PCM, the temperature contours shift from being parallel (as in the non-EHD case) to being wavy in shape, indicating that melting is no longer conduction dominated. Additionally, the results show that the maximum temperature regions are always located in the low-velocity areas near the top surface, with the temperature at locations opposite the electrodes being lower than the temperature in the middle regions between the electrodes. This pattern is due to the flow field moving in an upwards direction opposite the electrodes and downwards in the middle. When the low-temperature fluid particles opposite the electrodes move upwards, they cool the layers of liquid in the upper area. Conversely, when the high temperature fluid particles in the middle region move downwards, they heat the liquid layers near the interface.

(a) (b)

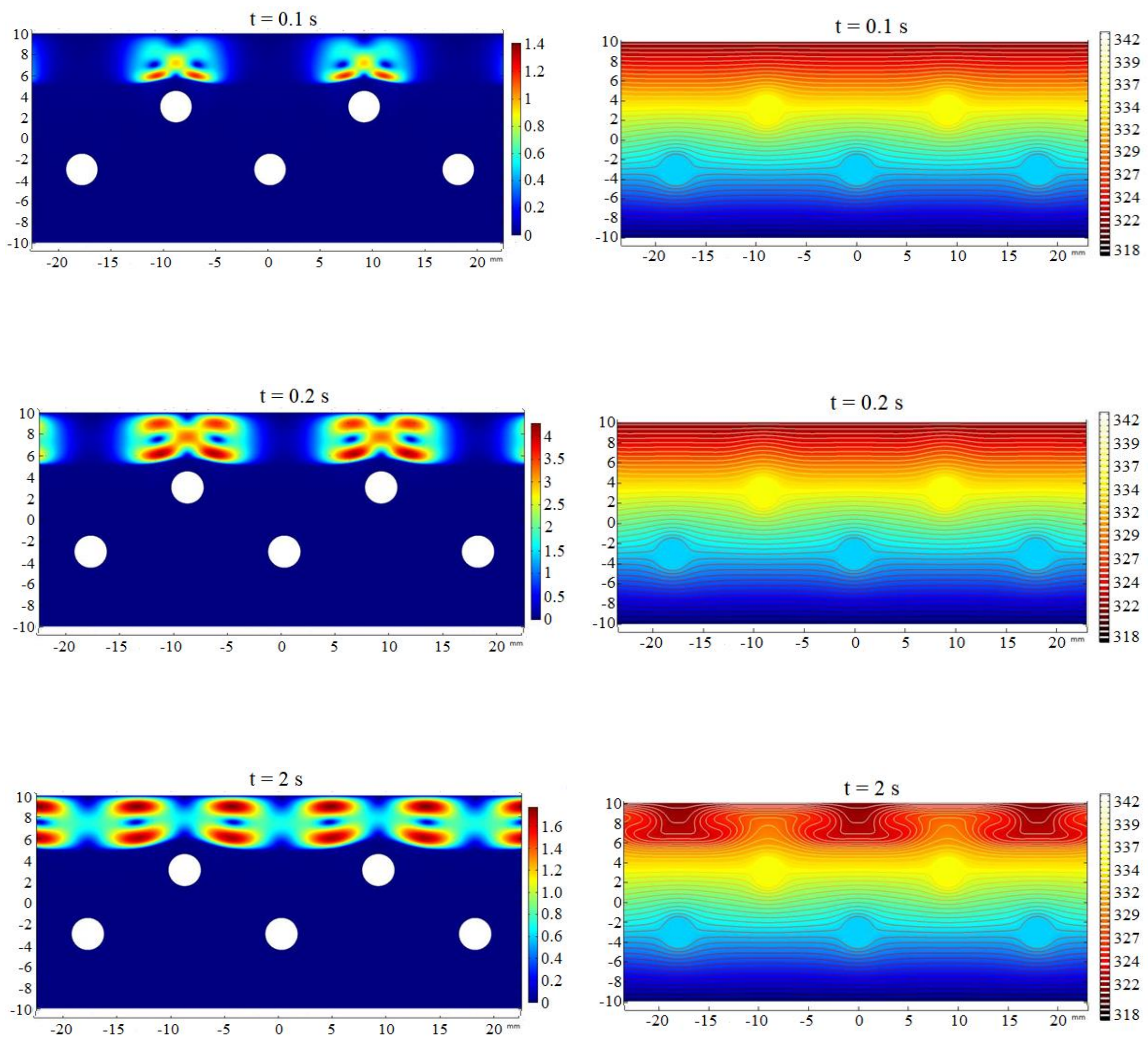

(c)

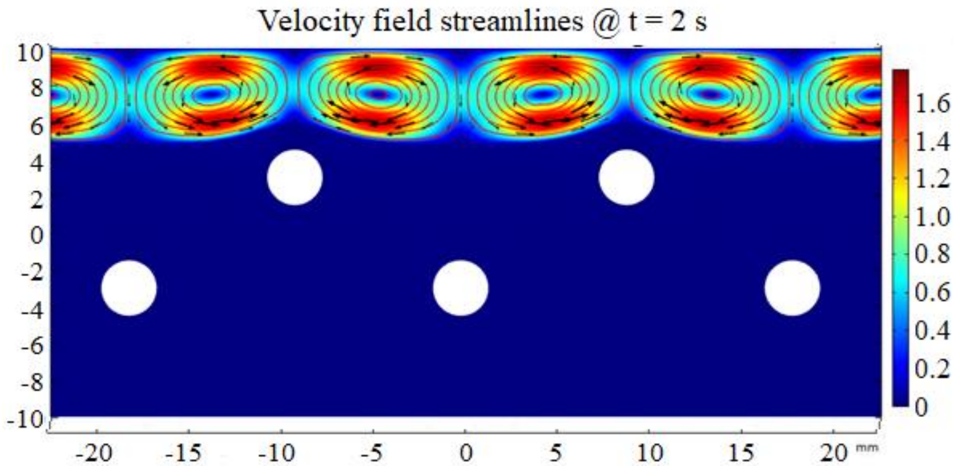

Figure 31: (a) Velocity field [mm/s], (b) temperature field [K]evolution during EHD melting at different time steps, and (c) streamlines at t = 2 s.

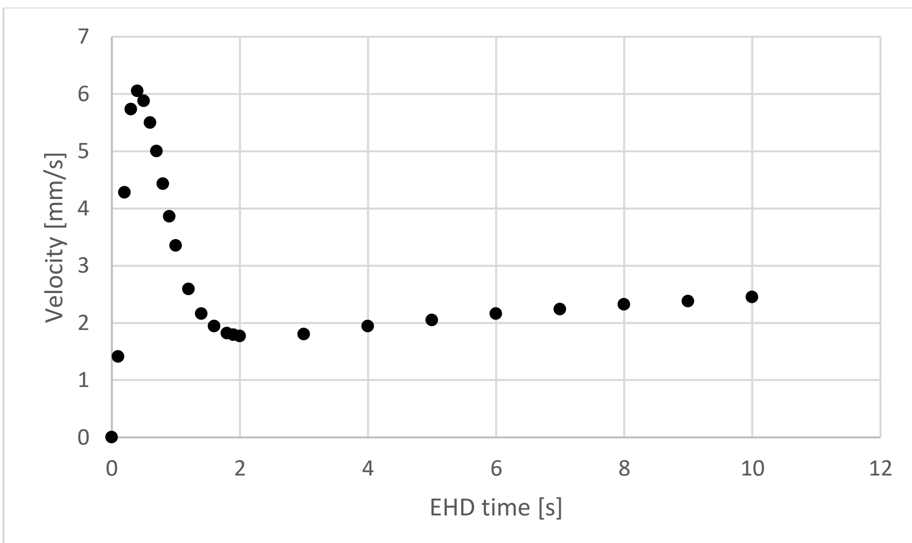

Figure 32: Maximum velocity variation with time.

Fig. 33 shows the development of the velocity field, temperature field and space charge at different time steps during EHD melting. As melting progresses, the liquid region expands and the electroconvection cells grow until they merge in the middle region between the upper electrodes, as illustrated in the last time step at t = 1 h. When the melt front moves below the upper row of electrodes, the two-roll structure of the velocity field does not change as it expands downwards, whereas the velocities below the upper electrodes are almost zero due to the damping effect from the electrodes. The maximum velocity increases with melting due to the expansion of the liquid region, which results in higher electrical body forces in the liquid PCM, where it reached about 7.9 mm/s in the EHD steady-state condition. The variation in the temperature distribution in the liquid region during EHD melting is affected by the development of the EHD flow. The wavy shape of the temperature contours can be observed throughout the melting process, where the vertical temperature distribution opposite the electrodes differs from the distribution at the vertical plane between the electrodes due to the existing rotational velocity cells. As melting progresses, the number of temperature contours decreases, indicating that the temperature distribution becomes more uniform horizontally. In the last time step, the temperature is almost uniform across the whole middle region between the electrodes; thus, the melting nearly stops at this point, and a steady state is reestablished. The variation in space charge density remains relatively stable throughout the melting process. Nevertheless, the symmetry of the space charge diminishes as a result of electroconvection evolution and increased velocity within the liquid region, unlike the unchanged space charge in the solid phase.

a b c

t = 10 s

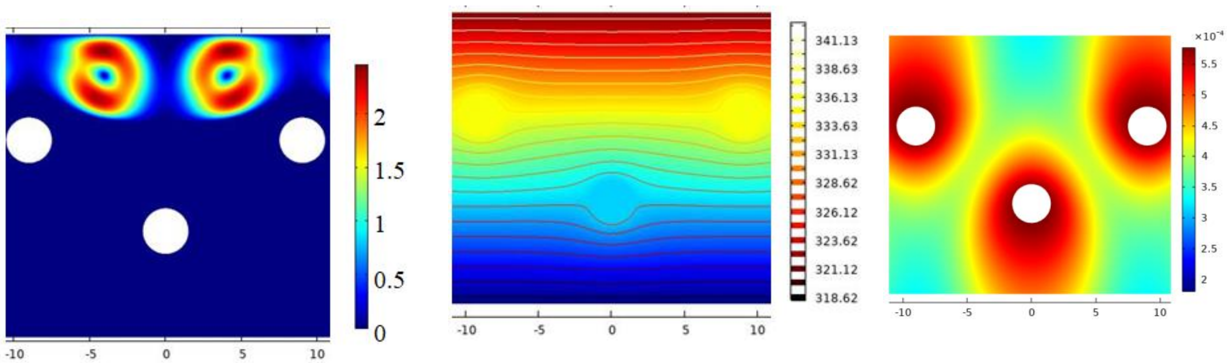

t = 60 s

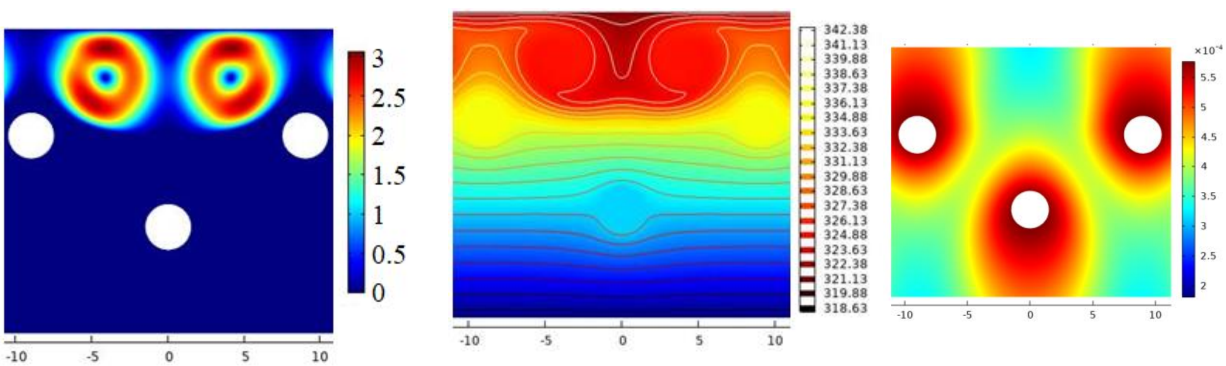

t = 300 s

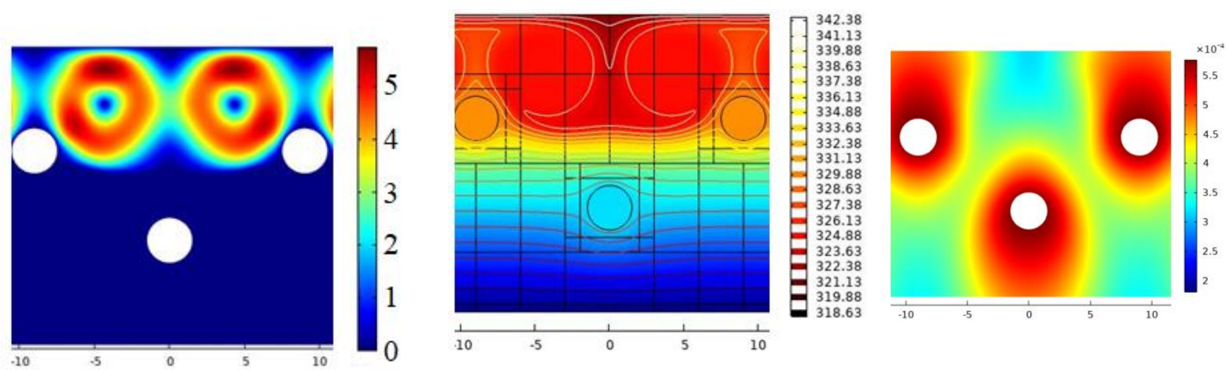

t = 600 s

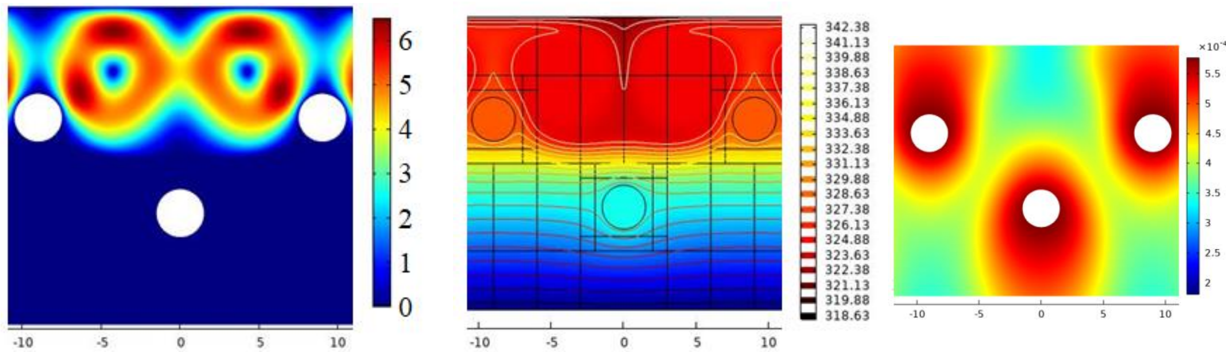

t = 3600 s

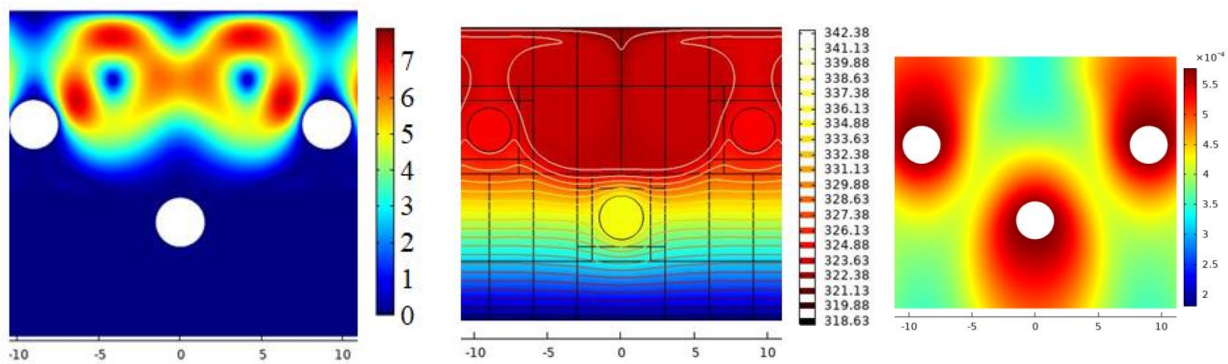

Streamlines @ t = 3600 s

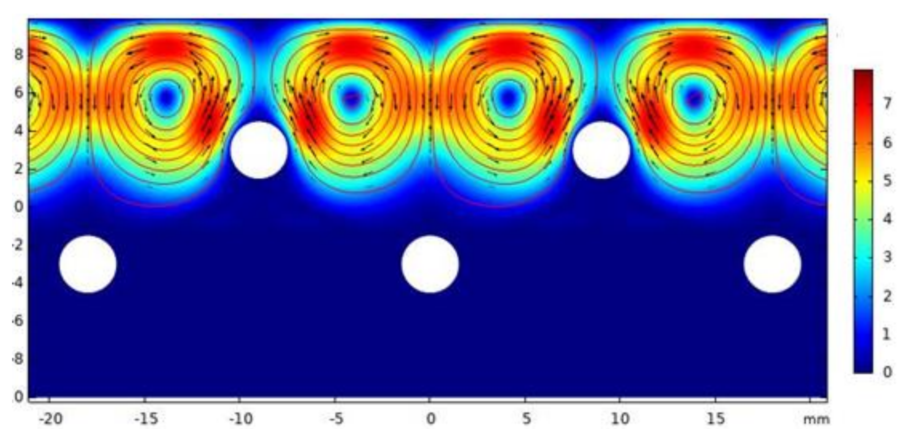

Figure 33: (a)Velocity field [mm/s], (b) temperature field [K], and (c) Space charge [C/m^3] variations during EHD melting.

3.3.4 EHD heat-transfer enhancement

As illustrated in the previous subsection, PCM melts under the effect of EHD due to the electroconvection cells generated in the liquid bulk, which causes the redistribution of the temperature field. When the temperature of the solid particles at the interface exceeds the melting temperature of the PCM, phase change will occur. Fig. 34**Error! Reference source not found.** shows the evolution of the liquid fraction during EHD melting of PCM starting from the point of non-EHD steady-state up to the establishment of another EHD steady-state condition. As can be seen, the liquid fraction increased with time, from 0.45 at the start of EHD to about 0.72 after one hour, with an enhancement factor of 1.6, where the enhancement factor is defined as the ratio of the non-EHD steady-state liquid fraction to the EHD steady-state liquid fraction. The numerical simulation was stopped after 1 hour, as the liquid fraction became almost constant with time. To compare the numerical value of the EHD melting enhancement with the experimental results determined in the previous work of Hassan et al. [13], the average melt thickness was calculated from the numerical simulations at different time steps at locations corresponding to a liquid fraction equal to 0.99. The results of this comparison are shown in Fig. 35. The average melt thickness increased from 4.9 mm in the non-EHD steady-state case to 11.5 mm after one hour of EHD. The enhancement factor calculated based on the melt thickness was 2.3, which was slightly higher than the experimental value determined in our previous study [13] (Table 6). This result can be attributed to the heat loss effect, which existed in the experiments, but was neglected in this study. However, further analysis revealed that the numerical absolute melt thickness values for both the non-EHD and EHD cases were slightly lower than the experimental values (Table 6**Error! Reference source not found.**). This finding may have been due to the melt front not being captured exactly at locations where the liquid fraction is equal to one in the experimental case due to the presence of mushy zone. Also, the effect of solid extraction at the solid-liquid interface can contribute to the melting enhancement is the experimental study [12]. The effective thermal conductivity was also calculated and compared to the experimental value, and can be expressed as a function of the EHD melt thickness (S_L) as,

$$k_{Eff} = \frac{S_{l,EHD}[k_m(T_{mh}-T_{ml})+k_s(T_{ml}-T_c)]}{(H-S_{l,EHD})(T_h-T_{mh})} \quad (16)$$

where T_{mh} and T_{ml} are the higher and lower PCM melting temperatures, T_h and T_c are the hot and cold temperatures of the top and bottom surfaces, k_m and k_s are the thermal conductivities for the mushy and solid phases, and H is the domain height. The findings showed that the numerical values for effective thermal conductivity were slightly lower than the experimental values due to the lower numerical value for the EHD melt thickness.

Table 6:Comparison between experimental and numerical results.

	Experimental	Numerical
Non-EHD melt thickness [mm]	5.8	4.9
EHD melt thickness [mm]	11.7	11.5
Enhancement factor	2	2.3
Effective thermal conductivity [W/m-K]	0.8	0.76

The locations of the melt front during EHD melting at different time steps is shown in Fig. 36a. As can be seen, the melt interface changed from being flat in shape during non-EHD melting to becoming wavy in shape during EHD melting. This shift occurred due to the melting behavior changing from conduction-dominated to electroconvection-dominated with two rotating cells between the electrodes. In addition, the observed melting rate was slower above the lower electrode due to the insulation boundary conditions applied at the electrode ends, which reduced the axial conduction through the electrodes. As shown in Fig. 36b, the melt-front shape in the EHD steady-state condition for the actual experiment has the same wavy shape observed in the numerical results, wherein the melt front locations change in the horizontal direction by about 0.4 mm between different positions. Furthermore, the interface location of the electrodes in the experimental and numerical cases were found to be comparable.

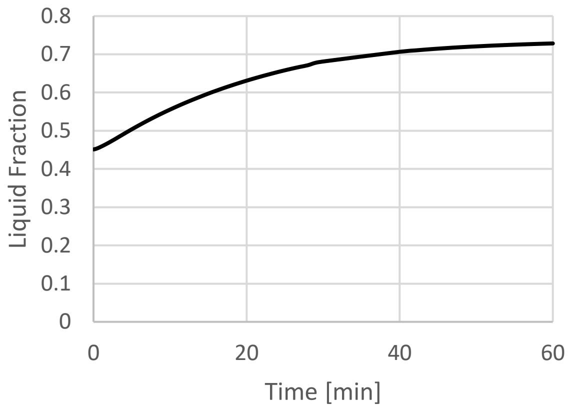

Figure 34: Liquid fraction evolution during EHD melting.

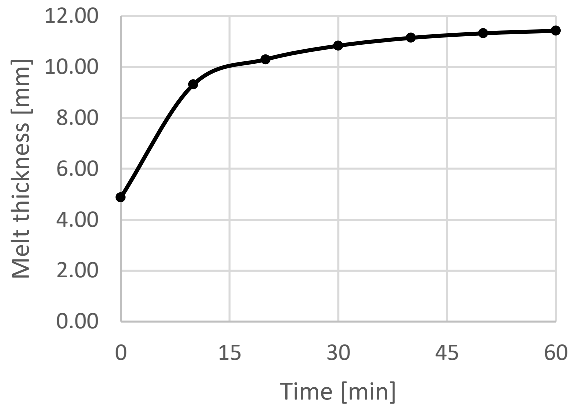

Figure 35: Melt thickness variation with time.

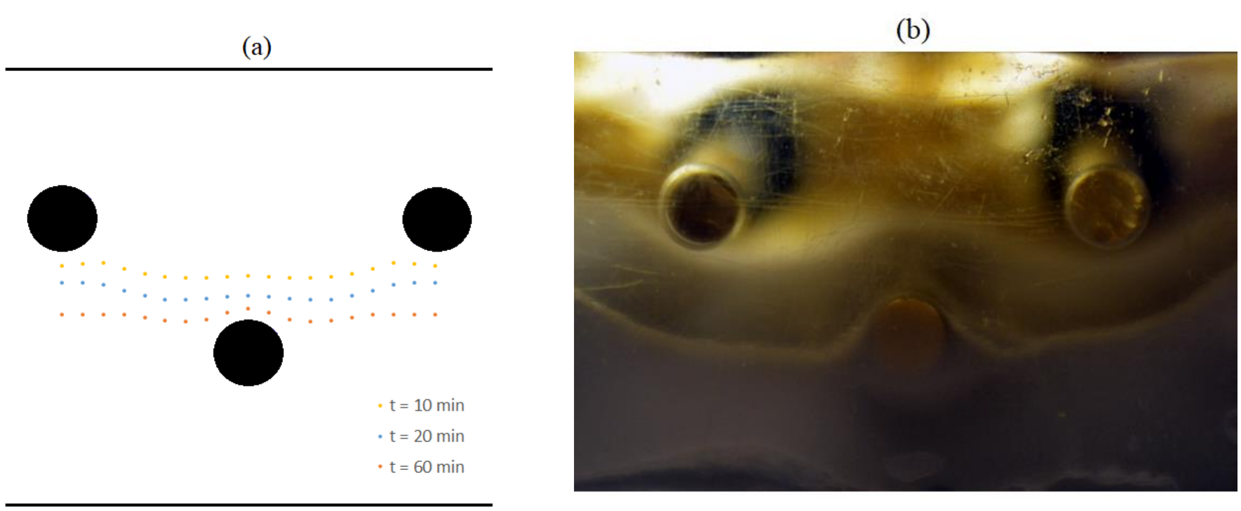

Figure 36: Melt interface locations: (a) melt interface locations at different EHD time steps, (b) experimental melt-front image in EHD steady-state condition (t=60 min).

The heat-transfer coefficient at the hot wall was calculated at different horizontal positions and different time steps, with the results being presented in Fig. 37. The variations in the heat-transfer coefficient in the horizontal direction were due to electroconvection and the redistribution of the temperature field. The heat-transfer coefficient peaks at positions opposite to the upper electrodes (x = 0, 18, 36, … mm) and their distribution were found to be symmetric around the electrodes due to the symmetricity of the two electroconvection cells created between each two successive electrodes. However, the heat-transfer coefficient dropped at the middle positions due to the lower temperature gradient in these locations compared to those opposite the electrodes. Additionally, the heat-transfer coefficients at positions opposite the first and last electrodes were slightly higher than those at the other electrodes due to the higher velocity at the sides of the domain, which is influenced by the damping effect of the electrodes. The heat-transfer coefficient's horizontal distribution with respect to the electrode locations exhibited the same trend reported by Nakhla et al. [11]. In their study, Nakhla et al. [7] experimentally studied the melting behavior of Octadecane in a vertical enclosure, utilizing a shadowgraph method to determine the heat-transfer coefficient at the hot wall. They found that the heat-transfer coefficient peaks at locations directly opposite the electrodes and falls to a minimum value at locations between the electrodes.

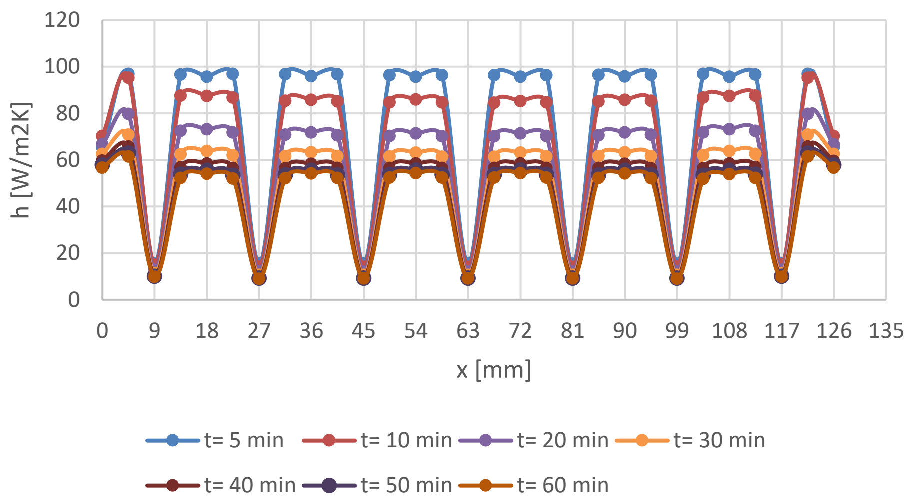

Figure 37: Horizontal distribution of the heat-transfer coefficient at the hot wall.

Fig. 38 shows how the mean Nusselt number at the hot wall varies with time. At the beginning of EHD melting, the Nu number increases due to the increase of the velocity with melting. The Nu number then starts to decrease gradually with time due to the reduction in the gradient of the liquid PCM temperature in the vertical direction. When the steady-state condition is regained, the variation in Nu becomes very small until melting stops after about 1 hour.

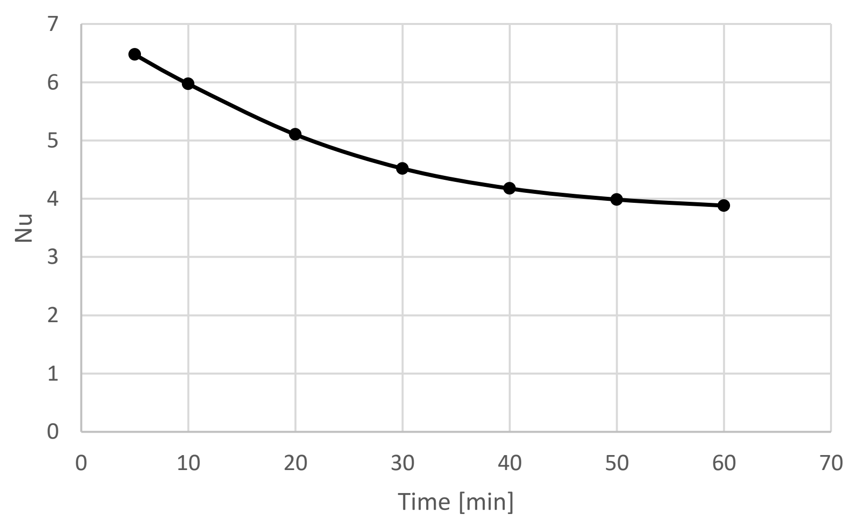

Figure 38: Mean Nu number variation with EHD time.

3.4 Conclusions

This paper presented a numerical study investigating the use of EHD to enhance heat transfer during the melting of paraffin wax under constant temperature boundary conditions. The finite element method was selected to solve the entire set of mathematical equations used to simulate the charge injection process associated with the EHD melting problem, and the numerical model was implemented to solve for the electric field, flow field, charge transport, and temperature field. The model was then validated against the experimental results reported by Sun et al. [38], who studied EHD flow for a dielectric liquid in a needle-plane electrode configuration. Next, the injection function used for the current density boundary condition at the electrodes of the studied domain was validated by comparing the numerical results for the total current with the experimental current-voltage characteristic previously reported by Hassan et al. [13]. The comparison between the numerical and experimental results showed good agreement.

The numerical results revealed that melting without EHD was conduction-dominated due to the thermal stratification of the liquid layers, as the hot wall was the top surface of the dielectric material. Melting continued until a steady state was achieved when the liquid fraction stabilized at 45%. In this case, the melt interface was located just above the upper row of electrodes. After applying EHD at 6 kV to the two rows of electrodes, melting recommenced due to the generation of electroconvection cells in the liquid PCM. The application of an electric field in the dielectric medium initiated the charge injection process at the surface of the electrodes, leading to the generation of the electrical body Coulomb force in the liquid bulk. The findings further indicated that the Coulomb force was high above the upper row of electrodes and directed upwards, thus creating two opposing electroconvection cells symmetrically positioned around each electrode. The maximum velocity reached at the beginning of EHD after the stabilization of the space-charge density was 1.3 mm/s. During EHD melting, the velocity increased due to the expansion of the liquid region, which in turn increased the Coulomb force. Melting continued until a steady-state condition was almost regained after around 1 hour, when the liquid fraction rose to a value of 72 %, with an enhancement factor of 1.6.

Subsequent analysis revealed that the numerical simulation yielded an average melt thickness in the EHD steady state that was slightly lower compared to the experimental values previously reported by Hassan et al. [9], which was likely due to the experimental results being impacted by the presence of a large mushy zone and solid extraction effects. Finally, the effective thermal conductivity calculated based on the numerical results at a voltage of 6 kV was 0.76 W/m-K and 4.8-fold increase over the PCM thermal conductivity.

Keywords

Thermal energy storage - PCM - Numerical modelling - Charge injection - COMSOL/finite element - Space charge density - Coulomb force - Electroconvection cells - EHD flow – Heat transfer enhancement.

Acknowledgements

This project was partly supported by the Natural Sciences and Engineering Research Council of Canada (RGPIN/355844). We would like to acknowledge CMC Microsystems for the provision of COMSOL that facilitated this research.

3.5 References

[1] L. Léal *et al.*, “An overview of heat transfer enhancement methods and new perspectives: Focus on active methods using electroactive materials,” *Int. J. Heat Mass Transf.*, vol. 61, no. 1, pp. 505–524, 2013, doi: 10.1016/j.ijheatmasstransfer.2013.01.083.

[2] N. I. Ibrahim, F. A. Al-Sulaiman, S. Rahman, B. S. Yilbas, and A. Z. Sahin, “Heat transfer enhancement of phase change materials for thermal energy storage applications: A critical review,” *Renew. Sustain. Energy Rev.*, vol. 74, no. October 2015, pp. 26–50, 2017, doi: 10.1016/j.rser.2017.01.169.

[3] T. Alam and M. H. Kim, “A comprehensive review on single phase heat transfer enhancement techniques in heat exchanger applications,” *Renew. Sustain. Energy Rev.*, vol. 81, no. June 2017, pp. 813–839, 2018, doi: 10.1016/j.rser.2017.08.060.

[4] Y. Lin, Y. Jia, G. Alva, and G. Fang, “Review on thermal conductivity enhancement, thermal properties and applications of phase change materials in thermal energy storage,” *Renew. Sustain. Energy Rev.*, vol. 82, no. May 2017, pp. 2730–2742, 2018, doi: 10.1016/j.rser.2017.10.002.

[5] B. Chu, “No Title,” *Phys. Fluids*, vol. 2.5, pp. 473–484, 1959.

[6] D. V. Fernandes, H. D. Lee, S. Alapati, and Y. K. Suh, “Numerical simulation of the electro-convective onset and complex flows of dielectric liquid in an annulus,” *J. Mech. Sci. Technol.*, vol. 26, no. 12, pp. 3785–3793, 2012, doi: 10.1007/s12206-012-1005-3.

[7] E. Thompson, “Electrohydrodynamic solidification of phase change materials,” 2017, [Online]. Available: http://hdl.handle.net/11375/22263

[8] D. Nakhla, H. Sadek, and J. S. Cotton, “Melting performance enhancement in latent heat storage module using solid extraction electrohydrodynamics (EHD),” *Int. J. Heat Mass Transf.*, vol. 81, pp. 695–704, 2015, doi: 10.1016/j.ijheatmasstransfer.2014.10.016.

[9] D. Nakhla, E. Thompson, B. Lacroix, and J. S. Cotton, “Measurement of heat transfer enhancement in melting of n-Octadecane under gravitational and electrohydrodynamics

(EHD) forces," *J. Electrostat.*, vol. 92, no. January, pp. 31–37, 2018, doi: 10.1016/j.elstat.2018.01.004.

[10] Z. Sun, P. Yang, K. Luo, and J. Wu, "Experimental investigation on the melting characteristics of n-octadecane with electric field inside macrocapsule," *Int. J. Heat Mass Transf.*, vol. 173, p. 121238, 2021, doi: 10.1016/j.ijheatmasstransfer.2021.121238.

[11] D. Nakhla and J. S. Cotton, "Effect of electrohydrodynamic (EHD) forces on charging of a vertical latent heat thermal storage module filled with octadecane," *Int. J. Heat Mass Transf.*, vol. 167, p. 120828, 2021, doi: 10.1016/j.ijheatmasstransfer.2020.120828.

[12] Z. Sun, Y. Zhang, K. Luo, A. T. Pérez, H. Yi, and J. Wu, "Experimental investigation on melting heat transfer of an organic material under electric field," *Exp. Therm. Fluid Sci.*, vol. 131, no. October 2021, 2022, doi: 10.1016/j.expthermflusci.2021.110530.

[13] A. Hassan and J. S. Cotton, "Investigation of the role of electrohydrodynamic forces on the heat transfer enhancement and solid extraction during melting of paraffin wax under constant temperature boundary conditions," *Int. J. Heat Mass Transf.*, vol. 204, 2023, doi: 10.1016/j.ijheatmasstransfer.2022.123831.

[14] J. Wu, P. A. Vázquez, P. Traoré, and A. T. Pérez, "Finite amplitude electroconvection induced by strong unipolar injection between two coaxial cylinders," *Phys. Fluids*, vol. 26, no. 12, 2014, doi: 10.1063/1.4903284.

[15] Y. Stishkov and V. Chirkov, "Dependence of the electrohydrodynamic flows structure in very non-uniform electric field on the charge formation mechanism," *Proc. - IEEE Int. Conf. Dielectr. Liq.*, pp. 1–4, 2011, doi: 10.1109/ICDL.2011.6015482.

[16] V. A. Chirkov and Y. K. Stishkov, "Current-time characteristic of the transient regime of

electrohydrodynamic flow formation," *J. Electrostat.*, vol. 71, no. 3, pp. 484–488, 2013, doi: 10.1016/j.elstat.2012.12.005.

[17] J. Wu, P. Traoré, M. Zhang, A. T. Pérez, and P. A. Vázquez, "Charge injection enhanced natural convection heat transfer in horizontal concentric annuli filled with a dielectric liquid," *Int. J. Heat Mass Transf.*, vol. 92, pp. 139–148, 2016, doi: 10.1016/j.ijheatmasstransfer.2015.08.088.

[18] T. F. Li, Z. G. Su, K. Luo, and H. L. Yi, "Transition to chaos in electro-thermo-convection of a dielectric liquid in a square cavity," *Phys. Fluids*, vol. 32, no. 1, 2020, doi: 10.1063/1.5126007.

[19] J. Huang, R. D. Selvakumar, Y. Guan, H. Li, P. Traoré, and J. Wu, "Numerical investigation of injection-induced electro-convection in a dielectric liquid between two eccentric cylinders," *Int. J. Heat Fluid Flow*, vol. 83, no. March, p. 108594, 2020, doi: 10.1016/j.ijheatfluidflow.2020.108594.

[20] Q. Liu, A. T. Pérez, R. D. Selvakumar, P. Yang, and J. Wu, "Numerical analysis of electrohydrodynamic instability in dielectric-liquid-gas flows subjected to unipolar injection," *Phys. Rev. E*, vol. 104, no. 6, 2021, doi: 10.1103/PhysRevE.104.065109.

[21] Z. Lu, G. Liu, and B. Wang, "Flow structure and heat transfer of electro-thermo-convection in a dielectric liquid layer," *Phys. Fluids*, vol. 31, no. 6, 2019, doi: 10.1063/1.5097562.

[22] J. Huang, Q. Wang, Y. Guan, Z. Du, R. Deepak Selvakumar, and J. Wu, "Numerical investigation of instability and transition to chaos in electro-convection of dielectric liquids between concentric cylinders," *Phys. Fluids*, vol. 33, no. 4, 2021, doi:

10.1063/5.0044147.

[23] Z. G. Su, Y. M. Zhang, K. Luo, and H. L. Yi, “Instability of electroconvection in viscoelastic fluids subjected to unipolar injection,” *Phys. Fluids*, vol. 32, no. 10, 2020, doi: 10.1063/5.0022772.

[24] A. N. Mordvinov and B. L. Smorodin, “Electroconvection under injection from cathode and heating from above,” *J. Exp. Theor. Phys.*, vol. 114, no. 5, pp. 870–877, 2012, doi: 10.1134/S1063776112030181.

[25] O. Nekrasov and B. Smorodin, “The Electroconvective Flows of a Weakly Conducting Liquid in the External DC and AC Electric Fields,” *Microgravity Sci. Technol.*, vol. 34, no. 4, pp. 1–9, 2022, doi: 10.1007/s12217-022-10002-3.

[26] A. V. Taraut and B. L. Smorodin, “Electroconvection in the presence of autonomous unipolar injection and residual conductivity,” *J. Exp. Theor. Phys.*, vol. 115, no. 2, pp. 361–369, 2012, doi: 10.1134/S1063776112070187.

[27] K. Luo, A. T. Pérez, J. Wu, H. L. Yi, and H. P. Tan, “Efficient lattice Boltzmann method for electrohydrodynamic solid-liquid phase change,” *Phys. Rev. E*, vol. 100, no. 1, pp. 1–15, 2019, doi: 10.1103/PhysRevE.100.013306.

[28] C. L. Lu, X. L. Gao, J. Wu, K. Luo, and H. L. Yi, “Heat transfer enhancement analysis of electrohydrodynamic solid-liquid phase change via lattice Boltzmann method,” *Appl. Therm. Eng.*, vol. 194, no. November 2020, p. 117112, 2021, doi: 10.1016/j.applthermaleng.2021.117112.

[29] C. L. Lu, K. Luo, P. C. Zhou, and H. L. Yi, “Lattice Boltzmann analysis for electro-thermo-convection with a melting boundary in horizontal concentric annuli,” *Phys. Fluids*,

vol. 33, no. 4, 2021, doi: 10.1063/5.0046975.

[30] R. D. Selvakumar, L. Qiang, L. Kang, P. Traoré, and J. Wu, "Numerical modeling of solid-liquid phase change under the influence an external electric field," *Int. J. Multiph. Flow*, vol. 136, p. 103550, 2021, doi: 10.1016/j.ijmultiphaseflow.2020.103550.

[31] H. E. Endigeri, R. Deepak Selvakumar, and S. Vengadesan, "Solid-liquid phase change subjected to unipolar charge injection from a circular wire electrode," *Int. J. Heat Mass Transf.*, vol. 194, p. 123120, 2022, doi: 10.1016/j.ijheatmasstransfer.2022.123120.

[32] K. He, B. Ma, and L. Wang, "Electrohydrodynamic enhancement of phase change material melting in cylindrical annuli under microgravity," *Appl. Therm. Eng.*, vol. 215, no. June, p. 119005, 2022, doi: 10.1016/j.applthermaleng.2022.119005.

[33] Y. K. Stishkov and V. A. Chirkov, "Formation of electrohydrodynamic flows in strongly nonuniform electric fields for two charge-formation modes," *Tech. Phys.*, vol. 57, no. 1, pp. 1–11, 2012, doi: 10.1134/S1063784212010240.

[34] V. A. Chirkov, Y. K. Stishkov, and A. A. Sitnikov, "Simulation of the integral electric current characteristics of unsteady-state current passage through liquid dielectrics," *IEEE Trans. Dielectr. Electr. Insul.*, vol. 22, no. 5, pp. 2763–2769, 2015, doi: 10.1109/TDEI.2015.005110.

[35] A. Gazaryan, A. Sitnikov, V. Chirkov, and Y. Stishkov, "A Method for Estimation of Functional Dependence of Injection Charge Formation on Electric Field Strength," *IEEE Trans. Ind. Appl.*, vol. 53, no. 4, pp. 3977–3981, 2017, doi: 10.1109/TIA.2017.2680398.

[36] A. V. Arasu and A. S. Mujumdar, "Numerical study on melting of paraffin wax with Al2O 3 in a square enclosure," *Int. Commun. Heat Mass Transf.*, vol. 39, no. 1, pp. 8–16, 2012,

doi: 10.1016/j.icheatmasstransfer.2011.09.013.

[37] M. S. Zadeh, “Measurement of ion mobility in dielectric liquids,” no. 66, 2011.

[38] Z. Sun, D. Sun, J. Hu, P. Traoré, H. L. Yi, and J. Wu, “Experimental study on electrohydrodynamic flows of a dielectric liquid in a needle-plate configuration under direct/alternating current electric field,” *J. Electrostat.*, vol. 106, no. October 2019, 2020, doi: 10.1016/j.elstat.2020.103454.

[39] S. Ramo, “Currents Induced by Electron Motion,” *Proc. IRE*, vol. 27, no. 9, pp. 584–585, 1939, doi: 10.1109/JRPROC.1939.228757.

Chapter 4: An investigation of the electroconvection flow and solid extraction during melting of phase-change materials

An investigation of the electroconvection flow and solid extraction during melting of phase-change materials

Ahmed Hassan, James S. Cotton*,

McMaster University, Department of Mechanical Engineering, Hamilton, Ontario, Canada

*Corresponding Author: cottonjs@mcmaster.ca

ABSTRACT

This paper presents numerical and experimental investigations of electrohydrodynamic (EHD) flow and solid extraction during melting of phase-change materials (PCMs) in a rectangular cavity under constant temperature boundary conditions. It was found that EHD generated electroconvection cells in the liquid PCM between each pair of electrodes. The fluid velocity increased with applied voltage and decreased under higher temperature gradients across the liquid region due to buoyancy suppression. In the experimental study, the high-speed imaging at the solid-liquid interface showed that dendrites were extracted from the mushy zone during EHD melting and moved upwards into the liquid bulk under the action of the interfacial EHD forces.

Nomenclature

b_i	Electric mobility (m^2/V.s)
C_p	Specific heat capacity (kJ/kg.K)
D	Diffusion coefficient (m^2/s)
e	Charge constant (C)
E	Electric field (N/m)
EHD	Electrohydrodynamic

f	Force (N)
I	Total electric current (A)
J	Current density (mol/m^{2}s)
k	Thermal conductivity (W/m.K)
n_i	Ion concentration (mol/m^3)
P	Pressure (Pa)
PCM	Phase Change Material
Pr	Prandtl number
q	Space charge density (C/m^3)
Ra	Rayleigh number
T	Temperature (K)
T_E	Electric Rayleigh number
u	Velocity field (m/s)
V	Voltage (V)

4.1 Introduction

The interaction between the electric field and velocity field (i.e., electrohydrodynamics (EHD)) is one of the most interesting techniques in fluid dynamics problems. This method offers a number of advantages—for example, it enables active control, contains no moving parts, and consumes very little power—which makes it a key factor in many industrial applications, including thermal energy storage systems, heat exchangers, and EHD pumping [1]. The EHD mechanism involves the application of high voltage to a dielectric medium to generate electrical body forces. These EHD forces induce secondary motions in the fluid, resulting in heat transfer enhancement in both single-phase and two-phase systems. The action of EHD forces on a dielectric fluid per unit volume can be expressed by the following equation [2]:

$$\bar{f}_{EHD} = q\bar{E} - \frac{1}{2}E^2\nabla\varepsilon + \frac{1}{2}\nabla[\rho E^2 \left(\frac{\partial\varepsilon}{\partial\rho}\right)_T] \quad (1)$$

The three terms on the right-hand side of the equation represent the electrophoretic (Coulomb) force, the dielectrophoretic force, and the electrostrictive force, respectively. The dielectrophoretic and electrostrictive forces, known as the polarization forces, become significant when the permittivity of the fluid changes considerably, which can occur at the interface of two-phase systems or at very high temperature gradient conditions. The Coulomb force is considered the main driving force of electroconvection in the bulk of the fluid and requires the creation of free charges in the fluid through the action of the electric field. These charges are created either by injection through the surface of the electrodes or via the dissociation of molecules in the fluid bulk. At high-voltage magnitudes, the effect of the injection mechanism dominates over the dissociation mechanism for low electrical conductivity materials [3].

In two-phase systems, EHD forces influence heat transfer enhancement through two main mechanisms: electroconvection flow and solid extraction. Electroconvection cells are generated in the liquid bulk by the electrophoretic body force. These velocity cells disturb the thermal boundary layer and promotes mixing, which lead to the increases of the heat transfer coefficient in the fluid [4]. In contrast, solid extraction takes place at the interface of solid-liquid systems during EHD melting under a high electric field gradient. Here, the extracted dendrites move upwards and melt faster in the higher temperature regions of the liquid, resulting in higher melting rates [5].

To better understand the impact of the EHD flow generated in the liquid bulk, researchers have conducted several experimental and numerical studies aimed at detecting the velocity field under the effect of EHD in different systems. Experimentally, the velocity field was mapped using particle image velocimetry (PIV) measurements, which can capture the time-dependent velocity field distribution. In PIV, the medium is seeded with small particles and laser sheet illumination is applied along the targeted 2D plane [6]. Daaboul et al. [7] used PIV to measure the dielectric liquid flow in a blade-plane geometry in order to detect the transition in charge creation between conduction and injection. To this end, DC voltage ranging from 0 to +5 kV was applied to a horizontal blade electrode while grounding a vertical plate electrode. When the voltage was between 500 and 1000 V, the generated flow moved towards the blade tip; this phenomenon was likely due to the conduction mechanism, which drives the EHD forces towards the electrode with the lowest radius of curvature (i.e., the blade). However, the direction of the flow reversed at voltages exceeding 1300 V; that is, a jet was generated at the blade tip and pushed towards the ground electrode. At these high voltages, the flow impacted the horizontal plate, and two wall jets were produced, creating opposing vortices. Louste et al. [8] performed experiments to study the EHD flow field in a cylinder-plane electrode geometry inside a closed cavity filled with HFE 7600 liquid. In this configuration, the electric field strength is about ten times stronger on the cylinder surface than on the plate surface. When high voltage was applied to the plate while the cylinder was grounded, the flow emanated from the right-hand side of the cylinder and moved around its circumference toward the plate, where it split into two wall jets that moved along the plane electrode. Variations in velocity were measured at a point midway between the plate and the cylinder, with results revealing the existence of two regimes. Below 10 kV, the velocity increased linearly alongside voltage and the flow was very stable; however, beyond 10 kV, the flow became unstable and moved in the opposite direction (i.e., the liquid was attracted by the cylinder rather than repelled by the plate). Louste et al. [7] explained the observed flow behaviour as a product of the conduction mechanism, wherein the liquid moves in the direction of higher electric field regions. Sun et al. [9] determined the EHD flow characteristics for transformer oil in a needle-plane electrode configuration. In this work, the authors performed PIV measurements to determine the velocity distribution under different applied DC voltages for both positive and negative polarities. At low voltages (V<+750 V), the conduction mechanism was dominant, with flow being directed towards the vertical electrode. At applied voltages greater than +1 kV, the direction of the flow reversed and moved towards the horizontal plate, indicating the transition to the injection mechanism. Notably, a large increase in the velocity magnitudes was observed at voltages higher than +2 kV. In addition, the velocity was found to be higher in the negative polarity cases than in the positive polarity cases due to the higher electric current in the former cases. In another experiment in Sun et al's study, AC square wave voltages were applied at the needle electrode at different frequencies. The results of these tests revealed that the fluid velocity decreased as the frequency increased up to 100 Hz, after which the flow almost disappeared. The authors explained these findings as a product of the ionic transit time—namely, that the charges did not have enough time to flow at high frequency.

With regards to two-phase melting, EHD flow was experimentally investigated during the melting of n-Octadecane in a small rectangular cavity under different applied DC voltages [10]. At +5 kV, the EHD flow was directed towards the high-voltage hot electrode, with a maximum velocity magnitude of 2 mm/s. In addition, the velocity was found to increase alongside the voltage, reaching a rate of 4 mm/s at +20 kV. However, when high voltage was applied to the cold electrode, the flow structure changed, and the velocity field became much stronger than in the first case, where the velocity reached 7.5 mm/s at +15 kV. Sun et al. [11] investigated EHD electroconvection during the melting of PCM in a cubical cavity with a high-voltage cylindrical electrode placed at the center. When +5 kV was applied at the electrode, they found that the EHD flow was very weak and directed towards the high voltage electrode, which indicates that conduction charge creation is prevailing. When the voltage was increased to +15 kV, the flow direction reversed, moving downwards towards the bottom plate. Furthermore, Sun et al. [10] observed that the velocity increased when negative polarity was applied. In a different work, Nakhla et al. [12] examined melting enhancement during the melting of n-Octadecane in a vertical rectangular enclosure with thirty electrodes embedded inside the PCM. The EHD flow was derived based on the local distribution of the heat transfer coefficient, which was determined using the shadow graph measurements. In the initial melting stage, the melt front shape was symmetrical around each electrode. As melting progressed, the influence of the buoyancy force increased, and the melt interface became tilted. The heat transfer coefficient results revealed maximum values at locations opposite the electrodes, with almost symmetrical distribution around each electrode, which suggested the existence of two counter-rotation flow cells between each row of electrodes. Finally, in the last stages of melting, the peaks of the heat transfer coefficient decreased near the top region due to the increase in gravitational forces.

Researchers have also conducted several numerical studies to investigate the electroconvection flow in both single-phase and two-phase EHD systems. With regards to single-phase systems, electroconvection flow has been numerically studied for a dielectric liquid contained between two planar electrodes [13]–[17]. In the case of natural convection, a one-roll flow structure appeared in the fluid, with the application of EHD resulting in its bifurcation into two electroconvection cells. The above studies showed that the flow pattern is influenced by two main parameters: the Rayleigh number and the electric Rayleigh number. When the Rayleigh number is high, the buoyancy force is dominant, and a two-roll flow pattern exists. When injection starts, the electric Rayleigh number becomes dominant, and the two-roll flow structure bifurcates into multiple electroconvection cells. As the electric Rayleigh number increased, so too did the cell bifurcation and velocity magnitude, resulting in an increase in the system's heat transfer [15]. Numerical studies have also been conducted to examine EHD flow in a single-phase dielectric medium between two concentric cylinders [3], [18]–[20]. In these works, charge-void regions (regions with very low space charge) were found to appear as EHD was applied, leading to the creation of two opposing rotational convective cells corresponding to each void region. Furthermore, the findings also revealed that the number of electroconvection cells is affected by the annular spacing, the radii of the electrodes, and the electric Rayleigh number. For instance, the number of rotational cells and the velocity magnitudes increase as the annular spacing decreases. Moreover, it was also found that the eccentricity and radius ratio of the electrodes can significantly affect the bifurcation of cells and the EHD flow structure [21].

Several studies examining the electroconvection flow in two-phase solid-liquid systems have been performed using the two popular configurations described above (i.e., a rectangular cavity wherein the dielectric medium is placed between two plane electrodes, and a concentric cylinder configuration). Some studies focusing on the 2D cavity configuration have initiated melting from the bottom wall [22]–[26]. The results of these works were comparable to those obtained for single-phase flow, wherein the EHD flow is characterized by a two-velocity roll structure in the liquid region, with the solid-liquid interface acting as a solid wall. The EHD flow intensifies as melting progresses from natural-convection-dominated to electrically dominated, and a number of charge-void regions are created in the fluid, which is considered a common feature of the

EHD electroconvection problem. The charge-void regions continue to adjust their structure and location as the interface moves during the melting process. When the PCM is completely melted, the problem is reduced to a single-phase EHD problem, wherein the stability of the flow structure depends on the electric Rayliegh number at this stage. In addition, studies have also considered the effects of the electric Rayleigh number (T), the Stefan number (St), and the Prandtl number (Pr). For instance, several works have shown that, as the electric Rayleigh number increases, the Coulomb force becomes stronger and the electroconvection cells further bifurcate. This reaction causes the EHD flow to intensify, which results in higher melting rates [22], [23], [25]. Selvakumar et al. [22] studied the effect of the St number, finding that the EHD flow is more effective at lower St number. This result may be due to the lower temperature gradient associated with lower St values, which leads to smaller resisting buoyancy force. Conversely, Luo et al. [22] investigated the effect of the Pr number and found that increasing this parameter will result in faster EHD onset during melting.

A number of studies have also examined EHD flow using the concentric cylinder configuration. For example, He et al. [27] numerically investigated the EHD flow during the melting of a phase-change material (PCM) under microgravity conditions, with findings revealing the creation of several radial flow vortices distributed evenly around the inner electrode. In the zero-gravity case, PCM melting proceeded for the whole domain at the same time. Furthermore, He et al. [26] found that the effect of applying gravity was more significant at low electric Rayleigh numbers, where the Coulomb force is comparable with the buoyancy force. The effect of eccentricity was also studied under zero-gravity conditions. The results of these investigations showed that the melting time increases alongside the eccentricity. Selvakumar et al. [28] examined the orientation effect for the concentric-cylinder configuration. They found that, compared to the vertical orientation, the horizontal orientation resulted in more chaotic electroconvection flow due to its lower buoyancy effect, which in turn produced more enhancement. He et al. [28] also studied the effect of the concentric-cylinder configuration's ellipticity. They observed that the EHD streamlines were similar to those of the circular cylinders, with the radial flow vortices being induced from the inner electrode and directed outwards to the outer electrode. The authors concluded that the melting time increased alongside the aspect ratio, and that the circular case (AR = 1) enabled optimal melting enhancement. In another study, Endigeri et al. [29] investigated the melting enhancement and the electroconvection induced by charge injection from a circular electrode placed at the center of a square cavity. During the initial stage of melting, two counter-rotating flow cells formed in the liquid region symmetrically to the horizontal center line. As melting progresses, the velocity increases, and the flow structure becomes asymmetric, resulting in a higher melting rate. The authors also studied the effect of increasing the electrode size, finding that larger electrodes resulted in lower melting enhancement due to the increase of the damping effect produced by the center electrode.

The other mechanism that can enable heat transfer enhancement in two-phase solid-liquid systems is solid extraction. This phenomenon was first reported by Nakhla et al. [5] in their investigation of the EHD melting enhancement of paraffin wax in a conduction-dominated melting regime. In this work, two rows of electrodes connected to a high-voltage power source were placed into a rectangular cavity filled with PCM, and a high-speed camera was used to monitor the behavior of the solid-liquid interface during the melting process. The authors observed that the interfacial EHD forces facilitated the extraction of solid dendrites from the mushy zone and their subsequent upward movement into the liquid bulk. Specifically, the melting of the dendrites increased as they moved to higher temperature regions, thus increasing the melting rate of the PCM. In a later work, Nakhla et al. [29] studied the EHD melting enhancement of n-Octadecane in conduction-dominated melting experiments. In this study, solid extraction was not observed at any of the different applied voltages, which was hypothesized to be due to the absence of a mushy zone in n-Octadecane during melting. Similarly, Thompson et al. [31] did not detect any solid extraction during their analysis of the solidification process of Paraffin wax. This outcome may have been due to the very low enhancement associated with the solidification process under EHD effect. Hassan et al. [30] studied EHD heat transfer enhancement during the melting of paraffin wax under different DC and AC voltages and constant temperature boundary conditions, with solid extraction being visualized via high-speed imaging. The results revealed the Coulomb force as the main EHD mechanism during melting. Additionally, solid extraction was detected at the different applied DC voltages, as the solid dendrites were drawn from the melt front into the liquid region by the Coulomb force. The findings further indicated that the movement of the dendrites in the liquid PCM was influenced by the electroconvection cells generated in the medium.

The above studies demonstrate that the EHD flow generated in the liquid medium is the main mechanism contributing to heat transfer enhancement in both single-phase and multi-phase systems. Prior experimental and numerical studies investigating how the electroconvection flow impacts EHD heat transfer enhancement have focused on two main electrode configurations: planar electrodes and the concentric cylinders. The results of these works show that the velocity field typically takes the form of rotational velocity cells wherein the flow is always directed from the high-voltage electrode to the ground electrode when the charge injection mechanism prevails. Furthermore, the flow pattern and the velocity magnitudes appear to be influenced by the injection strength, the temperature boundary conditions, and the liquid fraction (in two-phase systems). In the numerical works, charge injection was modeled using the autonomous injection assumption, wherein a constant space-charge-density boundary condition is applied at the emitter electrode. However, this assumption is not an accurate due to the local variation of the electric field with respect to the electrodes as demonstrated in the current work. The above-discussed works also show that solid extraction can affect melting rates in solid-liquid phase-change systems. This phenomenon requires further investigation, as understandings of it are somewhat rudimentary at present.

In the first part of this paper, the finite element method is applied to conduct a numerical study of the EHD flow in a two-phase solid-liquid system with a multiple electrode design, which is a configuration that has yet to be considered in the literature. The developed model will be applied to simulate the electroconvection EHD flow and Coulomb force at different voltage magnitudes. In addition, the effect of the resisting buoyancy force will be examined under different temperature gradients across the liquid region. The charge injection is considered the only source for charge creation in the dielectric medium. In the second part of this paper, solid extraction during the melting of Paraffin wax under constant temperature boundary conditions is experimentally investigated. In particular, we examine how different applied DC voltages and temperature gradients impact the flow behaviour of the extracted dendrites. Finally, the effect of the mushy zone on solid extraction will also be investigated via the melting of various PCMs with different mushy zone thicknesses.

4.2 Methodology

The EHD melting system considered in this study consisted of a rectangular enclosure containing a PCM, which was melted initially in a conduction-dominated regime starting from the top surface under constant temperature boundary conditions (Fig. 39). EHD was applied through two rows of cylindrical electrodes, which were installed inside the enclosure in a staggered pattern to create high electric field gradients around them. In this section, we detail the numerical methodology and experimental test facility of the EHD system employed in this work.

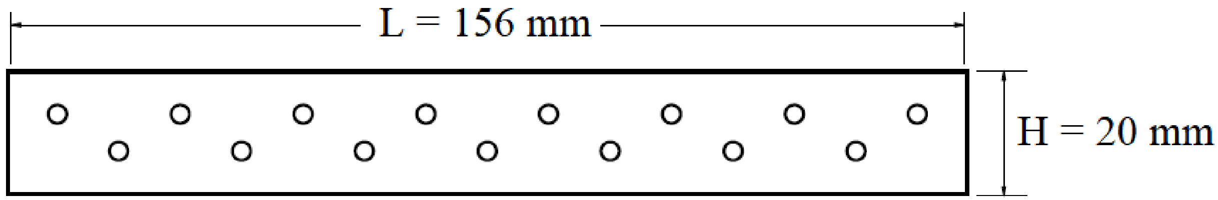

Figure 39: EHD melting system configuration.

4.2.1 Numerical Methodology

A 2D numerical domain was constructed based on the EHD system under consideration. The domain material was given the properties of paraffin wax, and the circular electrodes were defined using the properties of copper (k = 400 W/m K and Cp = 385 J/kg K). The thermophysical properties of paraffin wax are presented in Table 7. The electric permittivity of the paraffin wax is assumed to be homogenous for the whole domain, while the change in permittivity between the solid and liquid phases is neglected due to its low gradient at the interface which did not change the results of the simulations. The ion mobility of the material was set to $2 * 10^{-8}$ $m^2/V*s$ [31], while the diffusion coefficient was overestimated ($D = 10^{-7}$ m^2/s) to accelerate the convergence of the model and increase the numerical stability. This was acceptable, as exaggerating this value had an insignificant impact on the results, as the diffusion current has a relatively low contribution compared to the migration and convection currents.

Table 7: Thermophysical properties of paraffin wax.

Physical property	Value

Melting temperature range, °C	63 – 53
Latent heat, kJ/kg	190
Mass density, kg/m3	800 (solid), 750/(0.001*(T-319) +1) (liquid)
Specific heat capacity, kJ/kg K	1800 (liquid), 2000 (solid)
Thermal conductivity	0.2 (liquid), 0.23 (solid)
Electrical permittivity (liquid)	2.1
Viscosity, kg/m s	0.01

The coupled set of governing equations used to model the EHD melting problem and the charge injection process are given as follows:

$$\vec{E} = -\nabla\varphi \tag{2}$$

$$\nabla.(\varepsilon_o \varepsilon_r \vec{E}) = q \tag{3}$$

$$\frac{\partial n_i}{\partial t} + \nabla.[n_i b_i \vec{E} + n_i \vec{U} - D_i \nabla n_i] = 0 \tag{4}$$

$$\mathrm{q} = e(n_1 - n_2) \tag{5}$$

$$\nabla.\vec{U} = 0 \tag{6}$$

$$\rho \frac{\partial \vec{U}}{\partial t} + \rho\left(\vec{U}.\nabla\vec{U}\right) = -\nabla P + \mu\nabla^2\vec{U} + \mathrm{q}\vec{E} - \rho g \tag{7}$$

$$\frac{\partial T}{\partial t} + \nabla.(\vec{U}\frac{\mathrm{H}}{C_p}) = \nabla.(\alpha\nabla \mathrm{T}) \tag{8}$$

The above set of equations contains the Poisson equation, the Nernst-Planck equation for charge transport, the continuity equation, the momentum equation, and the energy equation. In these equations, φ is the electric potential, E is the electric field, q is the space-charge density, n_i is the ion concentration for the positive and negative species, u is the fluid velocity, P is the dynamic pressure, H is the total enthalpy, and T is the temperature. The symbols, ε, b, D, μ, ρ, and α, represent the electrical permittivity, ionic mobility, diffusion coefficient, dynamic viscosity, mass density, and thermal diffusivity, respectively. The ion conservation equation (Equation 4) shows the three different modes for ion transport through the dielectric medium, namely: charge migration due to the electric field, charge convection due to the flow field, and diffusion transport. The space-charge density is calculated using Equation 5, where e is the charge constant.

In the momentum equation, the EHD Coulomb force is added as a volume force due to the existence of free charges in the medium and can be expressed as: $f_c = q*E$. The gravitational force term ($\rho*g$) in the equation represents the buoyancy effect due to the density variation in the liquid region during the EHD melting process. The Navier Stokes equations are solved for the whole domain in the transient model. The viscosity of the material is given an exaggerated value for the solid domain to eliminate the flow while applying a linear gradient in the mushy region to enhance the stability of the solution.

In the energy equation, the Joule heating effect is neglected due to the very low current associated with the EHD problem. The total enthalpy of the PCM can be expressed as,

$$\mathrm{H} = \mathrm{c_p} T + \gamma L \tag{9}$$

where L is the latent heat content of the PCM and γ is the liquid fraction, which is defined as:

$$\gamma = \begin{cases} 0 & \text{If } T < T_{solidus} \\ \dfrac{T - T_{solidus}}{T_{liquidus} - T_{solidus}} & T_{solidus} < T < T_{liquidus} \\ 1 & T > T_{liquidus} \end{cases} \tag{10}$$

The thermophysical properties of the PCM in the phase-change physics are defined as,

$$\rho = \gamma\rho_{\text{liquid}} + (1-\gamma)\rho_{solid} \tag{11}$$

$$\text{k} = \gamma k_{\text{liquid}} + (1-\gamma)k_{solid} \tag{12}$$

where ρ and k are the density and thermal conductivity of the PCM, respectively.

The physical configuration of the two-dimensional numerical domain is shown in Fig. 40. A constant positive DC voltage was applied to all the cylindrical electrodes while grounding the top and bottom walls (φ=0). The four sides of the domain and the electrodes' surfaces were assigned nonslip velocity boundary conditions (u=0). The top and bottom surfaces were maintained at constant temperatures, T_h and T_c, respectively, while the side walls were adiabatic.

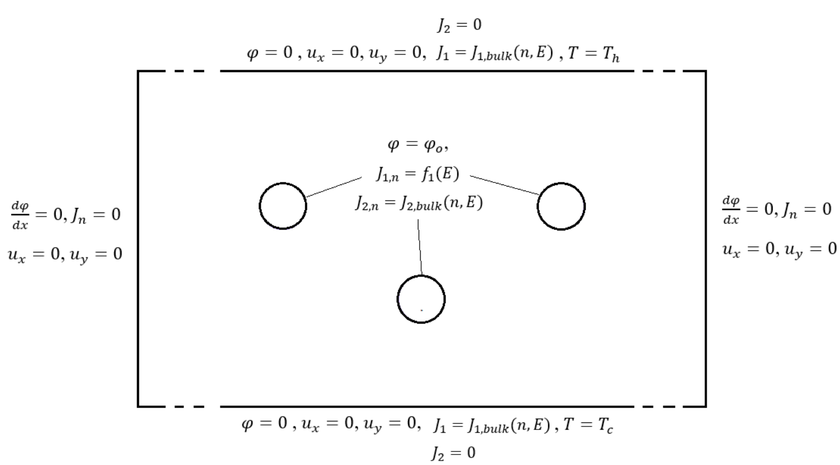

Figure 40: Physical domain and boundary conditions.

Charge injection was modeled using a nonautonomous unipolar injection model in which a current-density boundary condition is applied to the high-voltage electrodes. For the positive charges a current density that is functionally dependent on the local electric field is applied, while zero current flux is applied for the negative ions. The injection function, $f_1(E)$, was determined by evaluating the total electric current from the simulation at different electric potential boundary conditions and then comparing the results with the experimental current-voltage characteristics.

To achieve an accurate representation of the injection function, a Heaviside step function (θ) similar to the one previously used by Gazaryan et al. [32] was considered. The mathematical expression presented in Equation (13) shows that the current density is linearly dependent on the electric field up to a threshold value (E_t). When the electric field exceeds this value, another second-order term is added, and a nonlinear relationship between current-voltage characteristics will be valid.

$$\mathrm{f_{inj}} = \mathrm{AE} + \mathrm{B}(\mathrm{E} - \mathrm{E_t})^2\theta(E - E_t) \qquad (13)$$

In the linear part of the equation, the current-voltage characteristics are within the ohmic region, and the slope of the function is dependent on the coefficient (A). When the second-order term is applied, the injection strength becomes very high, and the nonlinear relation becomes dependent on another coefficient (B). The values of coefficients A and B were iterated until the total numerical electric current results matched the experimental values at each voltage. The total numerical electric current was evaluated using Sato's equation, with the total current being determined via the volumetric integration of the current density [32], [33].

$$I = \int (J, f_E) dV \tag{14}$$

where $f_E = E/Vo$ is the weighting electric field.

Charge-loss boundary conditions (f_{loss}) were applied at the top and bottom grounded surfaces where a current-density dissociation function was considered. The f_{loss} function presented in Equation (14) assumes the current density at the walls is equal to the current density arriving from the bulk of the medium and can be expressed as:

$$f_{loss,i} = n_i b_i E_N - D_i \nabla_N n_i \tag{15}$$

The non-EHD melting simulation was first conducted with an initial specified temperature equal to the solidus temperature of paraffin wax and validated against the experimental results. Next, the EHD melting study was performed with initial conditions specified from the previous state of the non-EHD study.

The fully coupled governing equations were then solved using the finite element method and COMSOL Multiphysics 5.5 software. The computational method applied in the simulations used a time-dependent backward differentiation formula BDF solver with variable order and variable time steps. To control the solution accuracy, the absolute tolerance was set to a maximum value of 0.5%, and the time step was adjusted accordingly to maintain the solution error within the specified tolerance for the different parameters: if the error exceeded the limits of the defined tolerance, the solver switched to the use of the nonlinear iterations' method.

A structured designed mesh consisting of quadrilateral elements was used to discretize the computational domain. The mesh was designed to be highly refined near the electrodes, where there are high gradients of space-charge density. In this region, the mesh elements were limited to a maximum size of 50 µm, but they gradually increased in size with distance away from the electrodes, with a maximum element growth rate of 5%. To assess the uncertainties of the simulation, a grid independency study was conducted, with results indicating that reducing the mesh size did not cause the solution to vary by more than 0.5%. Following the numerical simulations, an additional investigation was conducted to further assess the accuracy of the results. In this investigation, the energy conservation and total current were compared between different cross sections and the inlet and outlet charge boundaries. The analysis revealed that the maximum deviation of the total current between the injection electrodes and the discharge walls did not exceed 0.7%, while the maximum discrepancy between the energy in and out of the system was approximately 0.2%.

4.2.1.1 Model Validation

The numerical model was validated against the experimental results of Sun et al.'s [9] investigation into the characteristics of electroconvection flow induced by the application of EHD into a single-phase dielectric liquid. The EHD system examined by Sun et al. had a needle-plane configuration in which high voltage was applied to the needle electrode and the bottom horizontal plate was grounded. The electric current was measured using a pico-ammeter connected at the ground side of the test section, while a PIV system was used to determine the velocity field for the EHD flow.

To validate the current EHD model, a 2D axisymmetric domain was constructed for a needle-plane design resembling the system used in Sun et al.'s study (Fig. 41). For the validation tests, a constant electric potential and charge-creation boundary conditions were applied at the needle electrode, and the horizontal bottom plate was grounded. The injection function used in the simulation was the same as in Equation (13). The values of the coefficients A and B were varied to yield different current-voltage results until a good match was achieved between the numerical and experimental total electric current results. The full EHD governing equation was solved using COMSOL Multiphysics software.

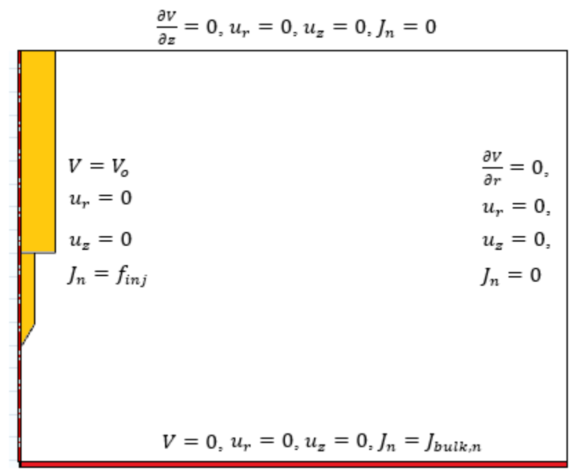

Figure 41: Numerical domain for the validation case.

The numerical results for the total current at different applied voltages were then plotted against Sun et al.'s experimental results (Fig. 42a). As can be seen, the relationship between the current and the voltage remains linear in the ohmic region until it exceeds 1 kV, at which point it becomes nonlinear. Additionally, good agreement between the numerical and experimental results can be observed, as the maximum discrepancy between the results does not exceed 5%.

The numerical results for the velocity field were validated using the experimental values at +2 kV, and the distribution of the vertical velocity component along the centerline at the interelectrode distance was plotted and compared with the experimental values (Fig. 42b). The velocity increased from zero at the electrode surface, following a downward direction along the vertical axis until reaching a maximum value of about 2.3 mm/s approximately 10 mm from the tip before beginning to decrease again. Once again, good agreement was observed between the numerical and the experimental velocity profile.

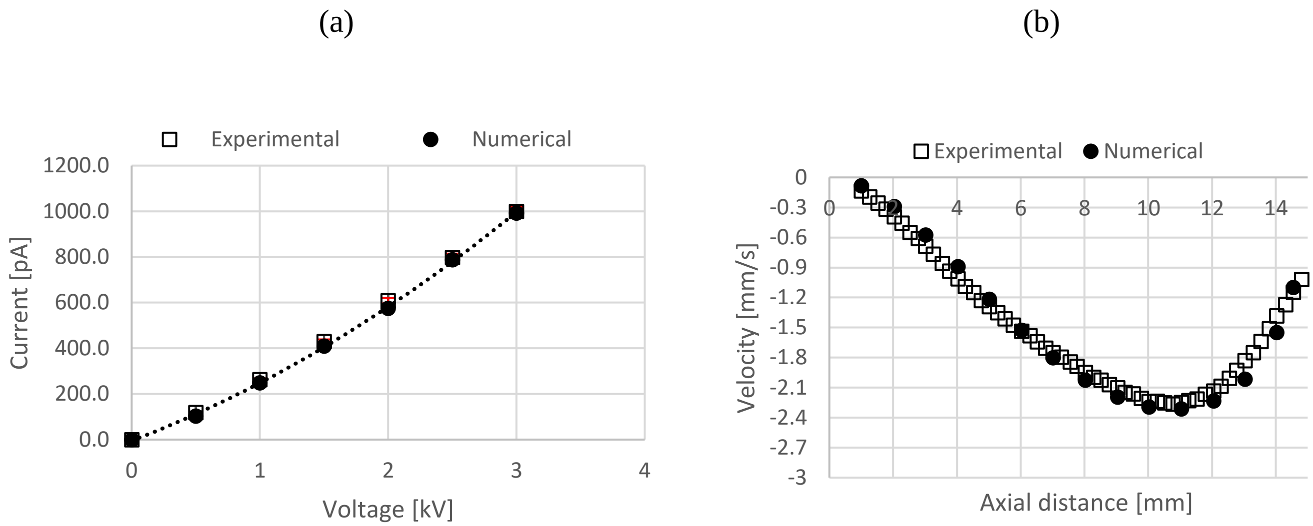

Figure 42: Validation of the numerical model against the experimental results of Sun et al. [9] at 2 kV applied voltage (a) current voltage characteristics, (b) vertical velocity profile at the inter-electrode gap.

4.2.2 Experimental Methodology

An experimental setup was implemented to facilitate high-speed imaging of the melt interface during EHD melting of PCMs under constant temperature boundary conditions. A schematic of the experimental facility is shown in Fig. 43. The test facility consisted of a rectangular test section, which was constructed of transparent acrylic on all four sides to enable solid extraction visualization. The top and bottom surfaces were attached to aluminum heat exchangers, which were supplied with water using two thermal baths: NESLAB RTE-10 and PolyScience AP15R-30. The water from the thermal baths was supplied at high flow rates to maintain the heat exchangers at nearly constant temperatures. Melting was forced to start from the top surface and advance downwards by maintaining the top and bottom heat exchangers at hot (T_h) and cold temperatures (T_c), respectively. The acrylic sides of the test section were insulated using glass wool thermal insulation throughout the experiment to minimize heat loss to the surroundings. During high-speed imaging, the insulation on one side was removed and reinstalled again after capturing the images. Two rows of cylindrical copper electrodes were installed horizontally inside the enclosure in a staggered configuration (Fig. 43). All the electrodes were supplied with high voltage using a Matsusada DC power supply, and both heat exchangers were connected to the ground.

The temperatures of the heat exchangers were measured at positions corresponding to the inlets and outlets of the water supply using type-T thermocouples to ensure the water was being maintained at nearly constant temperatures. The maximum allowable temperature deviation along the heat transfer surfaces was set at 0.3 °C. The ambient temperature was recorded with another type-T thermocouple to verify the experiments were being conducted within an ambient temperature range of 23–25 °C. A data acquisition card (NI-DAQ 9211) was used to output the temperature data into a computer, where it was monitored and recorded. The uncertainty of the temperature readings was ±0.2 °C. Solid-extraction visualization was conducted using a FASTCAM SA4 high-speed camera with a frame rate of 125 f/s. The high-speed videos were analyzed using FV4 software, with the size and velocity of the dendrites being measured at different locations during EHD melting. The uncertainties of the velocity and size measurements were ±0.1 mm/s and ±0.1 mm, respectively. Finally, the electric current was measured using a pico-ammeter DMM6500 with a sensitivity of 10 pA that was connected to the ground side of the test section across a 500 kΩ shunt resistance.

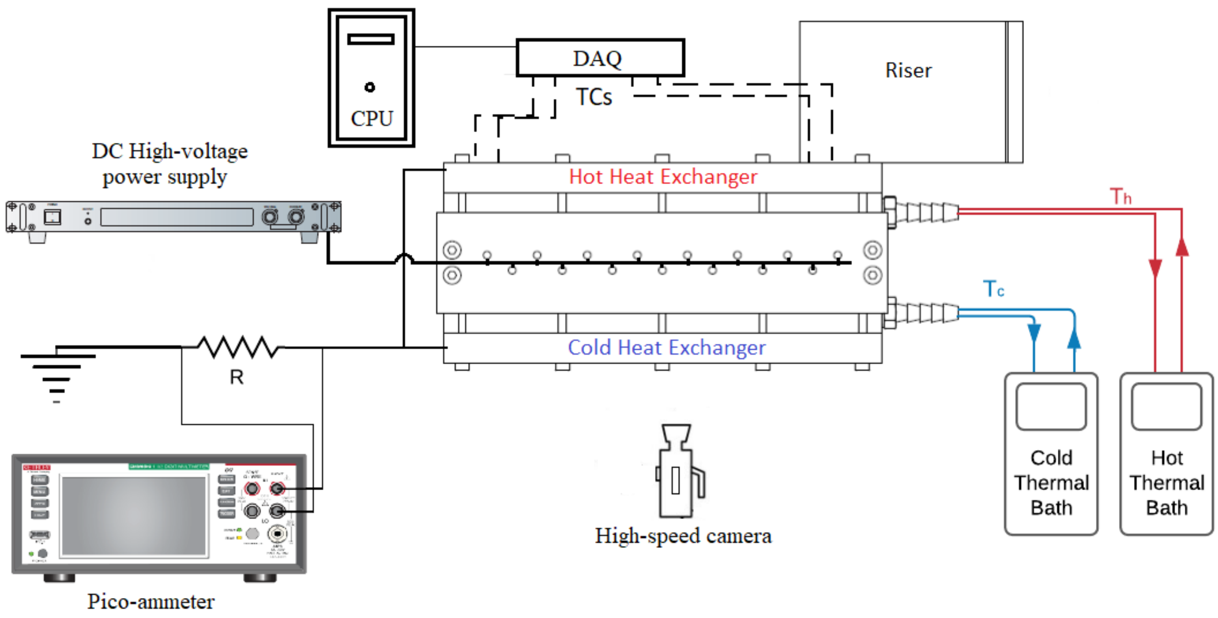

Figure 43: Experimental constant temperature boundary EHD test facility.

The experimental procedures for the EHD melting were as follows. First, the thermal baths were operated at specified temperature limits for the experiment while recording the temperature readings of the top and bottom surfaces of the heat exchangers. Melting commenced when the temperature of the top surface exceeded the melting point and continued to advance downwards in a conduction dominated regime. When melting had stopped and a steady state condition had been reached, high voltage was applied to the copper electrodes to initiate EHD and high-speed imaging was conducted concurrently.

4.3 Results and Discussion

This section details the results of our investigation of electroconvection flow and solid extraction during the melting of PCMs under constant temperature boundary conditions. First, the electric current experimental results are assessed to identify the proper injection function for use in the EHD model. Next, the results of the EHD melting problem are presented, including the effects of varying the magnitudes of the applied voltages and temperature gradients on the electroconvection flow. We then discuss the experimental results of the solid extraction characterization at different voltages and temperature gradients, as well as for PCMs with varying mushy zone thicknesses. Finally, the EHD flow deduced from the experimental solid extraction visualization is compared with the velocity distribution from the numerical results.

4.3.1 Preliminary Electric Current Measurements

This section presents the experimental measurements of the electric current at different applied voltages, which were subsequently used to validate the numerical results of the total electric current. In the experiments, the PCM was completely melted by adjusting the top and bottom surfaces to a temperature 12 °C above the high melt temperature, and the current measurements were obtained once the EHD had commenced. After each experiment, the power supply was turned off, and the test section was discharged by connecting it to the ground. As can be seen in Fig. 44, the current-voltage characteristics appear to be linear up to the maximum applied voltage (6 kV), suggesting that the relation lies within the ohmic region. Therefore, in the numerical simulation, the linear term of the injection function was used while varying the coefficient A, and the total electric current was calculated at the different applied voltages. A good match was achieved between the numerical and experimental current results at A = 1.2×10^{-16} mol/m-V-s, with a maximum discrepancy of about 9%. Furthermore, it is worth noting that the maximum electric current was about 95 nA, thus indicating that the joule heating effect could be neglected as the maximum heating effect (electric power consumption) was only 0.6 mW representing less than 0.1% of the total energy.

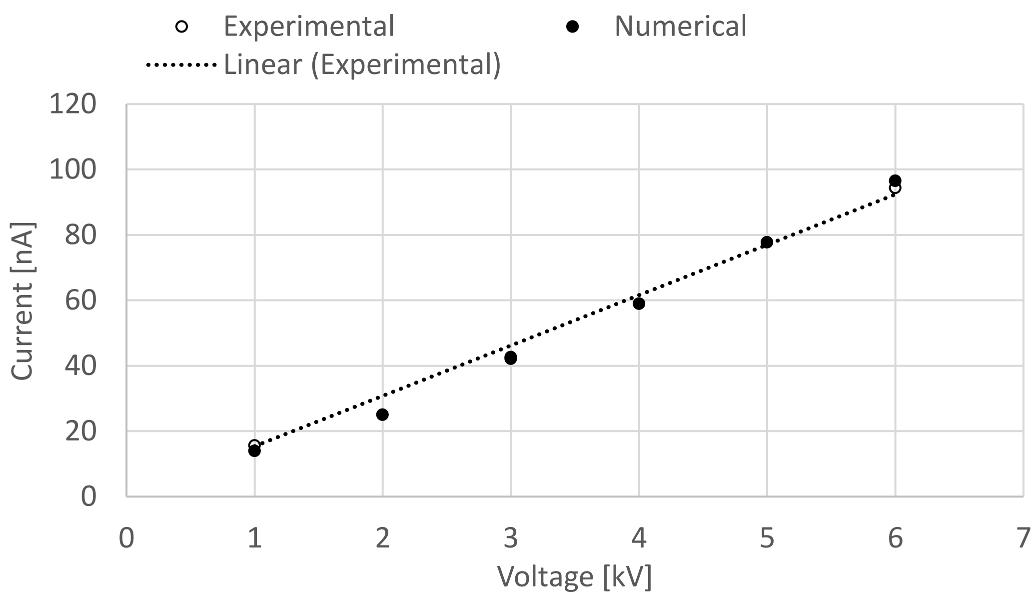

Figure 44: Current-voltage characteristics validation.

4.3.2 Numerical Results

In this section, the numerical results for the EHD melting problem are presented. Similar to the experimental procedure the non-EHD melting was simulated until a steady state condition was achieved, which was followed by the application of the EHD model to the system. The electrostatic results and the flow field are illustrated at different applied voltages and temperature gradients.

4.3.2.1 Effect of DC Voltages

Fig. 45 shows the electric field distribution at different applied voltages. The maximum electric field regions are observed in the vicinity of the high-voltage electrodes, with a gradient being detected above the top row of electrodes towards the top grounded surface and below the bottom row of electrodes towards the bottom grounded surface. In addition, a very low electric field region can also be observed in the middle area between the two rows of electrodes. The nonsymmetrical electric field distribution around each electrode can produce a resultant

Coulomb force, which is hypothesized to influence the intensity of the solid extraction. Moreover, the electric field increased alongside the voltage, with maximum electrical field values of 0.65, 1.3, and 2 MV/m being observed for the 2 kV, 4 kV, and 6 kV cases, respectively. Also, it can be seen that the electric field for the different cases are not identical due to the variation of the space charge density distribution.

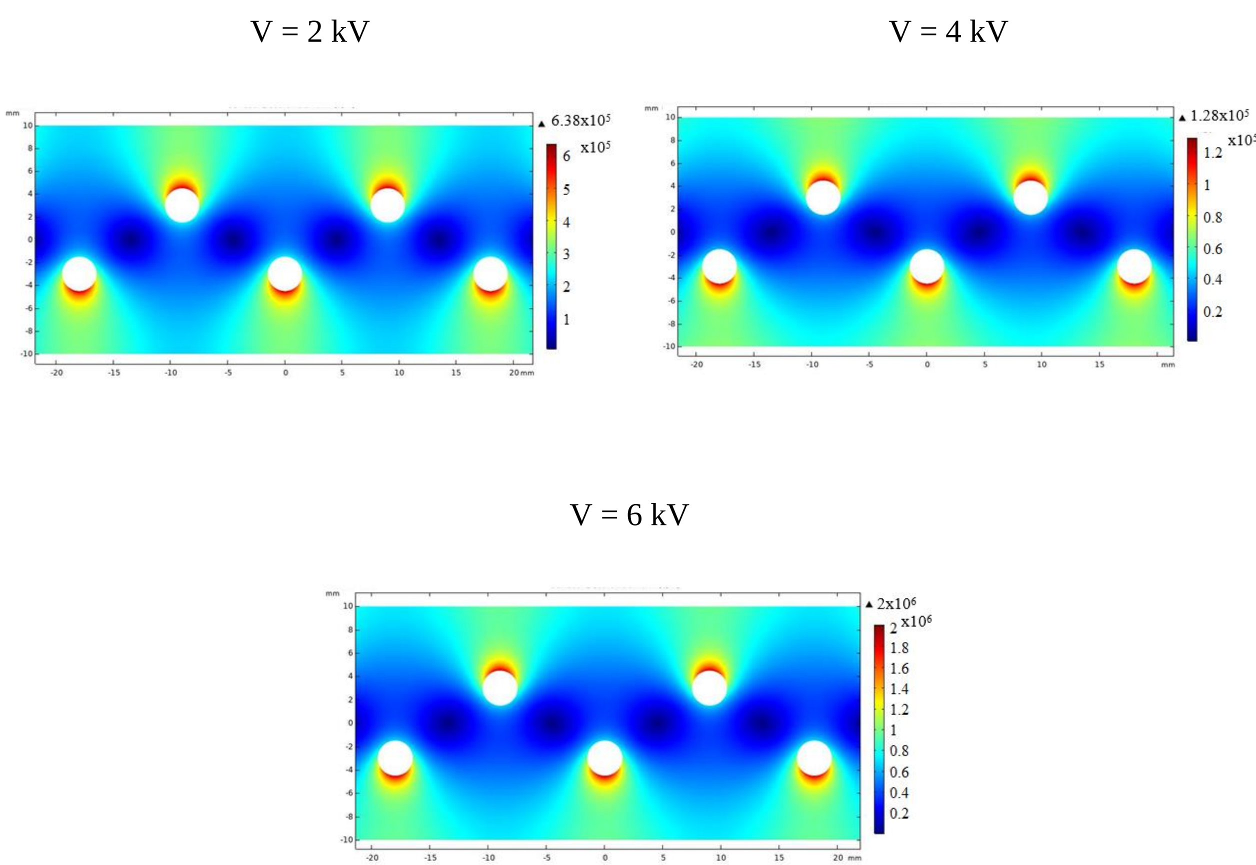

Figure 45: Electric field distribution at different voltages at t = 2 s [V/m].

The generation of the electric field in the dielectric medium will give rise to the formation of free charges at the surface of the electrodes due to the charge injection process. The results of the distribution of space-charge density at different applied voltages are shown in Fig. 46. The space charges in the vicinity of the electrodes increases with time and is observed to flow towards the counter electrodes at the top and bottom surfaces. After reaching the ground, the space charges start to discharge until a steady state condition is achieved after about 2 s, wherein the maximum space-charge density is found to be about 5.6 $*10^{-4}$ C/m^3 at 2 kV. A gradient of space charge is observed in the direction away from the electrodes, while a charge-void region is detected in the region between each two successive electrodes. With the increase in the applied voltage, the maximum space-charge density at the surface of the electrodes is slightly varied, while regions of high space-charge density are found to be larger due to the higher amount of free charges being injected into the dielectric medium at higher voltages.

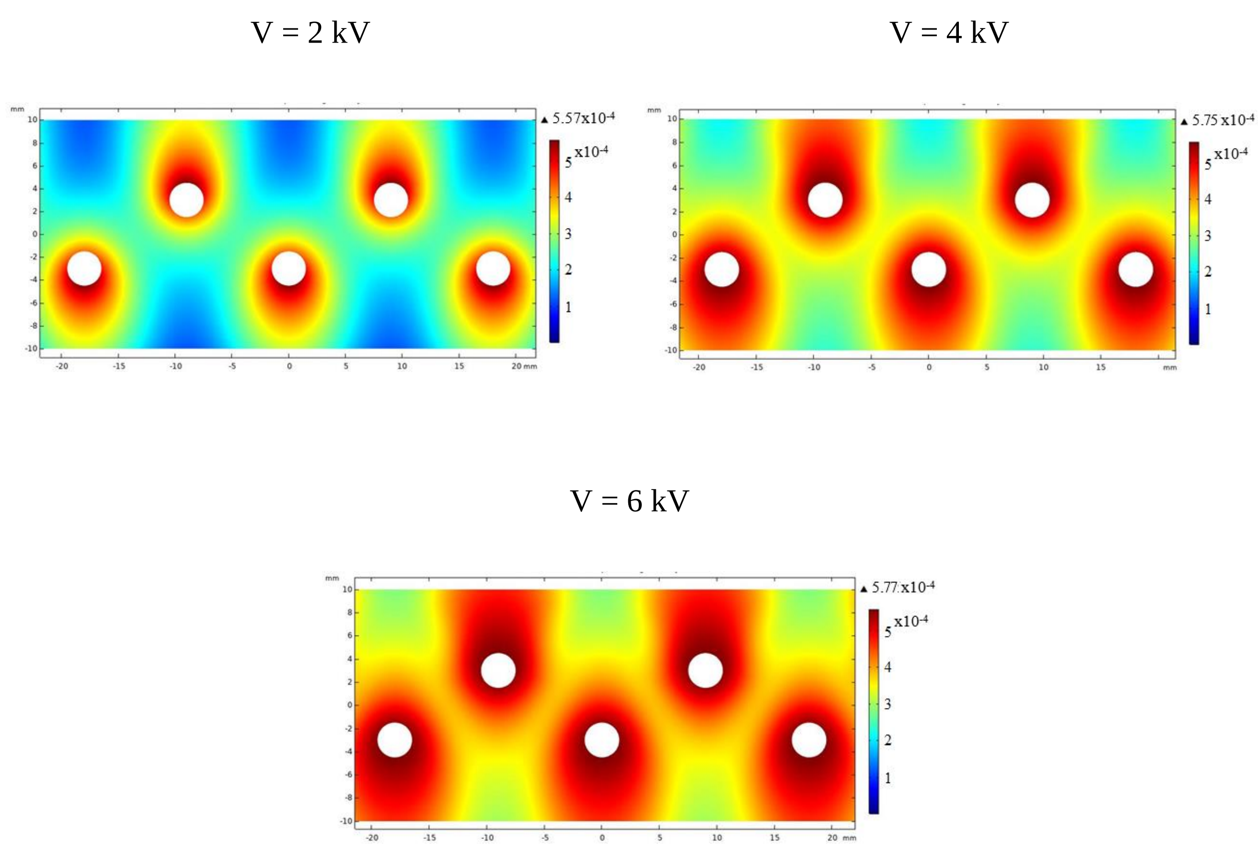

Figure 46: Space-charge density distribution at different voltages [C/m^3].

The free charges generated in the dielectric medium, along with the presence of the electric field, are responsible for creating the electrophoretic (Coulomb) EHD force in the bulk of the medium. Fig. 47 shows the distributions of the Coulomb force at different applied voltages. As can be seen, the Coulomb force is highest near the electrodes, where the electric field is also high, and diminishes with distance. In the middle region between the upper and lower rows of electrodes, the Coulomb force is very low due to the decline of the electric field in this area. The direction of the force followed the electric field lines and was always directed towards the ground electrodes (i.e., the force directed upwards above the top row and downwards below the bottom row of electrodes). As the voltage increased, the Coulomb force intensified in the bulk of the PCM, with maximum values of 0.33 kN/m^3, 0.74 kN/m^3, and 1.16 kN/m^3 being detected in the 2 kV, 4 kV, and 6 kV cases, respectively. This result was due to the increase in both the electric field and space charges in response to increases in the voltage. As the electrical body force in the liquid PCM comes into effect, an EHD flow is generated in the form of velocity cells due to the moment acting on the fluid. This EHD motion is influenced by two main body forces: the EHD Coulomb force and the buoyancy force. The Coulomb force produces torque on the fluid as it is confined between the boundary walls and the solid interface. The generated torque produces fluid vorticity leading to the creation of two electroconvection cells between each two successive electrodes (Fig. 48). However, the buoyancy force, which is produced by the temperature gradient across the liquid region, acts as a resisting force for the EHD flow. This oppositional behavior occurs because the buoyancy force produces a resisting torque which tends to move the cold fluid in the regions near the hot wall downward, while simultaneously pushing the hot fluid near the interface upward. As illustrated in Fig. 48, increasing the voltage significantly affected the EHD flow and the vorticity generated in the liquid bulk. The average fluid velocity was found to increase from 0.23 mm/s at 2 kV to 0.7 mm/s at 4 kV at an EHD time equal to 2 s. Similarly, further increasing the voltage to 6 kV resulted in an even higher average fluid velocity (about 1 mm/s). These results can be attributed to the increase in the body forces acting on the fluid as the voltage also increases. Additionally, the results revealed how the applied voltage primarily contributes to the increase in the heat transfer coefficient and, consequently, the increased melting rates reported by Hassan et al. [30].

V = 2 kV

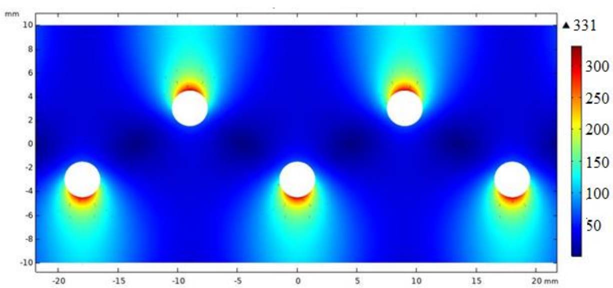

V = 4 kV

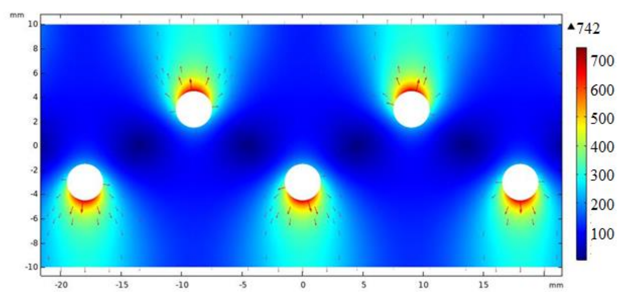

V = 6 kV

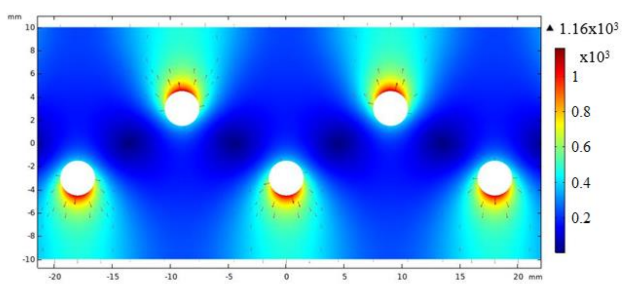

Figure 47: Coulomb force distribution at different applied voltages [N/m³].

(a) (b)

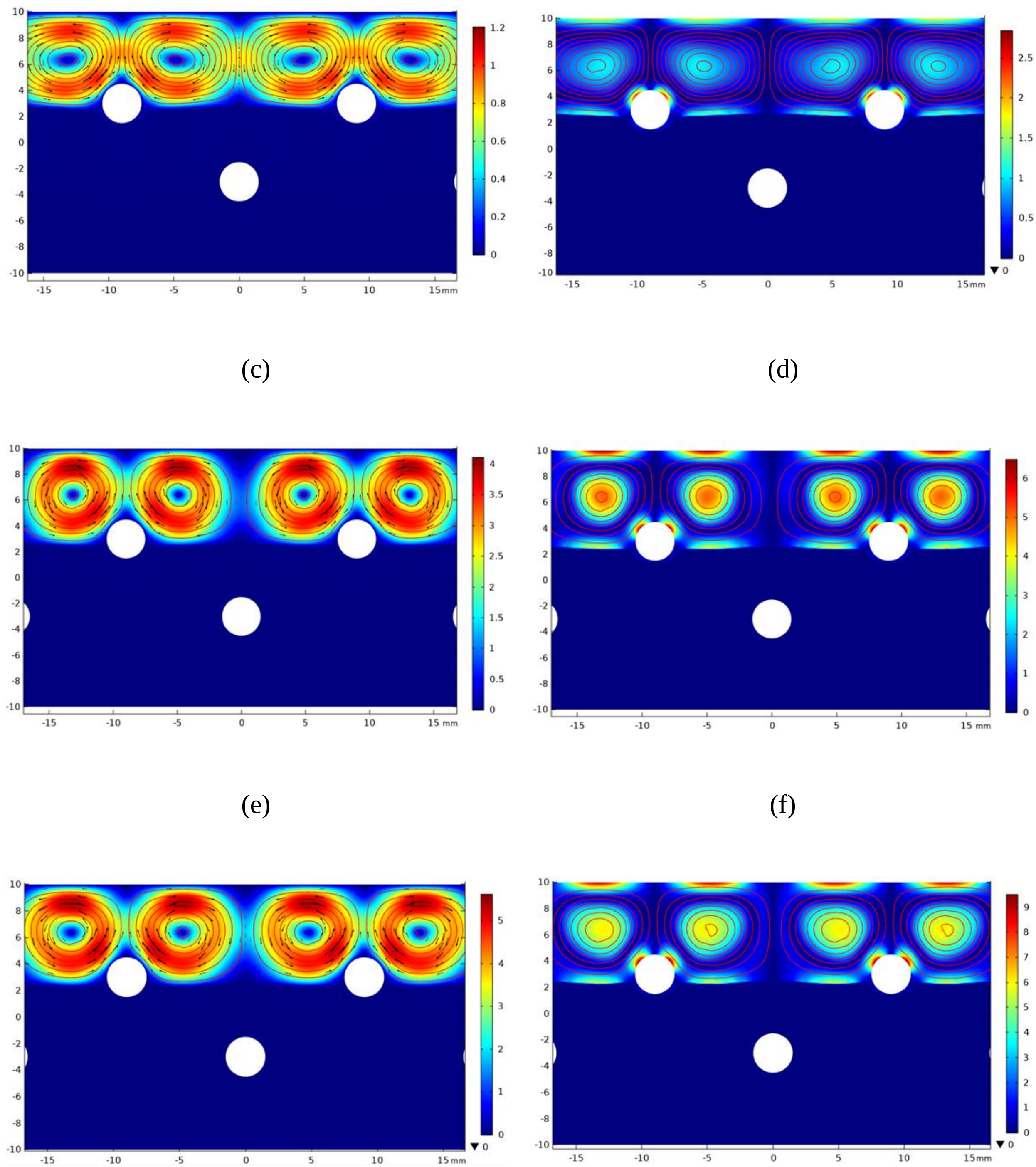

Figure 48: (a), (c), (e) Velocity field [mm/s] and streamlines for 2 kV, 4 kV, and 6 kV cases. (b), (d), (f) Vorticity field [1/s] for 2 kV, 4 kV, and 6 kV cases.

4.3.2.2 Effect of Temperature Gradient

The effect of temperature gradient across the liquid region was studied at different hot and cold temperatures for the top and bottom heat exchangers, where for case (a), T_h = 75 °C and T_c = 45 °C, and for case (b) T_h = 80 °C and T_c = 40 °C. First, the temperature gradient's impact on the buoyancy force was examined for the two cases (Fig. 49). As can be seen, the variations in the liquid density were higher at higher temperatures; thus, larger buoyancy forces were observed in the higher temperature cases. Next, the variation in the velocity of the EHD flow along the vertical plane was studied for the two cases at two horizontal positions, x = 0 and x = 9 mm, where x = 0 represented the midpoint between the two upper electrodes, and x = 9 mm represented the position corresponding to the electrode (Fig. 50). The results revealed that the velocity distribution had a bell-shaped curve, with zero divergence at the interface and top wall and maximum divergence in the middle. For the two horizontal positions, the velocities in the higher temperature cases were always higher than those in the lower temperature cases, where the maximum variation in the fluid velocity between the two cases was about 20%. This result was due to the higher buoyancy force associated with the high temperature case, where a resisting torque under the buoyancy effect is acting in an opposite direction to the torque produced by the Coulomb force, thereby reducing the fluid velocity.

Case (a) Case (b)

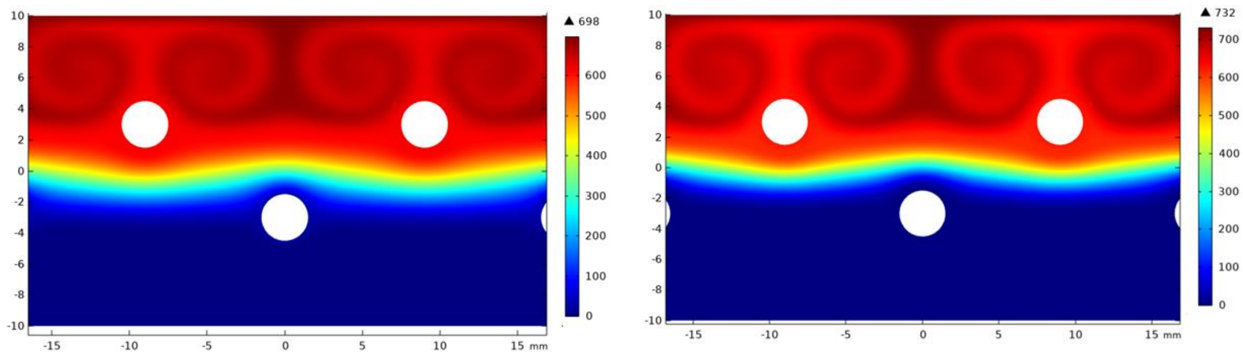

Figure 49: Buoyancy force distribution [N/m³] at different temperature gradients, (a) T_h = 75, T_c = 45 C, (b) T_h = 80, T_c = 40 C.

(a) (b)

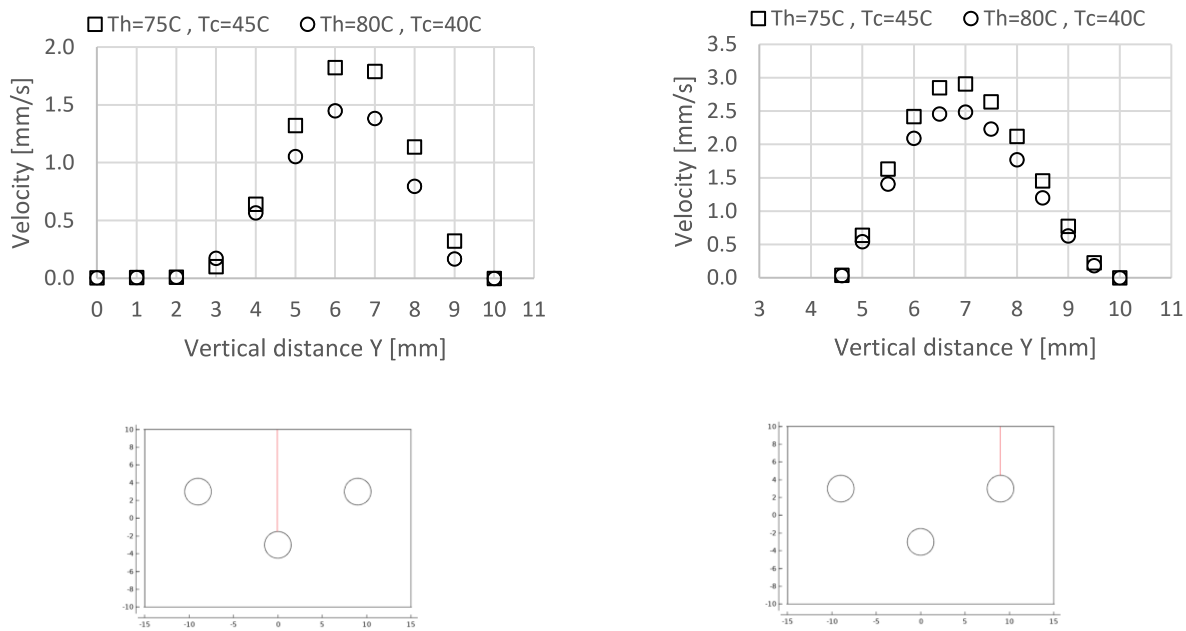

Figure 50: Velocity distribution at different temperature boundaries for two horizontal positions, (a) x= 0 and (b) x = 9 mm.

4.3.3 Experimental Results

4.3.3.1 Two-phase electric current measurements

The results of the electric current measurements for two-phase paraffin wax at different applied voltages are presented in Fig. 51. First, the PCM melted without EHD until a steady state condition had been achieved and the melting had stopped. At this point, the EHD was initiated, and the electric current was measured and recorded with time during the melting process. The EHD steady state electric current at different applied voltages was then determined and compared to the single-phase magnitudes (Fig. 51). The results revealed that the current-voltage characteristics for both cases had a linear relationship, with the current in the two-phase case being slightly higher than in the single-phase case. This difference can be attributed to the fact that, in the single-phase case, the top and bottom counter electrodes are exposed to the liquid PCM, whereas only the top electrode is in contact with the liquid in the two-phase case. Since the liquid has slightly higher mobility compared to solid PCM [34], [35], the electric current passing through it will be higher. The difference between the results was small, with a maximum variation in the electric current of about 10 nA which is within the experimental error of the current measurements.

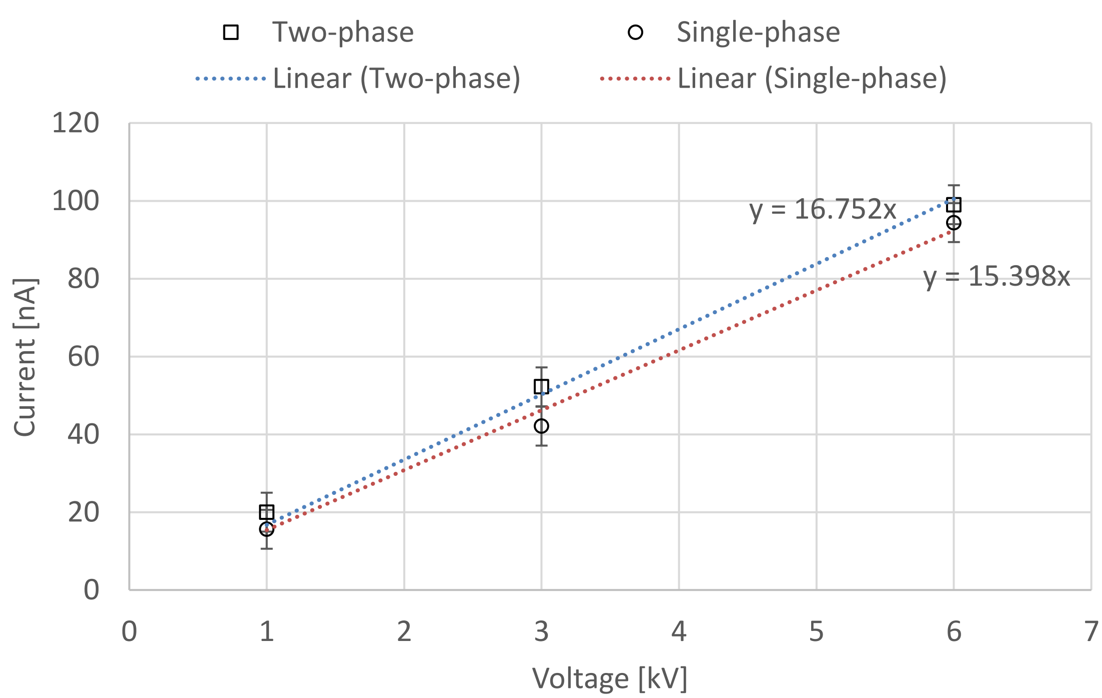

Figure 51: Electric current-voltage characteristics for two-phase system vs single-phase system.

4.3.3.2 Solid Extraction Characterization

High-speed imaging was employed to visualize solid extraction during the melting of paraffin wax under constant temperature boundary conditions. For these tests, the temperatures of the top and bottom heat exchangers were adjusted to 75 °C and 45 °C, respectively. Melting started to advance downwards until the melt front reached the first row of electrodes, at which point the EHD was applied at a DC voltage of 6 kV. High-speed imaging was initiated just after the start of the EHD and continued for 60 seconds. The visualization focused on the melt interface, which was located in the region between the electrodes in the middle of the test section. It was observed that solid extraction began once the EHD is applied, with very small solid particles being pulled upwards out of the mushy zone and into the liquid bulk. The images in Fig. 52 show the extracted dendrites near the melt interface at time intervals of 0.16 s between frames. As the images illustrate, the dendrites are nonsymmetrical in shape, being much longer than wide, with lengths ranging from 0.03 mm to 0.2 mm. These physical characteristics may be due to the particles being pulled strongly in one direction by the EHD forces. The variation in dendrite sizes depended on the position of the equiaxed grains in the mushy zone with respect to the interfacial forces, with higher EHD forces enabling the extraction of bigger dendrites. Furthermore, the intensity of the extraction was very high in regions near the electrodes on the right and left sides of the images due to the strong Coulomb force in the high-electric-field regions near the electrodes, as only few dendrites were observed being pulled from the center. After the dendrites are pulled out of the mushy region, they move upwards into the higher temperature regions where they melt. This behavior can be observed via the decrease in the dendrites' sizes in the upper regions compared to their sizes near the interface.

Solid extraction can result in higher melting rates, as the solid dendrites can melt faster as they move upwards in the liquid bulk. This outcome is the product of two factors: first, the liquid region is a higher temperature region resulting in faster melting, and second, the larger interfacial area of the extracted dendrites leads to higher heat transfer. In addition, the motion of the dendrites in the liquid medium can result in higher turbulence and, consequently, better electroconvection, which can increase the heat transfer coefficient in the liquid PCM. Nevertheless, the impact of turbulence in relation to the low velocities of dendrites may be minimal.

(a)

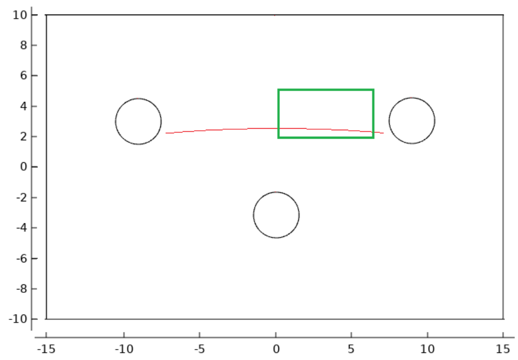

(b)

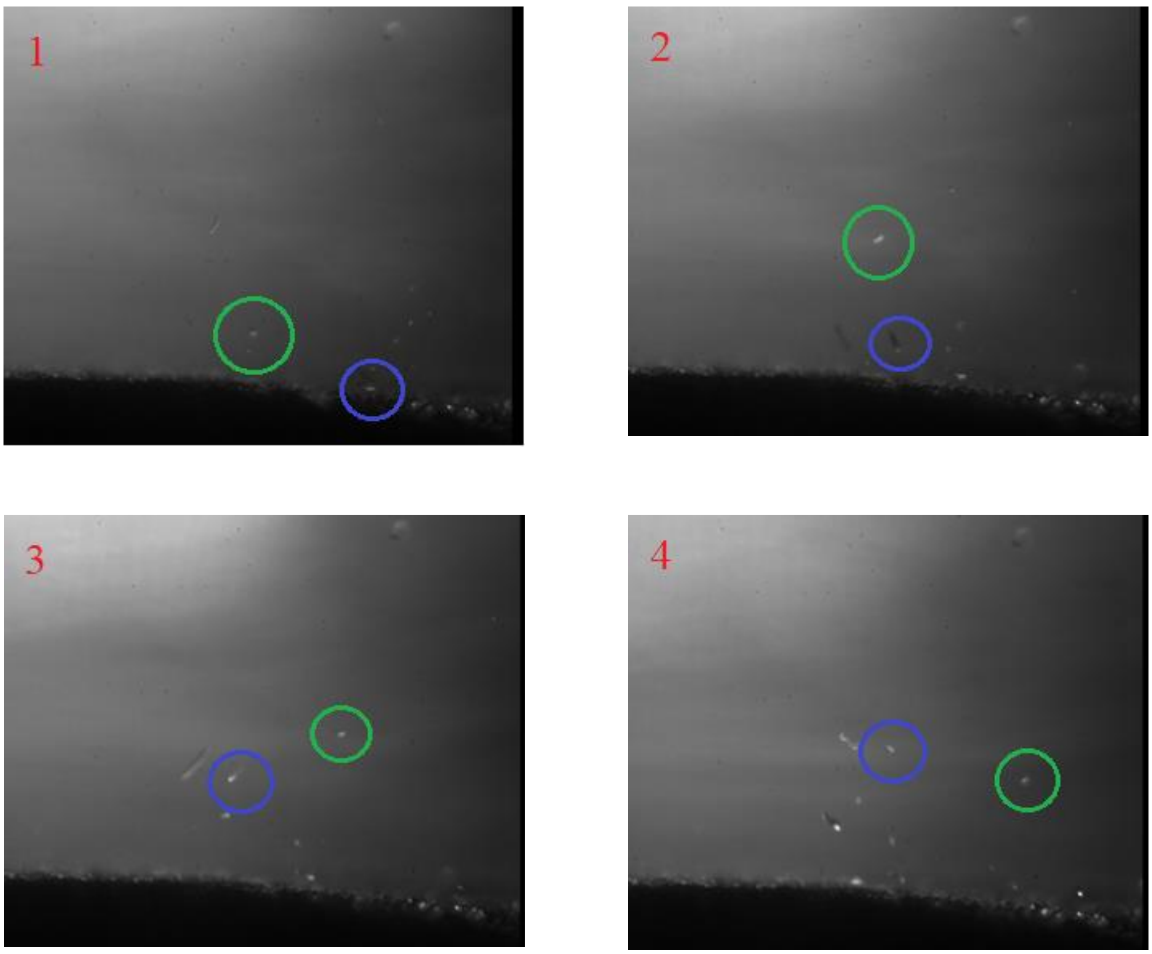

Figure 52: (a) Location of high-speed imaging, (b) High-speed images of solid extraction at 6 kV – time between frames is 0.32 s.

(a)

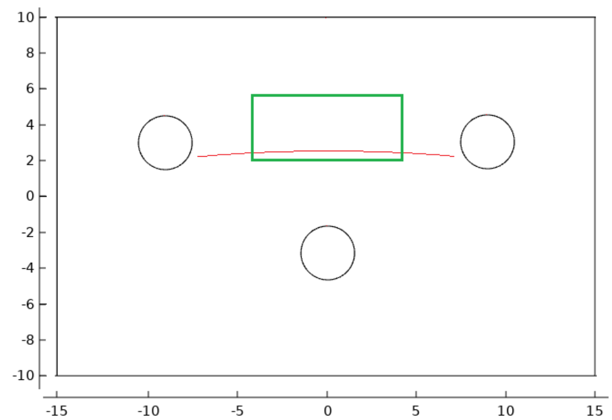

(b)

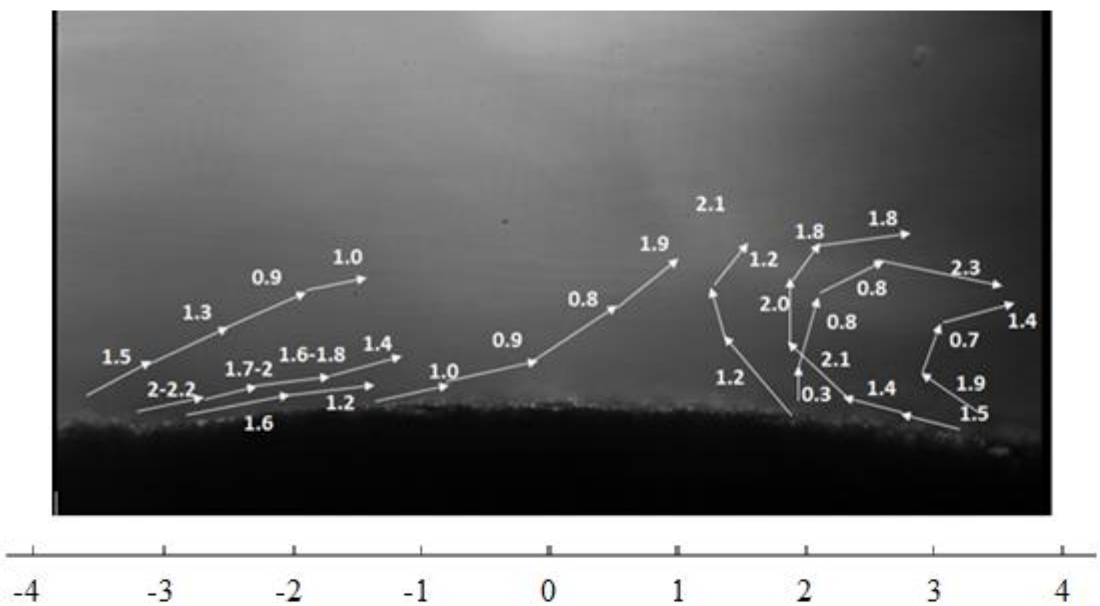

Figure 53: (a) Location of high-speed imaging, (b) Solid extraction velocity measurements at 6 kV [mm/s].

The velocity of the dendrites after extraction was measured at different locations as they moved upwards from the melt interface into the liquid volume (Fig. 53). Velocity measurements were conducted using FV4 software where the distance traveled by a single dendrite is tracked while moving between the recorded frames. Hence, the velocity can be determined by dividing the distance traveled by the time between frames. The arrows in the image indicate the direction of motion, and the number next to each arrow represents the velocity magnitude in mm/s. The velocity magnitudes ranged from 0.8 mm/s to 2.3 mm/s at 6 kV. It can be observed that the dendrite velocities decreased as they moved upwards due to being acted upon by different forces during extraction. At the interface, the dendrites are pulled out from the mushy region and then move upwards under the action of the interfacial forces. Since the Coulomb force is the main contributing force of solid extraction [30], the velocity magnitudes will be higher in regions with high Coulomb force, which are located close to the electrodes and near the melt interface. As the dendrites move away from the interface, their velocities decrease due to the corresponding decrease in the Coulomb force. Furthermore, it was observed that the dendrites typically moved from the areas near the electrodes (at the right and left of the image) towards the center. This pattern of motion can be attributed to the Coulomb force, which can direct the dendrites from the high-electric-field regions to the lower-electric-field regions in the middle area between the electrodes. In some cases, the dendrites changed their direction of motion in response to an increase in velocity magnitude, likely as a result of the influence of the electroconvection cells in the liquid bulk. When the small solid particles advance into the velocity roll's zone of action, they tend to flow along the streamlines and take on the same velocity magnitudes. Next, different DC voltages were tested to examine how they impacted the velocity and size of the extracted dendrites. Fig. 54 shows the variation in the average velocity of the dendrites calculated at different horizontal locations with respect to the electrodes, where x=0 represents the location at the middle between the electrodes (refer to Fig. 53). As can be seen, the velocity of the dendrites increases as x increases, indicating that the dendrites extracted closer to the electrodes are influenced by larger EHD forces. Furthermore, it can also be observed that the dendrites can acquire higher velocity magnitudes as the voltage increases, as the increased electric field due to higher voltage leads to higher Coulomb forces and, consequently, stronger electroconvection. The maximum velocities detected for the 3 kV, 6 kV, and 9 kV cases were 1.6 mm/s, 3.5 mm/s, and 6 mm/s, respectively.

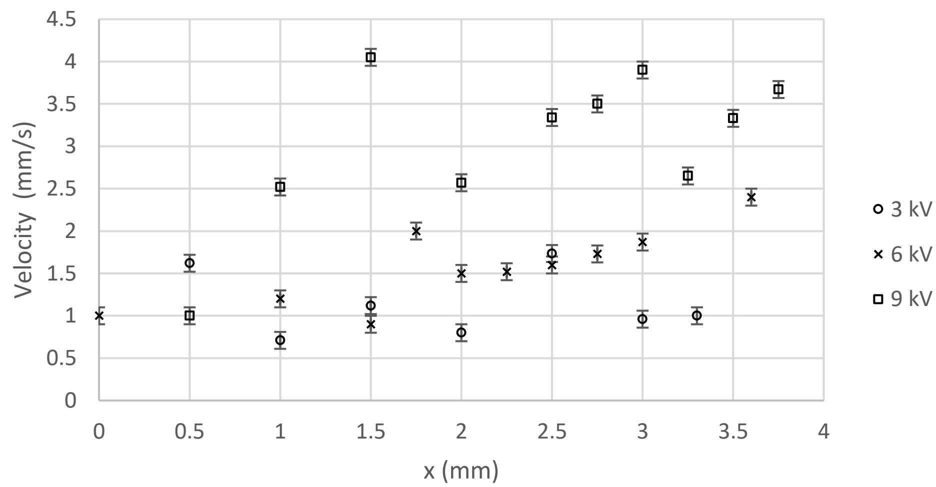

Figure 54: Variation in solid extraction velocity along the horizontal axis at different applied voltages.

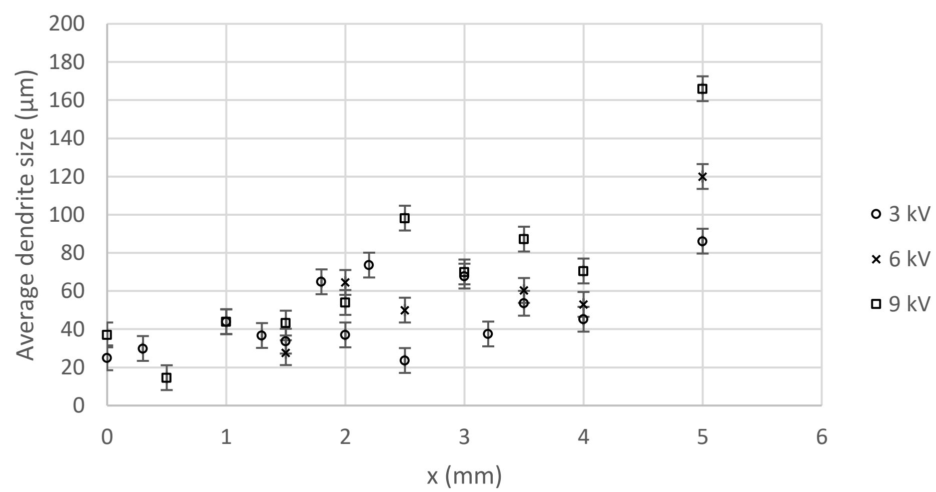

Figure 55: Variation in dendrite size along the horizontal axis at different applied voltages.

The length and width of each dendrite was measured near the melt interface just after extraction, and the average size was calculated and plotted against the horizontal location (Fig. 55). The results revealed that the dendrites' sizes exhibited a similar trend to the velocity results, namely, the dendrites were relatively small in the middle region between the electrodes (x=0) and grew in size as x increased and they got closer to the electrodes. This phenomenon was due to the higher extraction (Coulomb) force in the vicinity of the electrodes, which led to larger solid particles being pulled out of the mushy zone. Additionally, the extraction of larger dendrites was observed as the voltage was increased, with maximum dendrite sizes of 0.16 mm, 0.2 mm, and 0.5 mm being recorded for the 3 kV, 6 kV, and 9 kV cases, respectively. This result was due to the increase in interfacial forces brought about by the increase in voltage. The intensity of the solid extraction was also studied at different applied voltages by recording the number of dendrites pulled out of the mushy zone from the start of EHD to 60 seconds after EHD. Each experiment was repeated several times to examine the repeatability of the solid extraction. Solid extraction was observed during the application of EHD in all experiments, which shows that this mechanism is repeatable. The results for the solid extraction intensity tests at different DC voltages are presented in Fig. 56. As can be seen, the lowest intensity was observed at 3 kV, where the number of extracted dendrites in the different repeatability experiments varied from 20 to 50 in the first 60 seconds. Increasing the voltage to 6 kV resulted in a significantly higher intensity, with the number of dendrites ranging from 70 to 150; this result indicates that, at higher voltages, the interfacial forces get stronger, and thus, more dendrites can be extracted. Increasing the voltage to 9 kV did not yield any significant increase in solid extraction intensity above the 6 kV condition, with a maximum number of about 155 dendrites being extracted. The high range of intensities observed within the repeatability experiments can be attributed to the randomness of the PCM grain structure during solidification after each experiment, as this lack of uniformity can result in different mushy zone structures during the melting process in the next experiment.

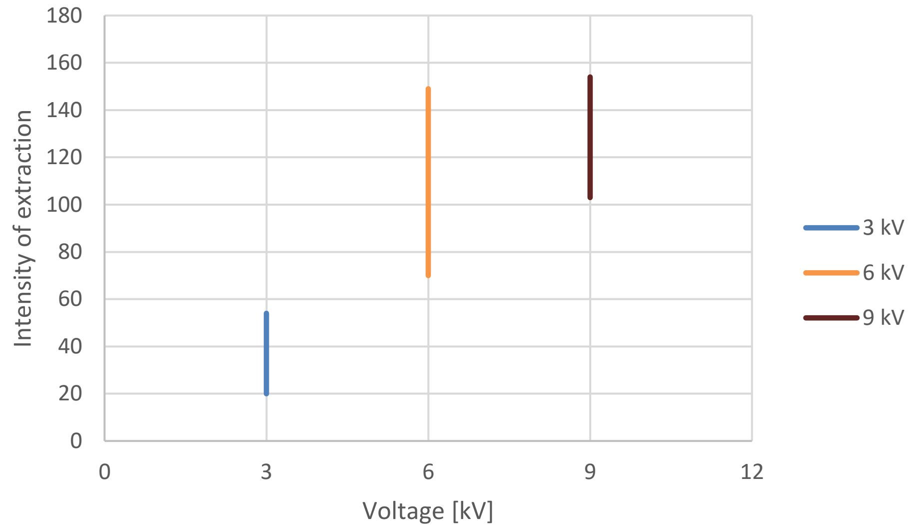

Figure 56: Intensity of solid extraction at different applied voltages.

The effect of temperature gradients on dendrite velocity was investigated by melting paraffin wax under an applied voltage of 6 kV and at two different top heat exchanger temperatures (80 °C and 75 °C) with the same temperature for the bottom heat exchanger (45 °C). Fig. 57 shows the results of the velocity measurements for different extracted dendrites at different locations with respect to the electrodes. Overall, the velocities of the dendrites just after extraction were slightly lower for the T_h = 80 °C case than for the T_h = 75 °C case. After extraction, the dendrites tended to move upwards towards the low-electric-field region in the middle area between the electrodes. For the high-temperature case, the dendrites moved upward with a lower slope—and thus, did not reach the higher regions of the liquid bulk—while in the lower-temperature case they moved higher in the liquid with a slightly higher velocity. The average velocity magnitudes measured for the low- and high-temperature cases were 1.6 mm/s and 1.25 mm/s, respectively. These results revealed that the velocity of the extracted dendrites is influenced by the temperature gradient across the liquid region; that is, the buoyancy force in the liquid PCM becomes greater at higher temperature gradients, consequently subjecting the dendrites to higher forces of resistance as they move upwards through the liquid, thus resulting in lower velocities and lower slopes for the upward direction of motion.

Finally, solid extraction was investigated with different PCMs having different melting temperature ranges to study the influence of the size of the mushy zone. Table 8 shows the different tested PCMs, their melting temperatures, and the solid extraction results. All the experiments were performed using an applied voltage of 6 kV and the same temperature boundaries for the upper and lower heat exchangers (i.e., T_h = 75 °C and T_c = 45 °C). Compared to the other PCMs, the intensity of the solid extraction for paraffin was relatively high, with a minimum intensity of 70 being observed for all experiments. Conversely, RT31 had a very low solid extraction intensity, with a maximum of 10 dendrites being detected, while no extraction was observed for n-octadecane in any of the experiments. These results support the conclusion that solid extraction is influenced by the presence of a mushy zone, as n-octadecane is considered a pure material with no mushy zone. In the case of RT31, which possesses a mushy zone, solid extraction becomes evident with very low intensity due to the materials small mushy thickness, whereas paraffin wax exhibited high solid extraction intensity due to the high thickness of its mushy zone, and therefore, its high melting temperature range.

(a)

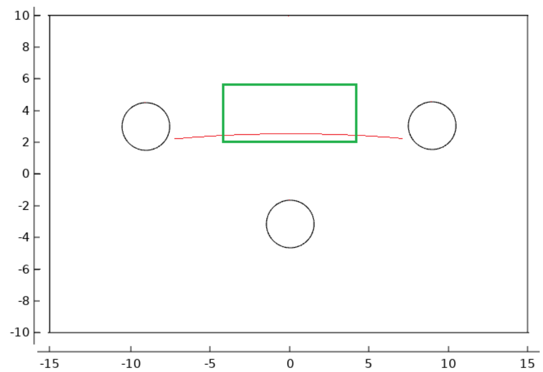

(b)

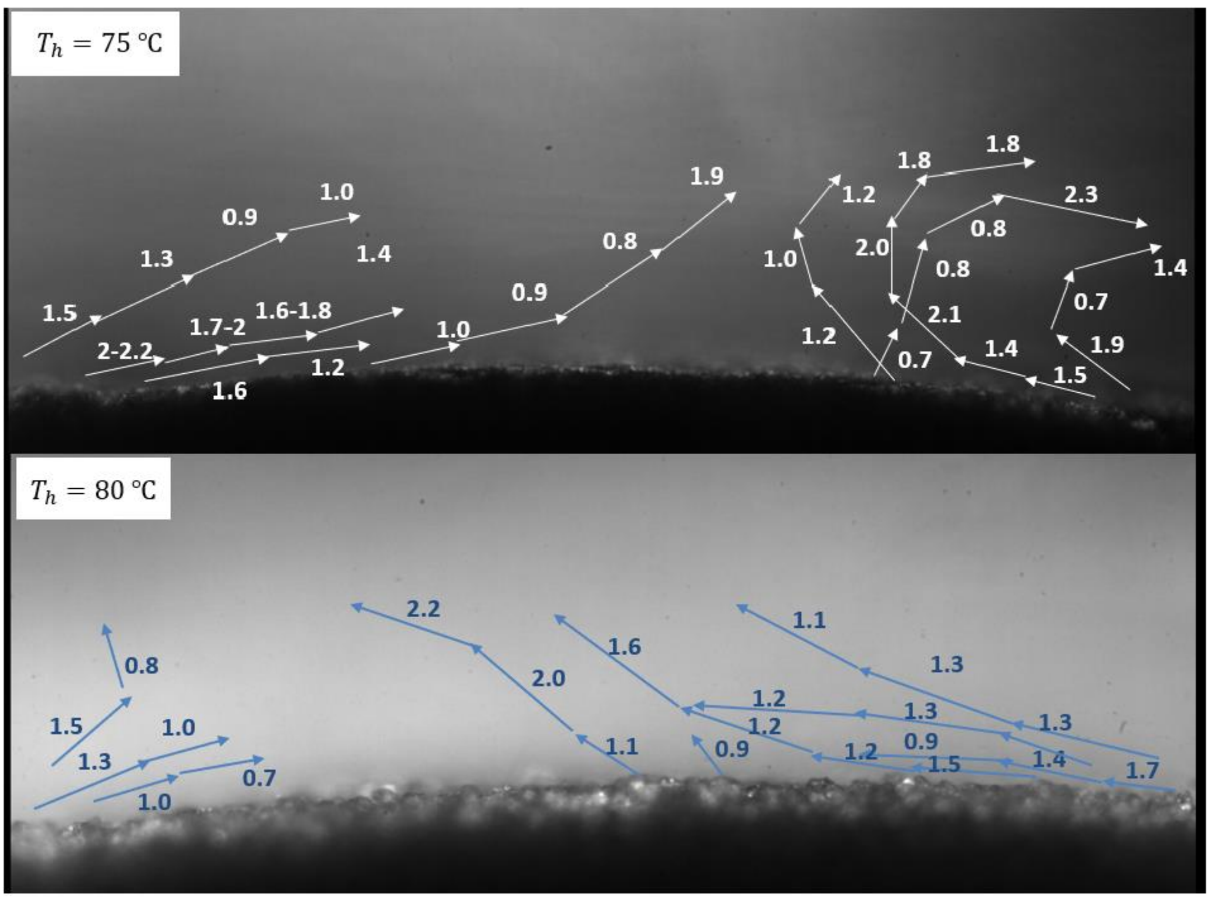

Figure 57: (a) Location of high-speed imaging, (b) Velocity measurements for the extracted dendrites at different temperature gradients at 6 kV.

Table 8: Solid extraction intensity for different PCMs.

	Melting temperatures	**Solid extraction intensity**
Paraffin wax	63 °C – 53 °C	> 70
RT31	29 °C – 31 °C	5 – 10
n-Octadecane	28 °C	No extraction

4.3.4 Comparison of Experimental and Numerical Results

A comparison of the numerical results for the EHD fluid velocity tests (the black arrow lines representing the direction of flow) and the experimental results for solid extraction velocity tests is presented in Fig. 58. The white arrow lines in Fig. 58a represent the direction of motion of the extracted dendrites, while the velocity magnitudes for the dendrites are shown in Fig. 58b. As can be seen, the extracted dendrites move opposite to the flow direction at locations near the interface where the fluid velocity is very low (below 1 mm/s). In this region, the dendrites move under the action of the charge injection, represented by the Coulomb force, which pulls the solid particles out from the mushy zone and pushes them upwards through the liquid bulk. Additionally, a dielectrophoretic force acts on the extracted dendrites, subjecting the suspended solid particles in the liquid PCM to a polarizing force that pulls them towards high electric field regions [36]. This is due to the induced charges that accumulate on the solid particle (the higher permittivity medium) with a non-uniform distribution which produces a positive electric dipole moment that acts along the electric field lines. However, because the Coulomb force is dominant, the dendrites continue to move upwards until they reach the higher-velocity regions within the electroconvection cells. At this point, the dendrites change direction and move along the streamlines of the velocity field and in the same direction as the convection cells. The velocity magnitudes of the deflected dendrites were in the range of 2 mm/s, which is comparable to the numerical velocity magnitudes at the same locations.

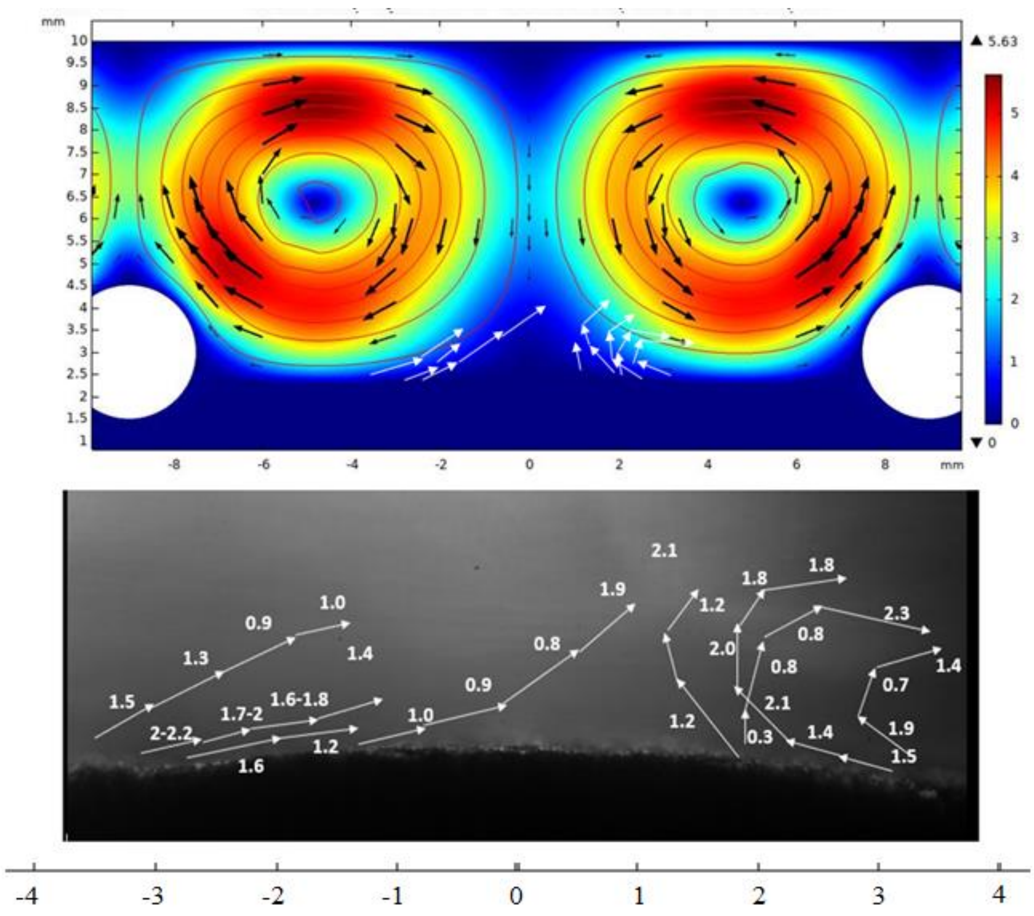

Figure 58: Comparison of the numerical results for the velocity distribution tests and experimental results for the solid extraction dendrite velocity tests at 6 kV.

4.4 Conclusions

In this paper, charge injection was numerically modelled to investigate electroconvection flow during the melting of phase-change materials under constant temperature boundary conditions. The coupled set of governing equations—including the electrostatic field, the space-charge density, the flow field, and the temperature field—were solved using a finite element method and COMSOL Multiphysics software. Furthermore, solid extraction was experimentally investigated via the melting of different phase-change materials under various applied voltages and temperature boundaries.

The numerical results indicated that the electric field and, consequently, the space-charge density increased alongside the applied voltage, resulting in increased Coulomb force within the dielectric medium. The results also indicated that the magnitudes of the Coulomb force were very high in the vicinity of the electrodes and decreased towards the top and bottom grounded surfaces. In addition, it was shown that the presence of electrical body forces in the liquid phase-change material generate two electroconvection cells between each two electrodes, and that the EHD flow velocity increases alongside the voltage due to an increase in the Coulomb force. Increasing the temperature gradients across the liquid phase-change material results in higher buoyancy effects, which decreases the fluid velocity.

The experimental results confirmed that solid extraction occurs at high intensities during the melting of paraffin wax, with solid dendrites being pulled upwards from the mushy zone into the liquid bulk at higher velocities than the EHD convection cells in their vicinity. The results further showed that the intensity of the extraction, along with the velocity and size of the dendrites, was highest in areas nearest the electrodes and decreased with closeness to the center-point between each two electrodes. In addition, it was observed that increasing the applied voltage resulted in higher extraction intensities and higher velocities for the extracted dendrites. This finding revealed that the Coulomb force can be hypothesized to be the dominant mechanism influencing solid extraction in the current study. As expected lower dendrite velocities were observed at higher temperature gradients due to the increase in the buoyancy force. Solid extraction investigations using different phase-change materials showed that RT31, which has a lower mush zone thickness, had a much lower extraction intensity compared to paraffin was, while no solid extraction was detected for n-octadecane. These results confirm the influence of mushy zone thickness on solid extraction.

Acknowledgements

This project was partly supported by the Natural Sciences and Engineering Research Council of Canada (RGPIN/355844). We would like to acknowledge CMC Microsystems for the provision of COMSOL that facilitated this research.

Keywords

Electrohydrodynamics - Charge injection - Coulomb force - Phase-change materials – Convection cells – Solid extraction.

4.5 Appendix B

In the current study, the permittivity of the material was assumed homogeneous for the whole domain during the melting process. This assumption was used due to the very low permittivity difference between the solid and the liquid for the paraffin wax, where ε_liquid=2.1 and ε_solid=2.3. In this section, the effect of varying the permittivity between the solid and liquid region for the 6 kV case is presented. The numerical modeling of the mushy region can be represented by equation A1.

$$\varepsilon = \gamma\varepsilon_{\mathrm{liquid}} + (1-\gamma)\varepsilon_{solid} \tag{B1}$$

The electric field distribution at t = 2 s is shown in Fig. B1. The variation in permittivity across the mushy region did not show any significant change in the electric field distribution, where the melt interface cannot be identified. This can be attributed to the very low gradient of permittivity due to the thick mushy zone for the domain material. Accordingly, the electroconvection flow was not influenced by the change in permittivity as presented in Fig. B2. The average fluid velocity was about 1.08 mm/s which differs from the average velocity for the homogeneous permittivity case by less than 4%. These results validate the assumption of homogenous permittivity used in the current study.

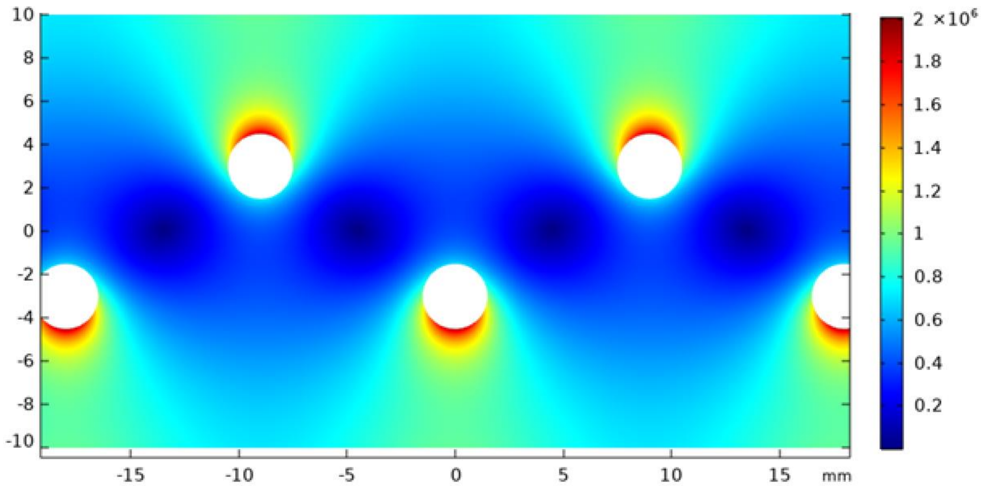

Figure B1: Electric field distribution at 6 kV [V/m]

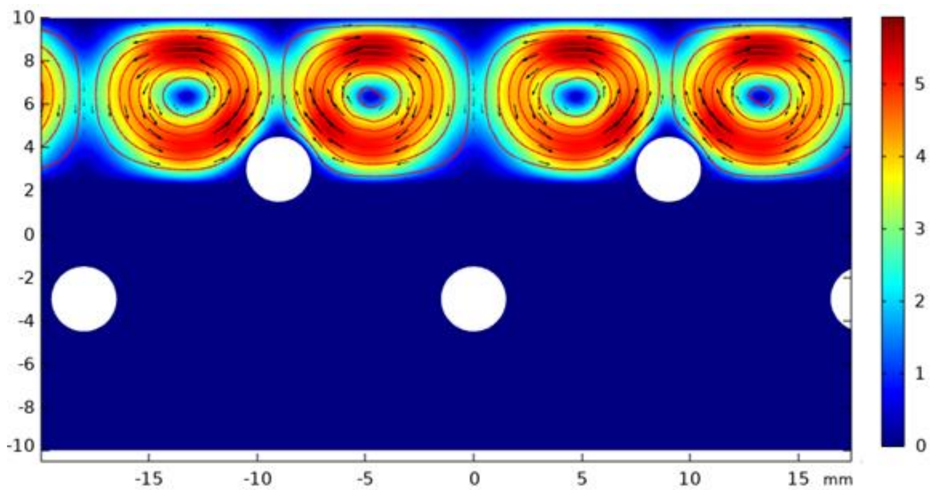

Figure B2: Velocity field at 6 kV [mm/s]

4.6 References

[1] S. Rashidi, H. Bafekr, R. Masoodi, and E. M. Languri, "EHD in thermal energy systems - A review of the applications, modelling, and experiments," *J. Electrostat.*, vol. 90, pp. 1–14, 2017, doi: 10.1016/j.elstat.2017.08.008.

[2] B. Chu, "No Title," *Phys. Fluids*, vol. 2.5, pp. 473–484, 1959.

[3] D. V. Fernandes, H. D. Lee, S. Alapati, and Y. K. Suh, "Numerical simulation of the electro-convective onset and complex flows of dielectric liquid in an annulus," *J. Mech.*

Sci. Technol., vol. 26, no. 12, pp. 3785–3793, 2012, doi: 10.1007/s12206-012-1005-3.

[4] J. L. Fernández and R. Poulter, "Radial mass flow in electrohydrodynamically-enhanced forced heat transfer in tubes," *Int. J. Heat Mass Transf.*, vol. 30, no. 10, pp. 2125–2136, 1987, doi: 10.1016/0017-9310(87)90091-3.

[5] D. Nakhla, H. Sadek, and J. S. Cotton, "Melting performance enhancement in latent heat storage module using solid extraction electrohydrodynamics (EHD)," *Int. J. Heat Mass Transf.*, vol. 81, pp. 695–704, 2015, doi: 10.1016/j.ijheatmasstransfer.2014.10.016.

[6] M. Daaboul, C. Louste, and H. Romat, "Electrohydrodynamical characteristics of a dielectric liquid flow induced by charge injection," *2008 IEEE Int. Conf. Dielectr. Liq. ICDL 2008*, pp. 37–40, 2008, doi: 10.1109/ICDL.2008.4622532.

[7] M. Daaboul, P. Traoré, P. Vázquez, and C. Louste, "Study of the transition from conduction to injection in an electrohydrodynamic flow in blade-plane geometry," *J. Electrostat.*, vol. 88, pp. 71–75, 2017, doi: 10.1016/j.elstat.2017.01.014.

[8] C. Louste, H. Romat, P. Traore, M. Daaboul, P. Vazquez, and R. Sosa, "Electroconvective Cavity Flow Patterns Created by Asymmetric Electrode Configuration," *IEEE Trans. Ind. Appl.*, vol. 54, no. 5, pp. 4851–4856, 2018, doi: 10.1109/TIA.2018.2843797.

[9] Z. Sun, D. Sun, J. Hu, P. Traoré, H. L. Yi, and J. Wu, "Experimental study on electrohydrodynamic flows of a dielectric liquid in a needle-plate configuration under direct/alternating current electric field," *J. Electrostat.*, vol. 106, no. October 2019, 2020, doi: 10.1016/j.elstat.2020.103454.

[10] Z. Sun, P. Yang, K. Luo, and J. Wu, "Experimental investigation on the melting characteristics of n-octadecane with electric field inside macrocapsule," *Int. J. Heat Mass*

Transf., vol. 173, p. 121238, 2021, doi: 10.1016/j.ijheatmasstransfer.2021.121238.

[11] Z. Sun, Y. Zhang, K. Luo, A. T. Pérez, H. Yi, and J. Wu, "Experimental investigation on melting heat transfer of an organic material under electric field," *Exp. Therm. Fluid Sci.*, vol. 131, no. October 2021, 2022, doi: 10.1016/j.expthermflusci.2021.110530.

[12] D. Nakhla and J. S. Cotton, "Effect of electrohydrodynamic (EHD) forces on charging of a vertical latent heat thermal storage module filled with octadecane," *Int. J. Heat Mass Transf.*, vol. 167, p. 120828, 2021, doi: 10.1016/j.ijheatmasstransfer.2020.120828.

[13] P. A. Vázquez, G. E. Georghiou, and A. Castellanos, "Numerical analysis of the stability of the electrohydrodynamic (EHD) electroconvection between two plates," *J. Phys. D. Appl. Phys.*, vol. 41, no. 17, 2008, doi: 10.1088/0022-3727/41/17/175303.

[14] P. Traoré and A. T. Pérez, "Two-dimensional numerical analysis of electroconvection in a dielectric liquid subjected to strong unipolar injection," *Phys. Fluids*, vol. 24, no. 3, 2012, doi: 10.1063/1.3685721.

[15] K. Dantchi, T. Philippe, and R. Hubert, "Numerical study of the heat transfer and electro-thermo-convective flow patterns in dielectric liquid layer subjected to unipolar injection," *J. Electrostat.*, vol. 71, no. 6, pp. 970–975, 2013, doi: 10.1016/j.elstat.2013.09.003.

[16] T. F. Li, Z. G. Su, K. Luo, and H. L. Yi, "Transition to chaos in electro-thermo-convection of a dielectric liquid in a square cavity," *Phys. Fluids*, vol. 32, no. 1, 2020, doi: 10.1063/1.5126007.

[17] J. Wu, P. Traoré, C. Louste, L. Dascalescu, F. B. Tian, and A. T. Pérez, "Effect of the mobility parameter on the oscillatory electroconvection of dielectric liquids subject to strong unipolar charge injection," *IEEE Trans. Ind. Appl.*, vol. 50, no. 4, pp. 2306–2313,

2014, doi: 10.1109/TIA.2014.2301872.

[18] J. Wu, P. A. Vázquez, P. Traoré, and A. T. Pérez, "Finite amplitude electroconvection induced by strong unipolar injection between two coaxial cylinders," *Phys. Fluids*, vol. 26, no. 12, 2014, doi: 10.1063/1.4903284.

[19] W. Hassen, M. I. Elkhazen, P. Traore, and M. N. Borjini, "Numerical study of the electro-thermo-convection in an annular dielectric layer subjected to a partial unipolar injection," *Int. J. Heat Fluid Flow*, vol. 50, pp. 201–208, 2014, doi: 10.1016/j.ijheatfluidflow.2014.08.003.

[20] J. Wu, A. T. Pérez, P. Traoré, and P. A. Vázquez, "Complex flow patterns at the onset of annular electroconvection in a dielectric liquid subjected to an arbitrary unipolar injection," *IEEE Trans. Dielectr. Electr. Insul.*, vol. 22, no. 5, pp. 2637–2645, 2015, doi: 10.1109/TDEI.2015.005157.

[21] J. Huang, R. D. Selvakumar, Y. Guan, H. Li, P. Traoré, and J. Wu, "Numerical investigation of injection-induced electro-convection in a dielectric liquid between two eccentric cylinders," *Int. J. Heat Fluid Flow*, vol. 83, no. March, p. 108594, 2020, doi: 10.1016/j.ijheatfluidflow.2020.108594.

[22] R. D. Selvakumar, L. Qiang, L. Kang, P. Traoré, and J. Wu, "Numerical modeling of solid-liquid phase change under the influence an external electric field," *Int. J. Multiph. Flow*, vol. 136, p. 103550, 2021, doi: 10.1016/j.ijmultiphaseflow.2020.103550.

[23] K. Luo, A. T. Pérez, J. Wu, H. L. Yi, and H. P. Tan, "Efficient lattice Boltzmann method for electrohydrodynamic solid-liquid phase change," *Phys. Rev. E*, vol. 100, no. 1, pp. 1–15, 2019, doi: 10.1103/PhysRevE.100.013306.

[24] K. He, Z. Chai, L. Wang, B. Ma, and B. Shi, "Numerical investigation of electro-thermo-convection with a solid-liquid interface via the lattice Boltzmann method," *Phys. Fluids*, vol. 33, no. 3, 2021, doi: 10.1063/5.0041574.

[25] C. L. Lu, X. L. Gao, J. Wu, K. Luo, and H. L. Yi, "Heat transfer enhancement analysis of electrohydrodynamic solid-liquid phase change via lattice Boltzmann method," *Appl. Therm. Eng.*, vol. 194, no. November 2020, p. 117112, 2021, doi: 10.1016/j.applthermaleng.2021.117112.

[26] R. D. Selvakumar and S. Vengadesan, "Combined effects of buoyancy and electric forces on non-isothermal melting of a dielectric phase change material," *Int. J. Multiph. Flow*, vol. 151, no. December 2021, 2022, doi: 10.1016/j.ijmultiphaseflow.2022.104029.

[27] K. He, B. Ma, and L. Wang, "Electrohydrodynamic enhancement of phase change material melting in cylindrical annuli under microgravity," *Appl. Therm. Eng.*, vol. 215, no. June, p. 119005, 2022, doi: 10.1016/j.applthermaleng.2022.119005.

[28] R. D. Selvakumar, J. Wu, I. Afgan, Y. Ding, and A. K. Alkaabi, "Melting performance enhancement in a thermal energy storage unit using active vortex generation by electric field," *J. Energy Storage*, vol. 67, no. February, p. 107593, 2023, doi: 10.1016/j.est.2023.107593.

[29] D. Nakhla, E. Thompson, B. Lacroix, and J. S. Cotton, "Measurement of heat transfer enhancement in melting of n-Octadecane under gravitational and electrohydrodynamics (EHD) forces," *J. Electrostat.*, vol. 92, no. January, pp. 31–37, 2018, doi: 10.1016/j.elstat.2018.01.004.

[30] A. Hassan and J. S. Cotton, "Investigation of the role of electrohydrodynamic forces on

the heat transfer enhancement and solid extraction during melting of paraffin wax under constant temperature boundary conditions,” *Int. J. Heat Mass Transf.*, vol. 204, 2023, doi: 10.1016/j.ijheatmasstransfer.2022.123831.

[31] M. S. Zadeh, “Measurement of ion mobility in dielectric liquids,” no. 66, 2011.

[32] A. Gazaryan, A. Sitnikov, V. Chirkov, and Y. Stishkov, “A Method for Estimation of Functional Dependence of Injection Charge Formation on Electric Field Strength,” *IEEE Trans. Ind. Appl.*, vol. 53, no. 4, pp. 3977–3981, 2017, doi: 10.1109/TIA.2017.2680398.

[33] S. Ramo, “Currents Induced by Electron Motion,” *Proc. IRE*, vol. 27, no. 9, pp. 584–585, 1939, doi: 10.1109/JRPROC.1939.228757.

[34] I. Adamczewski, “Induced conduction in dielectric liquids,” *Br. J. Appl. Phys.*, vol. 16, no. 6, pp. 759–769, 1965, doi: 10.1088/0508-3443/16/6/201.

[35] H. Kalman and E. Sher, “Enhancement of heat transfer by means of a corona wind created by a wire electrode and confined wings assembly,” *Appl. Therm. Eng.*, vol. 21, no. 3, pp. 265–282, 2001, doi: 10.1016/S1359-4311(00)00038-7.

[36] R. Pethig, A. Menachery, S. Pells, and P. De Sousa, “Dielectrophoresis: A review of applications for stem cell research,” *J. Biomed. Biotechnol.*, vol. 2010, 2010, doi: 10.1155/2010/182581.

Chapter 5: Conclusions and Future Work

In this chapter, a summary of the main contributions achieved by this study as well as the conclusions based on the main findings of the thesis are presented. Recommendations on future work to further gain ground on this research are covered.

5.1 Conclusions

This thesis focuses on utilizing the electrohydrodynamic technique to enhance the melting performance of phase change materials in latent heat thermal storage systems. The application of EHD on a dielectric medium can result in the generation of electroconvection flow in the liquid medium under the action of the electrical body forces. The EHD flow generated causes redistribution of the temperature field and consequently disturbs the thermal boundary layer which leads to increasing the heat transfer coefficient in the liquid PCM. Soid extraction is another mechanism that can contribute to the melting enhancement of PCMs in two phase solid-liquid systems under the effect of the interfacial forces at the melt front interface.

The main contributions of the current research work relate to three different aspects of EHD melting enhancement which address a number of key research gaps that include the investigation of the two main heat transfer enhancement mechanisms in solid-liquid systems. The first aspect relates to the role of each of the electrophoretic and dielectrophoretic forces, as well as the resisting buoyancy force on the generated EHD flow and melting performance of PCMs. The state-of-the-art literature contains no prior studies investigating the effect of temperature boundaries on the melting enhancement. Also, the influence of applying AC voltages with different frequencies on EHD melting was not found in literature. With respect to these gaps, the following contributions are provided by the current work:

- The effect of the variation of the DC voltages on the EHD melting enhancement, represented by the effective thermal conductivity, was determined.
- The influence of the voltage polarity and temperature limits on the melting performance was illustrated.
- The impact of applying AC square waves at different frequencies and offset values was resolved. This involved identifying the critical frequency for charge relaxation and demonstrating the significance of the dielectrophoretic effect.

The second aspect of the current research contributions relates to the effect of solid extraction as a possible heat transfer enhancement mechanism. In the literature, solid extraction was detected in only one study (Nakhla et al. 2015) where paraffin wax was melted under constant heat flux boundary conditions at -8 kV. However, no sloid extraction was observed in the other studies of Thompson et al. 2017 and Nakhla et al. 2018. There are some possible factors that need investigation to determine their influence on solid extraction which include the thermal boundary conditions, the electric field gradient, and the mushy zone thickness. Additionally, the literature contains no study on the characterization of solid extraction and the behavior of the extracted dendrites. The contributions addressed those gaps are:

- Investigation of solid extraction for paraffin wax using two different electrode configurations was performed. Also, exploration of solid extraction with different phase change materials having different mushy zone thickness was carried out.
- Solid extraction characterization was conducted by measuring the size and velocities of the extracted dendrites at different applied voltages and temperature gradients.

The third aspect of this study relates to the numerical modeling of charge injection and the EHD flow in two-phase systems. In the state-of-the-art literature, charge injection was modeled using only the autonomous injection assumption for which the space charge density at the emitter electrodes is assumed constant. However, this assumption does not accurately represent the actual injection charge density as the charge injection depends on the local electric field at the surface of the electrodes. Additionally, the electroconvection flow during EHD melting was studied only for the rectangular cavity and the concentric cylinders electrode configurations. Based on these gaps, this thesis makes the following contributions:

- A numerical model of charge injection assuming non-autonomous injection at the electrodes is developed.
- Numerical modeling of EHD melting of PCMs under constant temperature boundary conditions was conducted, wherein the simulation of space charge density, flow field, temperature field, and phase field are presented.
- The effect of voltage and temperature gradients on the electroconvection flow and Coulomb force was studied.

The findings of the research of this thesis, which were presented in the three journal papers in chapters 2, 3, and 4, are presented next. The contributions related to the first and second aspects are covered in the first paper and the experimental work of the third paper. Specifically, in these studies, the heat transfer enhancement with the application of EHD was investigated during melting of paraffin wax under constant temperature boundary condition. Experiments were conducted using both DC and AC applied voltages. The melt thickness was measured as melting progresses from the non-EHD steady state case to the EHD steady state case. The study also involved determining the EHD enhancement factor and the effective thermal conductivity of the PCM. For the DC cases, the melting enhancement increases with voltages where the maximum enhancement factor reached at -10 kV was 4.75. The effective thermal conductivity for this case was calculated to be 0.95 W/m-k. The investigation of the polarity effects revealed that when voltages exceed 6 kV, the negative polarity exhibited a slightly greater enhancement compared to the positive polarity. The impact of temperature boundaries on EHD melting enhancement was found to be minimal. The primary influence was attributed to the buoyancy force acting on the bulk liquid to reduce electroconvection. From the AC experiments, it was concluded that the effect of the dielectrophoretic force is negligible. The critical frequency for charge relaxation was identified as 2 Hz, and by reducing the frequency below this value the Coulomb force starts to take effect. The melting enhancement at 1 Hz frequency case was higher compared to the DC case hypothesized to be due to the flow instabilities. Additionally, it was found that the Coulomb force is still effective when applying high frequency AC unsymmetric wave forms, and that the enhancement results is not depending on the wave frequency for these conditions.

The investigation of solid extraction included in these studies showed that the extraction was detected with high intensities for all the applied voltages in the case of paraffin wax. The dendrites were pulled out from the mushy zone at the melting interface into the liquid bulk due to the influence of the Coulomb force. The intensity of extraction, as well as the velocity and size of dendrites are noted to be more pronounced near the electrodes and diminished as one moved toward the center region between each pair of electrodes. Additionally, increasing the voltages resulted in an increased level of dendrite extraction and higher velocities for the extracted dendrites. This revealed that the coulomb force is the dominant mechanism that influences solid extraction in the current study. In the case of RT 31, solid extraction was much lower compared to the cases of paraffin was. For n-Octadecane, no extraction was detected. These results show that as the mushy thickness increases for PCMs with high melting temperature ranges, solid extraction is intensified.

The contributions related to the third aspect of this research are presented in the second paper and the numerical work of the third paper. Numerical investigations of EHD melting of PCMs under constant temperature boundary conditions were conducted using the finite element method. The numerical results revealed that melting without EHD was conduction-dominated due to the thermal stratification of the liquid layers of the PCM. When EHD is applied, melting is recommenced due to the generation of EHD flow in the liquid PCM, where two opposing electroconvection cells were created between each pair of electrodes. Melting continued until a steady-state condition was regained after about 1 hour, when the liquid fraction rose to a value of 72 %, with an enhancement factor of 1.6.

Furthermore, in chapter 4, numerical modeling of charge injection was implemented to investigate the electroconvection flow during melting of phase change materials under different applied voltages and temperature boundaries. The EHD flow velocities were observed to increase with the increase of voltages, primarily due to the amplification of the Coulomb force. Conversely, an elevation in temperature gradients across the liquid phase introduces stronger buoyancy effects, leading to a reduction in fluid velocity.

5.2 Recommendations for Future Work

Investigating the role of the Coulomb force and the dielectrophoretic force on the heat transfer enhancement during melting of phase change materials and understanding the factors affecting the enhancement mechanisms of the electroconvection flow and solid extraction is very challenging. Although the contribution made by the research in this thesis address many of these challenges, there remain several avenues for future research to build upon this work, including:

- Investigating the influence of AC voltages with different wave forms on the process of charge injection and melting enhancement.
- Developing a novel electrode design that can allow for higher voltages to be conducted before reaching the breakdown voltage.
- Investigating the effects of electrode materials and type of phase change materials on the charge injection mechanism. Different PCMs with different electrical conductivities can influence the injection process and consequently affect the melting enhancement.
- Experimentally studying solid extraction using PIV technique for a better understanding of the phenomenon and its contribution to the EHD melting.
- Investigating the influence of adding small particles with different dielectric constants to the phase change material on the heat transfer enhancement and solid extraction during EHD melting.
- Numerically modeling charge injection process as negatively charges being injected from the ground electrodes to compare the results with the current study of positive charges injected at the high voltage electrode.
- Numerical modeling of the interfacial forces during melting of phase change materials for investigating solid extraction in two-phase systems.
- The numerical model developed in this research considered only the Coulomb force as the primary force contributing to the melting enhancement. It is recommended to apply the dielectrophoretic force to the model for a better representation of the EHD problem.